

Sensing and Actuation in Electroactive Elastomeric Bodies

by

Richard James Morrin Ellingham

A thesis submitted for the degree of
Doctor of Philosophy

in

Mechanical Engineering

at the

UNIVERSITY OF CANTERBURY

September 2024

Declaration of Authorship

I, AUTHOR NAME, declare that this thesis titled, 'Sensing and Actuation in Electroactive Elastomeric Bodies' and the work presented in it are my own. I confirm that:

- This work was done wholly or mainly while in candidature for a research degree at this University.
- Where any part of this thesis has previously been submitted for a degree or any other qualification at this University or any other institution, this has been clearly stated.
- Where I have consulted the published work of others, this is always clearly attributed.
- Where I have quoted from the work of others, the source is always given. With the exception of such quotations, this thesis is entirely my own work.
- I have acknowledged all main sources of help.
- Where the thesis is based on work done by myself jointly with others, I have made clear exactly what was done by others and what I have contributed myself.

Signed:

Date:

“When do you think you can submit your thesis?”

T. Giffney, April 2024

“Today.”

R. Ellingham, September 2024

UNIVERSITY OF CANTERBURY

Abstract

College of Engineering
Mechanical Engineering

Doctor of Philosophy

by [Richard James Morrin Ellingham](#)

Some of the world's most advanced technology is rigid due to various factors such as; manufacturability, miniaturisability, physical linearity, and more ideal physics in general. In parallel industries is also looking to use automation to improve and replace laborious tasks whether they be domestic, commercial, or industrially related tasks. There is a growing need for new innovations in technology to utilise the soft robotic solutions that mimic biological solutions seen in nature. This thesis is part of many to improve an understanding of the electroactive polymer subset of soft robotics and the limitations of specific implementations of artificial skin and artificial muscle technologies.

This thesis explores the integration of Electrical Impedance Tomography (EIT) with advanced soft sensing technologies, focusing on carbon black silicone rubber (CBSR) elastomer composites and Dielectric Elastomer Actuators (DEAs) to enhance pressure mapping, strain sensing, and actuation.

CBSR elastomer composites, noted for their high stretchability and biocompatibility, were investigated to understand their resistance relaxation behavior. This research contributes to optimizing the design of flexible dynamic strain sensors by modeling the response of resistance to transient strain inputs. The study developed an EIT-based pressure mapping system using a silicone CB nanoparticle sensing domain that mimics pressure mapping qualities human skin. This system was evaluated for its spatial and temporal resolution, showing potential for creating artificial pressure-sensitive skin with practical applications. Furthermore, the integration of EIT with DEAs was examined to improve the mapping of compressive forces across electrode surfaces. Despite some trade-offs in accuracy due to electrode compliance, this approach offers promising advancements for applications requiring precise actuation and pressure mapping. This work has majorly contributed towards filing a patent for an DEA-EIT actuator-sensor device. Additionally, the research uncovered unintentional power generation in DEAs, which could function as Dielectric Elastomer Generators (DEGs) due to mechanical strain. This finding highlights the dual functionality of DEAs and suggests opportunities for energy harvesting applications. Finally, a portable, low-cost EIT-based hardware system for pressure mapping was introduced. This system enables comprehensive characterization of various sensing domains and supports advancements in EIT-based soft sensor technology, with implications for biomedical devices, robotics, and energy harvesting.

Overall, this research advances the field of soft sensors by integrating EIT with innovative materials and technologies, providing new insights and applications in dynamic sensing and actuation.

Acknowledgements

People to thank:

- UC Bioengineering office - Lung lads, Lung Ladies, IPC, Hamish for infinite beers, Nic's abstract art.
- Geoff Chase - for a constant stream of stories and advice always within earshot.
- Other office - for ping pong madness, bikkies and fruit.
- Supervisor Tim - for time, money, lack of time, and support on a project that slightly diverged from his research till the end.
- Co-supervisors Chris, and late comer Lui - for advice and casual yarns.
- Summer students Toby and Yeni - for great work towards my PhD topic.
- UC mechanical and electrical department technicians (Julian Murphy, Julian Phillips, Tony Doyle, Scott Lloyd, amongst others) - for general support and yarns throughout my maddness.
- Juan Jose and Anastasia at IMDEA Materiales - for help with me going down a wonderful materials science rabbit hole.
- Markus Vorrath and co. at TU Dresden - for giving me a home to type out words and a group to discuss soft robotics with.
- Johannes Mersch - For helping with some final (hopefully groundbreaking) experiments when I was in strife towards the end of my PhD.
- Tess - for general oddities, support, and love.
- Friends - for constantly questioning "so when are you finishing again?"
- Family - for being supportive.

Contents

Declaration of Authorship	i
Abstract	iii
Acknowledgements	iv
List of Figures	vii
List of Tables	x
Abbreviations	xi
Symbols	xii
1 Introduction and Motivation	1
1.1 Why Go Soft and Not Rigid?	1
1.2 Research Objectives	2
1.3 Chapter Contributions	3
2 Literature Review	4
2.1 Biological Skin form and function	4
2.1.1 Skin Construction and Types	6
2.1.2 Characterising skin	7
2.1.3 Skin Modelling	9
2.2 Pressure Mapping Artificial Skin Devices	9
2.2.1 Soft Pressure mapping technology	9
2.2.1.1 Resistive	10
2.2.1.2 Capacitive	10
2.2.1.3 Magnetic	11
2.2.1.4 Optical	11
2.2.1.5 Acoustic	11
2.2.1.6 Soft Pressure mapping technology comparison	11
2.3 Biological Muscle form and function	13
2.3.1 Characterising a muscle	13
2.3.2 Muscle Mechanics	15
2.3.3 Electrical Muscle Models	16

2.4	Artificial Muscle Technology	16
2.4.0.1	Ionic polymer–metal composite actuator	16
2.4.0.2	HASEL actuator	17
2.4.0.3	Dielectric Elastomer Actuators	19
2.4.0.4	Magnetorheological Elastomer	20
2.5	Soft Conductive Particle Piezoresistive Composites	21
2.5.1	Fabricating Conductive Particle Elastomer Composites	21
2.5.2	Modelling Conduction mechanism	22
3	Giving Artificial Muscles the Sense of Touch	24
3.1	INTRODUCTION	24
3.1.1	Background	25
3.1.1.1	Dielectric Elastomer Actuators	25
3.1.1.2	Soft EIT-based Pressure Mapping	27
3.1.2	Simultaneous Pressure Mapping and Actuation	28
3.2	METHODOLOGY	28
3.2.1	Dielectric Elastomer Preparation	28
3.2.2	Compliant Electrode Fabrication	29
3.2.3	DEA Hardware	30
3.2.4	EIT Hardware	31
3.2.5	Experimental Method	31
3.2.5.1	DEA Validation	32
3.2.5.2	EIT-based Pressure Mapping on DEA	33
3.2.6	Simultaneous Actuation and Pressure Mapping	34
3.3	RESULTS	36
3.3.1	Fabrication	36
3.3.2	DEA Validation	36
3.3.3	EIT Validation	38
3.3.4	Simultaneous Actuation and Pressure Mapping	41
3.4	DISCUSSION	42
3.4.1	Fabrication	42
3.4.2	DEA Validation	42
3.4.3	EIT Validation	43
3.4.4	Simultaneous Actuation and Mapping	43
3.4.5	Altered Actuation Performance	44
3.4.6	Dielectric Breakdown	44
3.5	CONCLUSION	44
Bibliography		46

List of Figures

2.1 Examples of the locations of proprioceptors and cutaneous mechanoreceptors in the human body.	5
2.2 Clockwise from top left: IMU pose estimation[1] (© 2022 MDPI), stretch sensor knee joint pose estimation[2] (© 2020 IEEE), encoder elbow pose joint estimation[3], stretch sensor hand joint pose estimations[4].	5
2.3 Various pressure mapping devices. From top-left then clockwise: XSsensor wheelchair pressure mapping sheet (© 2024 XSENSOR® Technology)[5], Pressure Profile Systems pressure sensors on a robotic hand (© 2023 PPS UK limited)[6], Soft pressure mapping gripper[7], Tekscan thin pressure mapping platform[8](© 2024 Tekscan Inc.), Tactilus seat pressure mapping system[9](© 2024 Sensor Products Inc.)	6
2.4 Two grey electrodes across a blue dielectric medium. Left: Uncompressed state. Right: Compressed state exhibiting larger electrode areas and a thinner dielectric thickness.	10
2.5 Components of a biological muscle contractile unit and meta-structure.	13
2.6 Stress and strain of active and passive muscles (© J. Teran ACM 2003)[10] . . .	15
2.7 Diagram of the typical architecture of an IPMC actuator[11] (© 2018 Yanjie Wang and Takushi Sugino)	17
2.8 Diagram of the typical architecture and the contraction stages of a HASEL actuator[12]	18
2.9 Diagram of the simplified stages of HASEL actuator production[12]	18
2.10 DEA with two compliant light-grey electrodes and a transparent light blue dielectric elastomer. Showing deformation without and with a voltage applied across the electrodes.	19
2.11 Diagram showing MRE contraction actuation when a magnetic field is applied[13]	21
2.12 Two grey highly conductive electrodes across a CPEC cuboid showing enlarged black conductive particles within a blue polymer matrix. Left: An uncompressed CPEC. Right: A compressed CPEC.	22
2.13 Example of a randomised cube percolation with a volume percentage of 8% of particles	23
3.1 Potential future application of the DEA-EIT device topology. Left: EIT sensor input DEA controlled optical lens. Right: Pressure mapping sensitive skin for a DEA propelled jellyfish soft robot.	25
3.2 A circular DEA exemplifying its actuation principle.	26
3.3 A 16 electrode circular EIT domain setup exemplifying its electrical function. Where the dashed lines are representative of an applied electric field[14]	27
3.4 Mechanical fabrication of the circular DEA-EIT platforms	29
Elastomer prestretch method	29
Elastomer prestretch method	29

(b)ular DEA construction	29
(b)ular DEA construction	29
Single circumferential electrode	29
Single circumferential electrode	29
Multiple circumferential electrodes	29
Multiple circumferential electrodes	29
3.5 DEA excitation and measurement setup	31
3.6 Architecture of the force applicator and EIT measurement system [15]	31
3.7 The two DEA compliant electrode material types used in this work.	32
(Th)reference DEA made with CB powder compliant electrodes	32
(Th)reference DEA made with CB powder compliant electrodes	32
(Ab)DEA with 0.5 mm thick compliant electrodes at steady state contraction and excited at 32 kV	32
(Ab)DEA with 0.5 mm thick compliant electrodes at steady state contraction and excited at 32 kV	32
3.8 Load application areas used for compressive stress testing in order of application[15]	33
3.9 The two spatial performance metrics used for determining accuracy of blob as a load area estimate, where the transparent white circle is the actual load area and the dark purple elements are the load estimate area.	34
(\hat{A}_{CoM})	34
(\hat{A}_{CoM})	34
34 ($\hat{S}(E)$)	34
34 ($\hat{S}(E)$)	34
3.10 System architecture for simultaneous DEA actuation and EIT mapping.	35
3.11 Illustrative experiment timing diagrams. Left: Steady state V_{DEA} where the purple dotted lines represent the time a load event begins. Right: Transient EIT measurements where the red dotted line represents the time an EIT frame capture begins.	36
3.12 Comparing the measured CB reference DEA strain, the theoretical strain average and range, and the data fitted to Equation 3.3 by fitting either parameter K or ε_r	37
3.13 Comparison of the voltage strain relationships between the 100 mm diameter compliant electrodes of various thicknesses, z_{ce} , used for the DEA.	37
3.14 A 15% strain compression at point L_1 applied to 100mm diameter compliant DEA electrodes of 3 compliant electrode thicknesses.	38
$\hat{\epsilon}(a) \neq 0.38\text{mm}$	38
$\hat{\epsilon}(a) \neq 0.38\text{mm}$	38
$\hat{\epsilon}(b) \neq 38\text{mm}$	38
$\hat{\epsilon}(b) \neq 38\text{mm}$	38
$(\hat{\epsilon}_c) = 38\text{mm}$	38
$(\hat{\epsilon}_c) = 38\text{mm}$	38
Scale	38
Scale	38
3.15 Vectorised E_{CoM} for the nine load experiment at 20% compressive strain for each z_{ce} value tested on individual DEA-EIT compliant electrode samples.	39
$\hat{\epsilon}(a) \neq 0.39\text{mm}$	39
$\hat{\epsilon}(a) \neq 0.39\text{mm}$	39
$\hat{\epsilon}(b) \neq 39\text{mm}$	39
$\hat{\epsilon}(b) \neq 39\text{mm}$	39

$\epsilon(\epsilon) \neq 39\text{mm}$
$\epsilon(\epsilon) \neq 39\text{mm}$
$I_{(ob)}39\text{locs}$
$I_{(ob)}39\text{locs}$
3.16 Vectorised E_{CoM} for the nine load experiment using the same indentation depth as Figure 3.15 for each z_{ce} value tested on the DEA-EIT integrated samples.	40
$\epsilon(a) \neq 0.40\text{mm}$
$\epsilon(a) \neq 0.50\text{mm}$
$\epsilon(b) \neq 40\text{mm}$
$\epsilon(b) \neq 40\text{mm}$
$\epsilon(\epsilon) \neq 20\text{mm}$
$\epsilon(\epsilon) \neq 20\text{mm}$
$I_{(ob)}40\text{locs}$
$I_{(ob)}40\text{locs}$
3.17 Loads applied to the compliant ground electrode of a DEA during different steady state voltage excitations, V_{DEA}	41
$V_{(a)A} = 41\text{kV}$
$V_{(a)A} = 41\text{kV}$
$V_{(b)A} = 41\text{kV}$
$V_{(b)A} = 41\text{kV}$
$V_{(c)A} = 41\text{kV}$
$V_{(c)A} = 41\text{kV}$
3.18 An unloaded DEA with a captured during various voltage, V_{DEA} , step input artifacts.	41
$V_{(a)A} = 41\text{ kV}$
$V_{(a)A} = 41\text{ kV}$
$V_{(b)A} = 44\text{ kV}$
$V_{(b)A} = 44\text{ kV}$
$V_{(c)A} = 10\text{ kV}$
$V_{(c)A} = 10\text{ kV}$

List of Tables

2.1	Comparison of typical mammalian mechanoreceptor characteristics [16].	7
2.2	Comparison of different potential piezo-resistive sensor materials. Ranked 1 to 5, where 1 is desirable and 5 is undesirable. WIP - need to find a reference for each box!	10
2.3	Comparison of soft sensor technologies.	12
3.1	Effective bulk modulus, K_{eff} , and coefficient of determination, R^2 , for each fit of voltage-strain data for the CBSR compliant electrodes.	38
3.2	Noise factor and mean inter-electrode resistance, \bar{R}_{int} , for each thickness of compliant DEA electrode used for EIT	39
3.3	Mean E_{CoM} and SF values (\pm std) obtained for each DEA compliant electrode thickness at 20% strains loads	40
3.4	Mean E_{CoM} and SF values (\pm std) obtained for each DEA stack at the same indent depth as 20% strain in Table 3.3 loads. *Where the compliant electrode is part of a DE compliant electrode DEA stack.	40

Abbreviations

ADC	Analog-to-Digital Converter
CAD	Computer Aided Design
CB	Carbon Black
CFA	Cartesian Force Applicator
CE	Compliant Electrode
CoM	Center of Mass
DE	Dielectric Elastomer
DEA	Dielectric Elastomer Actuator
DEG	Dielectric Elastomer Generator
DUT	Domain Under Test
EIT	Electrical Impedance Tomography
ERT	Electrical Resistance Tomography
FEA	Finite Element Analysis
FEM	Finite Element Modelling
FPC	Flexible Printed Circuit
IDF	IoT Development Framework
MUX	Multiplexer
PCB	Printed Circuit Board
PCBA	Printed Circuit Board Assembly
PDMS	Polydimethylsiloxane (AKA silicone)
PNEC	Piezoresistive Nanoparticle Elastomer Composite
SMU	Source Measure Unit
SMD	Surface-Mount Device
SR	Silicone Rubber
THT	Through-Hole Technology
EAP	Electro-Active Polymer

Symbols

A	Area	[m ²]
C	Capacitance	[F]
ϵ	Permittivity	[Dimensionless]
K	Bulk Modulus	[Pa]
ν	Poisson's Ratio	[Dimensionless]
Q	Electrical Charge	[C]
U_E	Electrical Potential Energy	[J]
U_ϵ	Elastic Potential Energy	[J]
R	Resistance	[Ω]
σ	Stress	[Pa]
S	Strain	[Dimensionless]
V	Voltage	[V]
Y	Young's Modulus	[Pa]
z	Thickness	[m]

Dedicated to tinned baked beans in all their glory... .

Chapter 1

Introduction and Motivation

Rigid robotic systems often have multiple rotary motors and various sensors integrated together for precise control of the robot, this is mirrored in biology with the animals having many actuator units in the form of muscles and a multitude of various receptors for sensing their environment. The rigidity of rotational motors is stifling creativity in the creation and development of devices amongst many other unforeseen future technology. Engineers are often constrained to solving problems and designing solutions using typical rigid sensors and actuators due to their current ubiquity and their evolved increased efficiency. With the rise of research into soft sensor and actuator devices, these such device need to follow suit of the traditional rigid sensors and actuators and become ubiquitous and viable option for general and specialised engineering design solutions.

This thesis has developed methods and tools for creating and characterising artificial pressure sensitive skin technology. The thesis then continues to explore the integration of this artificial skin technology into an artificial muscle technology. The work in this thesis has ultimately contributed towards a patent for DEA-EIT actuator-sensor technology in a quest to bring this work out of the academic realms into real-world applications.

1.1 Why Go Soft and Not Rigid?

The requirement for soft robotics in general has been driven by the limitations of current rigid robotic solutions to interact with natural organic material. Manipulation of natural organic objects such as animals, plants, fruit, vegetables, and meat have traditionally been handled by humans by hand due to our ability to use our dexterity and intelligent control systems to ensure minimal undesirable damage. With the advance in technology in various soft robotic actuators[17–21], sensors[22], and soft robotics control[23, 24]. The use of soft robotics in place of rigid alternatives, amongst other benefits, has the opportunity to be more sustainable by decreasing waste products during fabrication, using biodegradable or recyclable materials, shelf life, and use of renewable resources[19]. The use of soft robotics brings opportunity of creating devices with a reduced bill of materials size and less moving parts for maintenance. The use of soft robotics in biomedical and aerospace applications is especially desirable due to the difficulties experienced when designing with regular motors in the outer space and near sensitive biological tissue environments such as heat dissipation, lubrication, and mass[25–28].

The most common rigid actuator is the rotary electric motor and the global market was valued at USD 142.2 billion in 2020, with a predicted growth rate of 9.5% until 2032[?]. Although this

market is dominated by automobiles which currently require the traditional form of rotary electric motors, growing sectors of this market such as medical, factory automation, and aerospace have potential interest in adopting soft actuator alternatives for the reasons given above. In parallel, rigid strain sensors of types metallic foil and semiconductor, was given a global market value of USD 190.66 million in 2022 with a compound annual growth rate of 3.9% until 2029[?]. Adjacently the pressure mapping global market value, focused mainly on the health sector, was valued at USD 480 million in 2023 with an expected growth rate of 5.1%[? ?]. Many soft actuator technologies could be used in these growing medical, aerospace, factory automation, and agricultural sectors.

Soft robotic actuation can be achieved through various mechanisms including thermal, electrochemical, fluidic, magnetic, and electrostatic. Similarly soft stress-strain sensing can be achieved through various physical principles such as resistive, capacitive, magnetic, and optical sensing methods. Often the function of soft actuators can be inverted such that the deformation of the actuator can produce a signal used for self sensing, in electroactive polymer (EAP) technologies such as dielectric elastomer actuators (DEAs)[29–32] and ionic polymer-metal composites (IPMCs)[33]. EAPs have the benefit of electronic control over other soft actuator and sensor technologies controlled by fluids, heat, or light which contain the complexity of another energy transfer process.

Proprioception in artificial muscle technology has been made a reality. This is seen in the self-sensing of one dimensional strain of DEAs usually through capacitive measurement between the compliant electrodes during operations to obtain the magnitude of a contraction. However, the pressure mapping done similar to the mechanosensation performed by cutaneous mechanoreceptors on an artificial muscle device has not been explored as of writing this thesis.

Publications towards this thesis include three conference papers, one journal paper, and one provisional patent filed. This thesis has converged on the use of conductive particle based elastomer composites and their use in sensors and actuators, in particular an electrical impedance tomography (EIT) based artificial skin and it's integration into the artificial muscle technology, dielectric elastomer actuators. The composite type used throughout the thesis is simple to fabricate but not well understood in terms of its electromechanical transient and dynamic characteristics. The modelling of such conductive particle composites would elucidate the feasibility of inverting the model to create a responsive strain sensor. This composite has been characterised in one-dimension several times in literature already however, if a two dimensional sensing application of this composite is desired the characterisation of the sensor in two dimensions must be completed. A method to do such 2D sensing is using EIT. EIT has been used in the past for a huge range of applications, with few exploring the use of EIT as a pressure mapping sensor. Although EIT-based pressure mapping was first discovered 30 years ago, the technology is still in its infancy with several problems needing to be resolved before the technology can be used reliably in real-world applications.

1.2 Research Objectives

The research objectives and questions for this thesis are given below:

1. Quantify and analyse static, dynamic, and transient phenomena seen in conductive particle composites.
2. From the characterisation in objective 1 mitigate the effects of the transient phenomena.

3. Create a set of metrics for quantifying the performance of an electrical impedance tomography based artificial skin.
4. Simulate and integrate an electrical impedance tomography based artificial skin onto a dielectric elastomer actuator.
5. Investigate the energy harvesting of a device that is both a dielectric elastomer actuator and electrical impedance tomography device.

1.3 Chapter Contributions

Chapters ?? - ?? contain the core novel research contributions. Chapters 2 and ?? provide essential background knowledge and future research directions for the thesis respectively.

Chapter 2 - Literature Review: This chapter explores the nature of biological skin and muscle from an engineering perspective, quantifying necessary functions and properties desired to replicate or supersede for their artificial equivalents. The thesis then describes state-of-the-art soft sensors and actuators and their function.

Chapter 3 - A Simple Conductive Elastomer Composite Material with Complex Behaviour: This chapter uncovers the electromechanical tensile and compressive properties of carbon black silicone composites, in order to understand the material before it's use in sensors and actuators.

Chapter 4 - An Improved an Electrical Impedance Tomography Based Artificial Soft Skin Pressure Sensor: This chapter discusses the use of electrical impedance tomography to create a pressure mapping sensor and provides tools for analysing the suitability to various applications and choosing a suitable sensing domain.

Chapter 5 - Giving Artificial Muscles the Sense of Touch: This chapter describes the integration of the pressure mapping technology discussed in the previous chapter, how it can be integrated into dielectric elastomer actuators, and the trade-offs.

Chapter 6 - Unintentional Power Generation in a DEA-EIT Sensor-Actuator Device: This chapter discussed the unintended power generation of the simultaneous sensor actuator device discussed in the previous chapter.

Chapter 7 - A Portable Electrical Impedance Tomography Based Pressure Mapping Sensor and Validation System: This chapter discusses the small form factor, low-cost hardware design for a hybrid artificial muscle - artificial skin based device.

Chapter 8 - ?? Modelling of DEA-EIT Capacitively driven Hybird Sensing and Actuation Device: The is chapter models the a DE-EIT device in order to find an optimal range of parameters at which capacitive shunting can be used to improve the DE-EIT pressure mapping device responsiveness.

Chapter 9 - The Biomimetic Re-Evolution: This chapter discusses the future direction of the technology discussed in the thesis and acknowledges the future of the broad field of soft robotics.

Chapter 2

Literature Review

Humans can complete complex tasks due to their intelligence, dexterity, and physical make up. These complex tasks include agricultural picking, culinary preparation, factory goods processing, and biomedical practice. To complete these tasks with machines it is important to quantify these human qualities that the technology must match or supersede. The first part of this section is focused on understanding and quantifying human skin and muscle tissue often required for these complex human tasks. In parallel, artificial skin and artificial muscle state-of-the-art technology is reviewed. Finally, background theory on piezoresistive elastomer composites which will be utilised with specific sensor and actuator technology is given to setup foundational knowledge base and reference for the rest of the thesis.

2.1 Biological Skin form and function

Skin is the largest organ in the human body with many functions, however this thesis only aims to replicate some pressure-sensitive functions of skin. Two pressure-sensitive categories of skin and muscle tissue transducers which allow for dexterous manipulation of objects are:

1. Proprioceptors: respond to internal mechanical stimuli in a joint capsule, tendon, or muscle to give the sense of motion.
2. Cutaneous mechanoreceptors: respond to mechanical stimuli usually external to the body, including pressure and vibration, for the localisation of sensations.

Locations of both proprioceptors and cutaneous mechanoreceptors are shown diagrammatically in Figure 2.1. Proprioceptors aid in determining pose estimates of body parts in space, acting as sensors providing feedback closed-loop control for the neurological motion control of body parts. Whereas cutaneous mechanoreceptors have various roles including object recognition, manipulation control, as well as motion control.

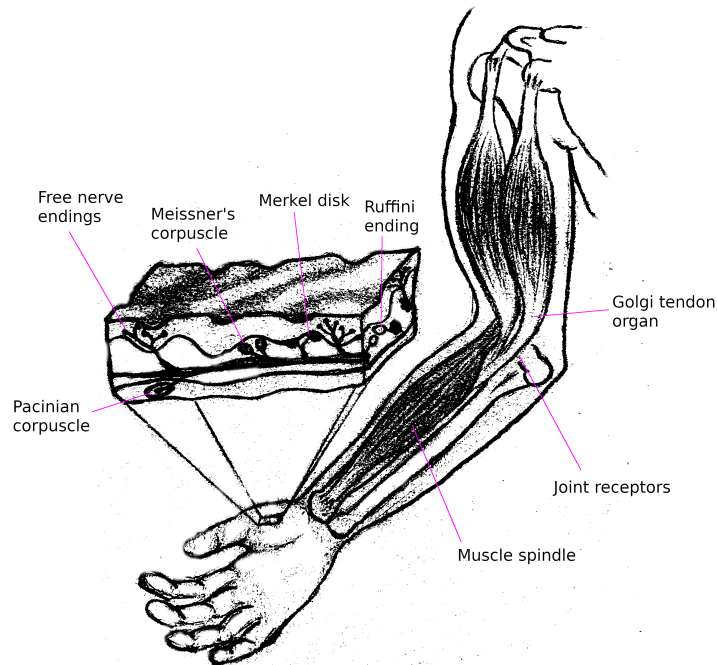


FIGURE 2.1: Examples of the locations of proprioceptors and cutaneous mechanoreceptors in the human body.

The function of both kinds of receptor have been mimicked by certain device technologies. For example proprioceptors have been mimicked in wearables and human assistive devices where joint motion has been estimated by sensors such as rotary/linear encoders, inertial measurement units (IMUs), and stretch sensors fixed adjacent to joints to calculate pose estimates of limbs[1–4]. Examples of such devices are displayed in Figure 2.2

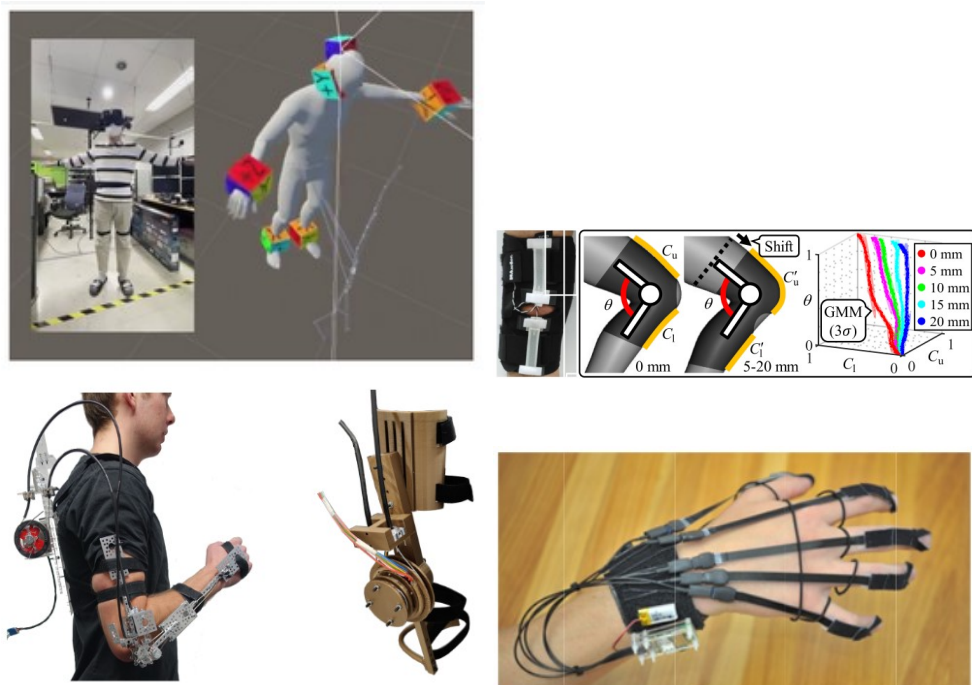


FIGURE 2.2: Clockwise from top left: IMU pose estimation[1] (© 2022 MDPI), stretch sensor knee joint pose estimation[2] (© 2020 IEEE), encoder elbow pose joint estimation[3], stretch sensor hand joint pose estimations[4].

Cutaneous mechanoreceptors have been mimicked by the development of pressure mapping of flexible surfaces. Examples of such technologies include, foot pressure based gait analysis, wheelchair seat pressure mapping. Commercially available examples of these sensors are shown in Figure 2.3.



FIGURE 2.3: Various pressure mapping devices. From top-left then clockwise: XSENSOR wheelchair pressure mapping sheet (© 2024 XSENSOR® Technology)[5], Pressure Profile Systems pressure sensors on a robotic hand (© 2023 PPS UK limited)[6], Soft pressure mapping gripper[7], Tekscan thin pressure mapping platform[8]((© 2024 Tekscan Inc.), Tactilus seat pressure mapping system[9](© 2024 Sensor Products Inc.)

Many of these pressure mapping technologies don't accurately mimic desirable qualities of regular biological skin and are specialised for their specific use cases. The following sections quantify characteristics of pressure sensitive skin.

2.1.1 Skin Construction and Types

Skin is a laminate structure consisting of three main layers, the epidermis, dermis, and hypodermis. The top two layers the epidermis and dermis are a subset of the cutaneous layer which contain the majority of the pressure-sensitive mechanoreceptors [34].

The skin can be categorised as glabrous/hairless or non-glabrous/hairy. Glabrous skin contains many of the mechanoreceptors given in Figure 2.1 whereas non-glabrous skin will also contain C-tactile afferent receptors for obtaining sensations through hair follicles. However this work is exploring simple monolithic/homogeneous-composite bodies so will not be replicating the sensor function of non-glabrous skin.

Depending on the region of skin different force resolution and spatial resolution will incur. Relevant cutaneous mechanoreceptors and their functions are given in Table 2.1. The tensile properties of skin is governed by skin tension lines, also called Lager's lines, which show the direction in which the maximal stretch can occur.

TABLE 2.1: Comparison of typical mammalian mechanoreceptor characteristics [16].

Receptor	Meissner corpuscle A1	Ruffini Corpuscle A2	Pancian Corpuscle B1
Perceptual sensory functions	Skin movement, handling objects	Skin stretch, movement direction, hand shape, and finger position	Fine tactile discrimination, form and texture perception
Skin stimulus	Dynamic deformation	Skin stretch	Indentation depth
Localisation	Dermal papillae	Dermis	Basal layer of epidermis / around guard hair
Conduction velocity	35 - 70 m/s	35 - 70 m/s	35 - 70 m/s
Receptive field	22 mm ²	60 mm ²	9 mm ²
Receptor density	150 / cm ²	10 / cm ²	100 / cm ²

2.1.2 Characterising skin

The sensing qualities of skin is crucial for the sensory feedback in complex manipulation tasks. To aid the creation of technology that mimics qualities of biological pressure sensitive skin, the mechanical properties must be characterised. Biological human skin is highly variable in terms of its mechanical and sensing properties depending on the region of skin, giving large variation in skin characteristics. Skin can be characterised in terms of the following mechanical characteristics:

1. Elastic modulus - The static elastic properties determined by a linear region of stress and strain of the material. [Pa]
2. Storage and loss modulus - The dynamic elastic and viscoelastic properties determining the relationship between stress and strain. [Pa]
3. Ultimate tensile stress (UTS) - The maximum tensile stress that a material can tolerate before breaking [Pa]
4. Life cycle - The time or number of actuation cycles in which it takes for the actuator to degrade such that it cannot perform its intended purpose to specified standards.

5. Viscoelastic creep and relaxation - All viscoelastic materials will experience strain creep and stress relaxation to varying degrees depending on the viscoelastic properties of the material. [$\text{mm} \cdot \text{s}^{-1}$ and s]
6. Skin thicknesses - the thickness of all layers of skin the cutaneous epidermis and dermis and thickness of the hypodermis. [mm]
7. Skin surface area - Biological skin has a large surface area and can also be regionalised to map skin function and sensitivity. [m^2]
8. Isotropy/Anisotropy - The directionality of skin properties, also known as skin tension lines, give a topological map of the maximal stretch (i.e. minimal elastic modulus) direction of regions of skin.

Some of the functional properties in terms of pressure mapping include:

1. Spatial resolution and touch acuity - The spatial resolution of biological skin, which is mainly dependent on the innervation, mechanoreceptors density, and thickness of the cutaneous layers of skin [35–37].
2. Static force resolution - This is the detection resolution of static or slow-acting forces acting upon the skin [37].
3. Temporal resolution - This is the detection resolution of fast-acting forces acting upon the skin often required for texture recognition [35, 37].

A quantitative characterisation of mechanical and pressure sensing functional skin properties include:

1. Elastic modulus - varies largely depending on test method, test skin type, and subject. Values found in literature include 83.3 ± 34.9 MPa [38], 0.1 - 2.4 MPa [39], and 10.4 - 89.4 kPa [40].
2. Storage and loss modulus - varies largely depending on test method, test skin type, and subject. Values found in literature range include 141.9 ± 34.8 Pa and 473.9 ± 42.5 Pa at 0.8 Hz [41], 473.9 ± 42.5 Pa and 32.3 ± 10.0 Pa at 205 Hz [42].
3. Ultimate tensile stress - 21.6 ± 8.4 MPa [38]. 28.0 ± 5.7 MPa [43]
4. Life cycle - Skin cells are constantly growing, dying, and shedding. Skin is always actively remodelling based on external stimuli [34].
5. Strain creep - The strain creep was found to be 2.7 kPa.s for a 10 Pa step input on a dermis skin sample [41].
6. Skin thicknesses - The thickness of human cutaneous skin ranges from 0.6 to 2.6 mm with an average skin thickness of 2 mm [35].
7. Skin surface area - The average surface area of skin in adult humans is $1.7 \pm 0.1 \text{ m}^2$ [35].
8. Isotropy/Anisotropy - The tension lines in skin are determined by collagen fibre orientation and dynamic stretch events [44, 45]. The elastic modulus of human skin was reported to be 160.8 ± 53.2 MPa parallel to the skin tension lines and 70.6 ± 59.5 MPa perpendicular to the tension lines [43]. The UTS of human skin was reported to be 28.0 ± 5.7 MPa parallel to the tension lines and 15.6 ± 5.2 MPa perpendicular to the tension lines [43].

1. Spatial resolution and touch acuity - The tactile field area increases with indentation depth for certain mechanoreceptors with a range of $5 - 12.6 \text{ mm}^2$ [46]. Two point discrimination is another metric for determining spatial resolution and has been determined as $3.7 \pm 0.7 \text{ mm}$ [47]. The receptive field varies depending on the mechanoreceptors used so has been reported to be between 1 and 60 mm^2 as another methods of inferring spatial resolution [16].
2. Force resolution - Minimum force detection on various regions of human skin was found to be between $67 - 1007 \text{ mg}$ [48], and various mechanoreceptors $0.73 - 122.6 \text{ mN}$ [49].
3. Temporal resolution - Depending on the mechanoreceptor sensing the force input, a frequencies ranges of 0 to 800 Hz can be perceived by human skin [46]

2.1.3 Skin Modelling

Developing robust mechanical models for human skin is non-trivial for three main reasons:

1. High degree of viscoelasticity
2. Self-regeneration and healing
3. Constructed from various types of cells in a laminate structure

To solve the complexity of modelling such a material a review by Landry et al.[35] shows that many researchers have applied various non-linear mechanical models including Ogden, Mooney–Rivlin, Neo-Hookean, Yeoh, Humphrey, and Veronda–Westmann. When recreating an artificial muscle it is desirable to minimise the mechanical material model complexity so that the material can be more easily integrated into a control system with known behaviour. Similar modelling techniques can be used to model conductive particle elastomer composites due to the similar hyper-elastic and visco-elastic behaviours observed.

2.2 Pressure Mapping Artificial Skin Devices

This section outlines some of the main technologies which are flexible and/or soft and comparable softness to human skin tissue and can map force events throughout a surface. A particular focus on electro-active polymer (EAP) based sensing is present due to the potential of miniaturising the technology and the range of miniaturised electronics currently available. EAPs are essentially polymer materials which can be used as transducers which change electrical properties based on a mechanical input, vice versa.

2.2.1 Soft Pressure mapping technology

Pressure mapping devices can be categorised into their various sensing technology, such as resistive, capacitive, inductive, magnetic, optical, and acoustic. Transduction methods have been compared by Tiwana et al.[50], with recommendations to pursue ‘capacitive, resistive, piezoelectric, piezoresistive or a combination’ of methods to replicate mechanoreceptors in the human skin. However, additional optical and magnetic/inductive methods will also be considered in the following sections.

2.2.1.1 Resistive

Soft resistive pressure mapping has been commonly achieved in the past by using arrays of piezoresistive sensor elements, some of which are shown in Table 2.3. The resistive elements can be made using several different flexible piezoresistive materials, such as conductive particle polymer composites[51–53], intrinsically conductive polymers[52, 54?], microfluidic metals[55–57], hydrogel structures [58–60], and flexible piezoresistive semiconductors[61, 62].

TABLE 2.2: Comparison of different potential piezo-resistive sensor materials. Ranked 1 to 5, where 1 is desirable and 5 is undesirable. WIP - need to find a reference for each box!

Material:	Conductivity	Piezo-resistivity	Hardness	Manufacturability	Cost	Durability	Toxicity	Drift
Conducting polymer	5	3	3	2	2	3	2	3
Electrolytic hydrogel	1	2	4	3	4	2	2	2
Conductive particle polymer	2	4	4	4	4	4	2	
Conductive particle paste	3	2	4	3	4	2	3	2
Conductive textile	4	4	3	2	4	5	4	3

2.2.1.2 Capacitive

Similar to resistive pressure mapping, capacitive pressure mapping has more commonly been done using arrays of capacitive elements. Many capacitive touch sensors use the human body to shunt the electric field between the capacitor electrode(s) to a common ground. However, the operating principle of capacitive-based strain sensors rely on the deformation of the capacitor dielectric and/or the capacitor electrodes [63? , 64]

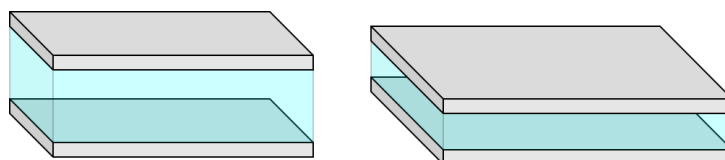


FIGURE 2.4: Two grey electrodes across a blue dielectric medium. Left: Uncompressed state. Right: Compressed state exhibiting larger electrode areas and a thinner dielectric thickness.

2.2.1.3 Magnetic

Magnetic strain mapping devices can be achieved using several methods. One method is to have a three layer stack with hall effect sensors [65]. The stack is made up of a the bottom layer full of rigidly connected three dimensional hall effect sensors, the second layer is made from an elastomer, and the top layer has a magnetic particle unit placed at a set distance above each of the hall effect sensors. The movement of the magnets alters the magnitude and direction of magnetic field sensed and data can be interpolated to create a map of strain deformation. The main advantages of this method is that each hall sensor can detect in three dimensions, hence normal and shear forces can be detected, and using magnetismfor sensing means less electrical noise in the system. The main disadvantages of this method of sensing is the added complexity in scaling the system and the electronics required and the rigid surface required.

2.2.1.4 Optical

There are various methods for making a optically driven artificial skins. A recent review has been curated by Lee et al. [66] all of the different methods of using optics for creating tactile sensors. The main advantages of optical sensors include the high speed sensor response, immunity to electrical noise, and their non-invasive nature. The main disadvantages include, the bulky hardware required for driving the optics and signal processing, the potential interference of external light sources, and the materials that can carry optical signals.

2.2.1.5 Acoustic

Acoustic soft tactile sensing has not been explored much compared to the other forms of sensing given. Park et al., Hughes and Correll [59, 67] have created a system which uses passive acoustic tomogrphy (PAT) to localise and and classify different types of touch. This form of tactile sensing is the most similar to the biological system of mechanoreceptors which are specialised to detect certain frequencies of vibration.

2.2.1.6 Soft Pressure mapping technology comparison

The softness of biological human skin has a large range as discussed in Section 2.1.2. There have been a range of works investigating sensors with a range of softness' and performance. A comparison of these start-of-the-art soft sensor works is given in Table 2.3.

TABLE 2.3: Comparison of soft sensor technologies.

1st Author	Sensing principle	Sensing region material	Sensing region elastic modulus or shore hardness	Electrodes per sensing position	Repeatability	Time series data shown	Spatial resolution	Temporal resolution
Gilanizadehdizaj [68]	Piezo-resistive	Ecoflex30-00 rGO composite sponge	40 kPa	2 sensels / electrode	10 cycles for each stress	-	10 x 10 mm	-
Fu[69]	Piezo-resistive	Carbon black silicone composite	1.5 Mpa	0.625 sensels / electrode	50000 cycles	Yes.	12 x 12 mm	60 ms
Yang[70]	Piezo-resistive	Ecoflex graphene composite sponge	-	2 sensels / electrode	800 cycles	Yes.	10 x 10 mm	150 ms
Liang[64]	Capacitive	PDMS, PET, Si, Sio2, Cu laminate	4000 Mpa	1 sensel / electrode	-	Real-time use of sensor shown. No explicit time-series data.	4 x 4 mm	-
Yan[65]	Magnetic	Ecoflex 00-50	83 kPa	11 IC pins / sensel	30,000 cycles	Yes.	0.1 x 0.1 mm	15 ms
Rossiter[71]	Optical	Polymer foam	-	2 sensels / electrode	-	-	10 x 10 mm	-
Shimdera[72]	Optical	Super clear silicone	40 A	N/A. One fiber optic LASER and one camera.	Error increase of 1.7% over 30 days	Yes.	approx. 20 x 20 mm / 0 - 1100 um	Sample rate 1.6s. Training required.
Ramuz[73]	Optical	PDMS	-	N/A. Two arrays of OLEDs and Organic Photo Detectors used.	900 cycles	Yes.	Not localised.	300 ms

2.3 Biological Muscle form and function

Biological muscles are a product of millions of years of evolution and the motion and other mechanical characteristics of biological structures is yet to be outperformed by artificial muscle technology. To determine how to quantify the performance of a biological muscle this section gives foundational knowledge about muscle function, structure, and how it can be characterised from an engineering perspective rather than the typical biological perspective, so that similar actuator devices with similar attributes can then be investigated.

Biological muscle is a naturally occurring tissue comprised of muscle fibres bundled together to apply a contractile force on connecting tissue or, in the case of smooth muscle, applying a force on itself. The base actuator units of muscle are proteins myosin and actin filaments, which effectively slide against each other to produce a contractile motion. The root cause of a muscle contraction is an electrochemical signal sent from the central nervous system to a motor neuron/s which travel to the muscle where electrochemical reactions take place for the contraction to occur[74]. The sliding motion of the myosin and actin filaments is due myosin

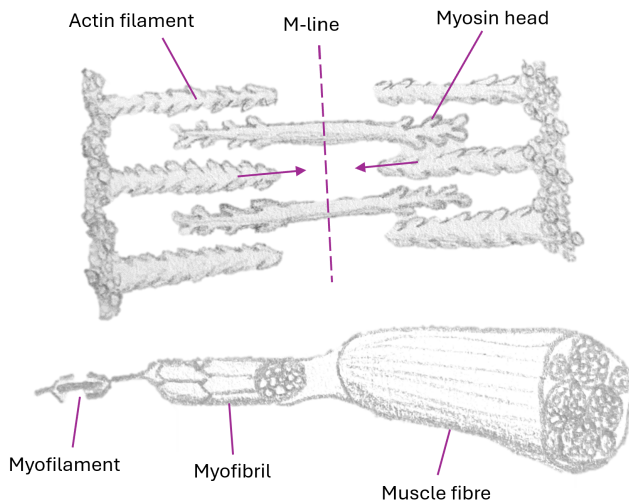


FIGURE 2.5: Components of a biological muscle contractile unit and meta-structure.

heads binding to the actin and pulling the actin towards a middle line (M-line) in multiple stroke actions. These filament actuators are stacked in three dimensions within a muscle fibre to amplify contractile stress and strain as shown in Figure 2.5.

On a macro scale, muscle is made up of bundles of fascicles connected together with a tissue called perimysium. Within the fascicles are many muscle fibres (i.e. muscle cells) which are surrounded by a connective tissue called endomysium. Within the muscle fibres there are many sacromeres stacked within a cylindrical-like structure called a myofibril. Each sacromere contains a contractile unit of myofilaments.

2.3.1 Characterising a muscle

To quantify the performance of a biological muscle, certain metrics are compared. An artificial and biological muscle can be characterised using typical mechanical material parameters such as:

1. Stress - Force that is applied to the normal of the cross section of the muscle through various states of muscle excitation. [Pa]
2. Strain - The muscle change of length due to the stress applied through various states of muscle excitation. [%]
3. Elastic modulus - The elasticity determining the relationship between stress and strain for the linear region of the stress strain characteristic curve. [Pa]
4. Energy density - The work done by the muscle per unit volume or mass. [$J.kg^{-1}$]
5. Power density - The work done by the muscle per unit volume or mass per unit time. [$W.kg^{-1}$]
6. Ultimate tensile strength - The maximum tensile stress that a material can tolerate before breaking. [Pa]
7. Efficiency - The work done by the muscle compared to the energy put into the system, known as metabolic cost in biological muscles. [%]
8. Actuation frequency - The frequency range of actuation cycles using the system's method of excitation. [Hz]
9. Stroke - The maximum displacement an actuator can achieve [m]
10. Life cycle - The time or number of actuation cycles in which it takes for the actuator to degrade such that it cannot perform its intended purpose to specified standards.

As well as the commonly used medical/biological muscle metric:

11. Maximum isometric contraction force - the maximum force a muscle can apply without changing strain. This is also related to the ratchet-like mechanism and muscle locking where a muscle can apply a much larger force in a static state, as seen in the myosin binding[75].

Other qualities of muscle should be quantified on a case by case basis depending on the artificial muscle technology being investigated. For example, a major issue with dielectric elastomer actuators is the excitation voltage required for actuation is too large for many applications. Hence, excitation voltage could be another parameter considered for some electroactive artificial muscles.

Some of the biological muscle metrics have been quantified by previous research as seen below:

- Energy density - energy densities ranging from 0.4 - 40 $J.kg^{-1}$ [76].
- Power density - power densities ranging from 9 - 284 $W.kg^{-1}$ [77]
- Actuation frequency - natural actuation frequencies ranges 1 to 180 Hz [77].
- Strain - ranging from 5 - 30%[78].
- Efficiency - Thermodynamic efficiency of human muscle is typically between 20-35%[79]. However other biological muscle has been seen to reach efficiencies of up to 77%[79].

2.3.2 Muscle Mechanics

Before attempting to recreate a bio-mimetic actuator it is important to acknowledge the numerous simplified electro-mechanical system models of parts of the muscle actuation process. These models need to be understood to gain an understanding of the application of biomimetic actuators can be used in assistive soft robotic devices. From here we will present basics of the subject of bio-mechanics.

The stress and strain involved in muscle contraction is more complex than uniform materials and is non-linear. The stress and strain of a passive muscle (i.e. contractile units are not producing internal muscle tension) can be modelled with the following equation;

$$\frac{d\sigma}{d\varepsilon} = \alpha \cdot (\sigma + \beta) \quad (2.1)$$

Where ε & σ are strain and stress respectively. A solution for this is first order ODE is;

$$\sigma = \mu e^{\alpha\varepsilon} - \beta \quad (2.2)$$

Where μ is a free parameter determined empirically. The stress-strain of a passive muscle can be likened to tension being applied yarn. As more strands of the yarn are pulled into tension the stress increases, then as the last strands are brought into tension a maximum stress is reached, until the yield stress is reached. Linear approximations can still be made over regions of elongation depending on accuracy required for application. The stress-strain of an active muscle (i.e. when it is tetanised) is approximated to a piece-wise quadratic function or bell curve. It is important to note that the stress for both active and passive muscle is zero when the strain is less than 0.4, demonstrating the yarn-like nature of the muscle stress-strain as shown in Figure 2.6.

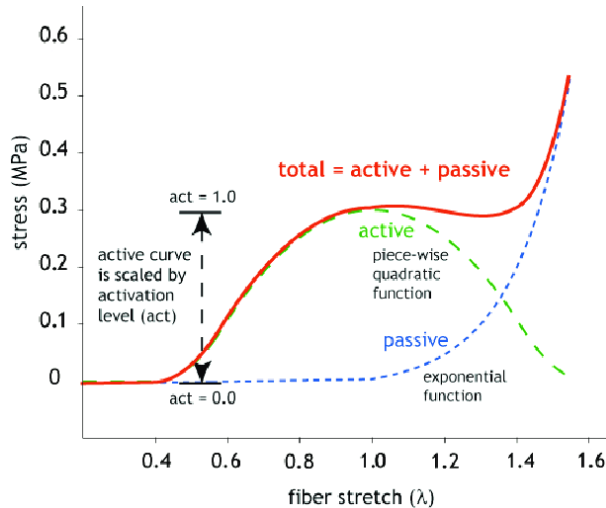


FIGURE 2.6: Stress and strain of active and passive muscles (© J. Teran | ACM 2003)[10]

Hill's muscle models commonly refer to a mechanical three element model [80] composed from, one parallel non-linear spring element, one series non-linear spring element, and a contractile unit.

2.3.3 Electrical Muscle Models

Similar to EAP-based artificial skin and artificial muscles, biological muscles also require electrical stimulation to function. The main method for providing an artificial electrical stimulation to a muscle, to simulate the signal a motor neuron would give to a muscle, is functional electrical stimulation (FES). Due to the biochemical nature of the motor neuron signal transport and the purely electrical stimulation provided by the FES device, the process isn't as efficient as the naturally occurring electro-chemical muscle activation, often resulting in increased muscle fatigue when compared to equivalent voluntary muscle contractions [81]. FES applies a voltage across between two electrodes on the user's skin above a specific muscle. The voltage simulates the signal form and frequency of action potentials between 4 - 12Hz[82]. The threshold for a muscle action potential to cause a muscle contraction is approximately 70 mV [83]. To artificially sense an intended muscle contraction electromyography (EMG) can be used. EMG also commonly uses two electrodes on the surface of the skin above a desired muscle. This EMG signal can be used as a sensor input for joint pose estimation. EMG senses the action potential impulses conducted along motor neurons to the muscle. There are many models for limb motion and EMG- and FES-based therapies [84-87].

2.4 Artificial Muscle Technology

There are many types of electrically actuated artificial muscles technology. Artificial muscle actuator technology that has gained particular interest in recent years include, the ionic polymer-metal composite (IPMC) actuator, the hydraulically amplified self-healing electrostatic (HASEL) actuator, magnetorheological elastomer (MRE) actuators, and dielectric elastomer actuators (DEAs). Each of these having qualities very similar to that of biological muscle usually with a trade-off in actuation response time, actuation force, and actuation strain for their various possible topologies. This section gives a brief overview of four state-of-art soft electromagnetically driven actuator technologies.

2.4.0.1 Ionic polymer–metal composite actuator

Ionic polymer-metal composite actuators (IPMCs) are soft actuators that can be actuated at a much lower excitation voltage than DEAs, commonly less than 10V. IPMCs are also desirable as artificial muscles they have shown large bending deformations, simple to fabricate, light weight and thin in design, and can have a fast actuation response time ($>15\text{Hz}$) at small displacements[88]. IPMCs also have a high work density and maintain a constant volume during actuation like biological muscles[89]. An IPMC is made up of an ionic polymer interlayer, two electrode conductive layers, and a voltage source. The ionic polymer interlayer allows for ionic transport and is typically made of treated Nafion or Flemion. These materials are typically used as ion exchange membranes so have the characteristics desired for the transporting ions during the actuation of the IPMC actuator. The two electrodes are made of a suitably conductive and flexible material. The interlayer is treated such that it is filled with water molecules and cations, with the chemical backbone of the interlayer being slightly negatively charged. When a voltage is applied across the electrodes the cations are repelled from the cathode and travel towards the anode while the water molecules are displaced in the opposite direction towards the cathode. The ionic polymer then swells as the cations repel each other along the anode side of the interlayer, while the polymer elements on the cathode side effectively shrink[90]. This swelling adjacent to the cathode provides the device's bending actuation.

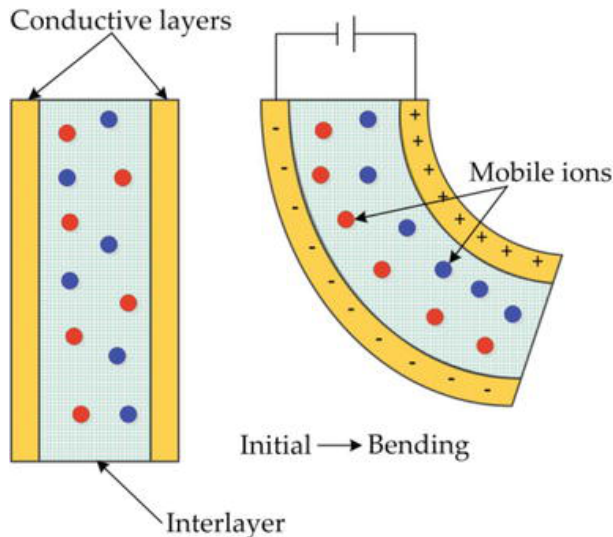


FIGURE 2.7: Diagram of the typical architecture of an IPMC actuator[11] (© 2018 Yanjie Wang and Takushi Sugino)

There are many variations of the design and manufacturing of IPMCs to optimise the actuator for an application as shown by [91]. Although the process of manufacturing IPMCs is simple, it takes a long amount of time (often >48 hours[88]) for the ionic polymer interlayer to absorb the necessary ions and undergo the necessary reactions. There has been much research into the optimal manufacturing of an IPMC [91–93]. The use of additive manufacturing has been used successfully to generate more complex geometries using fused filament deposition[94].

IPMCs can also be used as sensors. When an IPMC undergoes bending due to an external force there is a potential generated across the electrodes, which indicates bending direction and magnitude[95].

Two key deficiencies of current IPMC actuator technology are the maximum force output achievable and the life cycle of the actuator in a dry (non-aqueous) environment. The force output optimisation of IPMCs has been investigated by several researchers, all of which having a maximum actuation force in the milli-newton scale [95–97]. Because the IPMC actuators rely on hydrated ionic transport to actuate this means if the IPMCs are in a dry environment then over time they will decrease their maximum actuation force.

The applications of this actuator is limited to applications requiring a small actuation force and a wet environment. Current applications include flexible catheters [98], small biomimetic robotics [99, 100], aquatic robotics[101, 102], with many other applications yet to be discovered.

2.4.0.2 HASEL actuator

A hydraulically amplified self-healing electrostatic (HASEL) actuator is a recent soft actuator technology developed in 2018[12] which displays many qualities that are better than current artificial muscle technology. HASEL actuators are made up of three main components: electrodes, dielectric fluid, and an elastomeric shell. The electrodes need to be highly conductive, able to handle high electric potential, and can be solid or flexible. Hydrogel electrodes have been proven to be a good material for the electrodes because of their elasticity while still maintaining a high conductivity[103]. In one application the hydrogel material is bonded to a polydimethylsiloxane (PDMS) substrate for mechanical strength and for ease of bonding to the actuator biaxially-oriented polypropylene (BOPP) shell[12, 58]. HASEL actuators use high electric potential across

two electrodes to create an electrostatic force. This force induces a zipping effect which pulls the electrode together from one end to the other as the electric field strength increases. The zipping of the two electrodes pushes the dielectric fluid into the reservoir increasing the pressure which alters the shape of the reservoir bounds providing an actuation motion. When the electrodes have displaced all of the fluid between them the actuation displacement is at a maximum. The electrostatic zipping action allows a large force to be generated due to snap-through transition. Snap-through transition is an actuation instability which has been discussed in previous research as a means of amplifying DEA actuation strain[104]. Recorded efficiency values of HASEL actuators

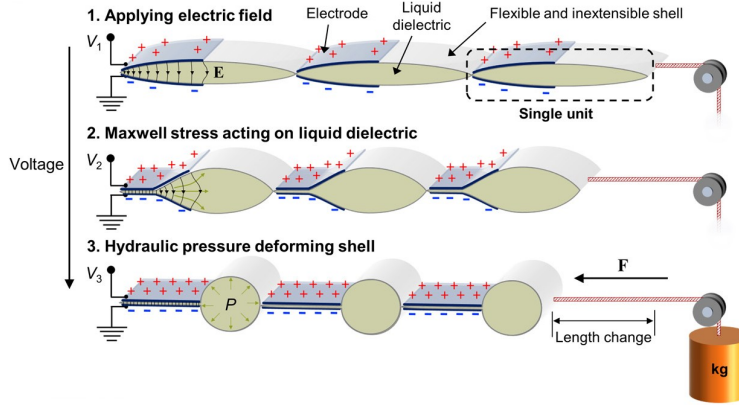


FIGURE 2.8: Diagram of the typical architecture and the contraction stages of a HASEL actuator[12]

ators of 21% are comparable to that of human muscles of 20 - 35% [79]. The actuators have had a frequency response of up to 20Hz. Large strains of 124% have been recorded, but can only be achieved when actuating at a resonant frequency. Strains of up to 79% have been recorded using a linear planar HASEL actuator configuration and DC voltage stepping. Else, strains of only 10% have been recorded for static steady strain[12]. Because there is a relationship between the motion of the actuation and capacitance between the electrodes, this means self sensing can be achieved through the electrodes. Although due to the flexible and fluid nature of the device, modelling of the HASEL is difficult and limited in accuracy.

The simple and commonly used manufacturing process for HASEL actuators is completed in six steps as shown by the diagram below:

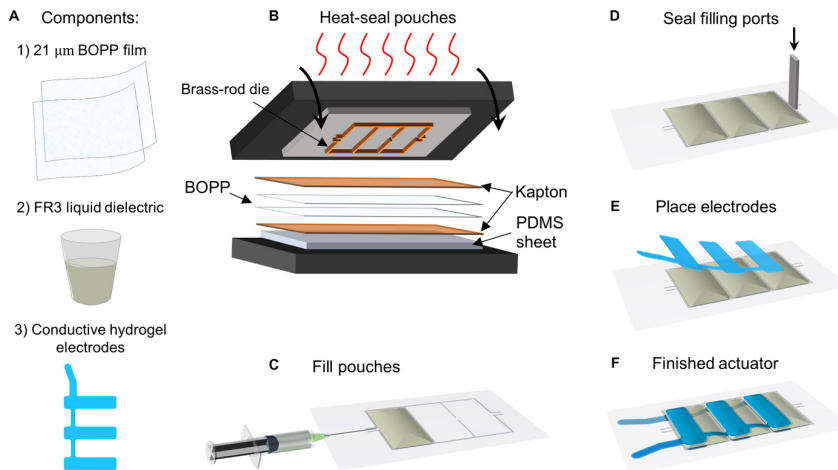


FIGURE 2.9: Diagram of the simplified stages of HASEL actuator production[12]

Other attempts have been made to use polyjet inkjet based additive manufacturing to make the whole HASEL actuator and have been successful with proof of concept, but are yet to be developed from prototype stage[105].

The cyclic life of HASEL actuators are high, because of their self-healing properties. When there is a dielectric breakdown through the liquid dielectric the damage caused is not permanent like when a DE breaks down. The liquid may form some small air bubbles, however these may not effect the operation of the actuator, instead this can increase the likelihood of another dielectric breakdown. The cycle life of the HASEL actuator was seen to be larger than one million with a given torus shaped HASEL actuator[103]. The HASEL technology is promising with a number topologies possible, some topologies include toroidal, planar linear[103], and scorpion metasoma(tail)[106].

2.4.0.3 Dielectric Elastomer Actuators

The dielectric elastomer actuator (DEAs) are often called artificial muscles because they share similar characteristics to biological muscle such as, the large strains achievable, the high elastic energy density, many topologies/configurations achievable, and constant volume during its contraction.

A DEA consists of a dielectric elastomer (DE) film sandwiched between two compliant electrodes. To excite the actuation, a high electric potential is applied to across the electrodes creating an electrostatic force between the two compliant electrodes. This force pulls the two electrodes together applying stress (known as Maxwell's stress) to the elastomer and hence strain parallel and perpendicular to direction of the electrostatic force. When the DEA is contracted the surface area of the electrodes increases and the thickness of the DE decreases causing a change in capacitance and Maxwell's stress. A dielectric elastomer actuator can be modelled

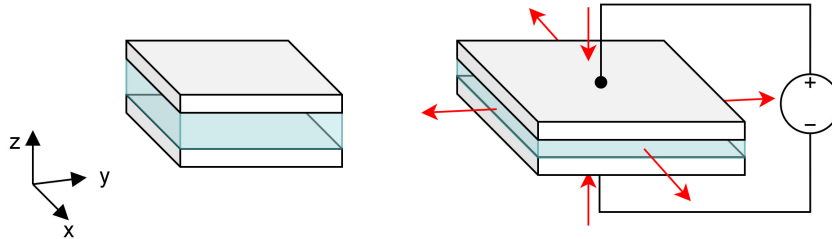


FIGURE 2.10: DEA with two compliant light-grey electrodes and a transparent light blue dielectric elastomer. Showing deformation without and with a voltage applied across the electrodes.

as a flexible parallel plate capacitor in its simplest form. Using this we can determine the electrostatic pressure to be:

$$\sigma_{es} = \epsilon_0 \epsilon_r \frac{V^2}{z^2} \quad (2.3)$$

Where σ_{es} is the electrostatic pressure, ϵ_0 and ϵ_r are the vacuum and relative permittivity constants, V is the voltage potential applied across the electrodes and z is the thickness of the DE. The electrodes used for a DEA need to be made of a conductive material, but require similar elasticity to the dielectric material. An ideal material for these electrodes would have high conductivity. This conductivity would change minimally and predictively under large strains. Many composites have been used in practice for these electrodes, with the most common in early development being a silicone rubber and carbon powder composite. However, the unpredictable nature of carbon powder elastomer composites has lead to research into many

other materials/silicone additives such as hydrogels, graphene sheets, metallic nanostructures, carbon nanotubes, liquid metal[107–110]. The ideal material for the dielectric elastomer should have a high elastic modulus and a high electric breakdown voltage. The elastic modulus needs to be sufficiently high so that less electrostatic pressure can create a larger strain. While the breakdown voltage of the material needs to be sufficiently high such that the material will not break down at the maximum desired strain. If a material can be found with a high enough electric breakdown strength at a smaller thickness than current research prototypes then a higher stress can be achieved giving a larger or equivalent actuation force at a lower voltage.

Many other topologies exist to generate different actuation motions using the same electrostatic pressure generation principle. These include actuator topologies such as stack[111, 112], helical[113], bending[114], lens[115], cylindrical, and rolled shaped actuators[116]. Each of which having a range of applications.

DEAs are often fabricated in a laboratory environment using a pre-strained elastomer. The pre-straining accomplishes four key qualities; stores elastic strain energy, ensures DE is planar within the bounds of the jig, controls the initial thickness of the DE, and puts the DE in an optimal stress-strain region, often taking advantage of elastomer hyper-elasticity. There is no standard practice for the fabrication of DEAs, other methods such as additive manufacturing have also been explored to generate more complex geometries and to increase production speed[117, 118].

As well as actuating, DEAs can also be used for sensing. DEAs can be used as sensitive capacitive sensors, where any strain applied to the DE will relate to the effective capacitance between the two electrodes[29, 119, 120].

Currently dielectric elastomer actuators all require voltages within the kilo-volt range to generate an adequate stress and strain for a range of applications. A key problem encountered by researchers designing DEAs is the trade-off between actuation force and strain magnitude [111]. This high voltage requirement may deem the technology dangerous for use where there is a possibility that a human may come into physical contact with the high voltage electrodes.

2.4.0.4 Magnetorheological Elastomer

Magnetorheological elastomer (MRE) actuators, also known as magnetoactive soft materials (MSMs), are a relatively new form of actuator however the theory reinforcing operating principle has been known since at least the 1980s [121]. The structure of an MRE actuator generally consists of a ferromagnetic elastic composite and a driving magnetic field. An example of this is a composite of iron-carbonyl powder and PDMS. The operating principle of MREs is that magnetic flux travelling through the MRE will change mechanical characteristics within the elastomer (i.e. stiffness or displacement of the body). The operation of a MRE actuator is similar to a DEA however instead of having an electric field cause a contraction it is a magnetic field causing a deformation. An MRE is typically made of silicone rubber containing magnetic ferrite based particles uniformly distributing throughout its volume. This kind of actuator is current controlled and can hence operate at a low voltage. This helps mitigate the risk of electric shock of a device in close proximity to humans (unlike HASEL actuators and DEAs). A key issue with using magnetorheological elastomers as soft actuators is that they require heavy gauge conductors for the high current they require for generating a magnetic field. The high current requirement means that actuators have only been created that have a solid electromagnet driving a soft MRE[122].

When manufacturing MREs, uncured liquid silicone rubber is mixed with magnetic (commonly carbonyl iron) particles to form a 3 dimensional matrix of crosslinks with the magnetic particles

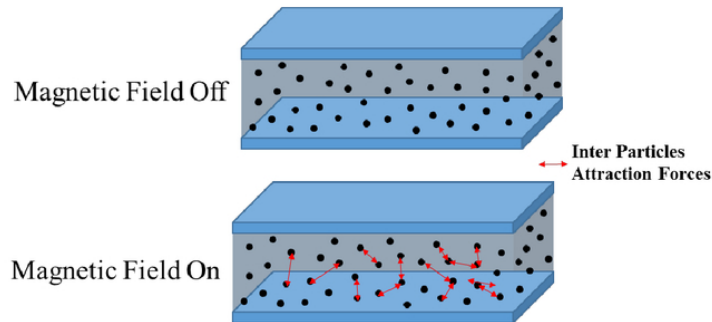


FIGURE 2.11: Diagram showing MRE contraction actuation when a magnetic field is applied[13]

fixed between the crosslinked polymers. A core issue when creating an MRE is the agglomeration and corrosion of magnetic particles due to residual water within the mixing operation. The magnetic particles can be processed to have a hydrophobic quality to mitigate this issue [123, 124]. During the curing process a magnetic field can be applied to align the particles within the elastomer to control the particle isotropy[124, 125].

There have been attempts to use additive manufacturing to make MREs[124, 126], however the method described has not optimised the structure of MRE for any application and the particle dispersion throughout the MRE has not been proven uniform throughout the print volume.

The current applications of MRE actuators are limited, however magnetorheological fluid (MRF), is a fluid which becomes more viscous with an applied magnetic field as currently has many modern applications. This fluid substance is largely used in applications where damping control is desired such as vehicle suspension[127], medical assistive devices[128] and helicopter seat damping [129]. Potential MRE actuator applications include fluid valve control[122] and active vibration control similar to that mentioned for MRFs[127].

2.5 Soft Conductive Particle Piezoresistive Composites

Soft sensors and actuators require low-stiffness materials for their active sensing/actuation domains. The requirement of softness is governed by the mechanical modulus values depend on the application requirements. The use of conductive particle elastomer composites is explored in this work due to the customisability of the electromechanical characteristics. A core part of this thesis is understanding the behaviour of conductive particle elastomer composites for their use as a range of EAP-based sensing and actuating devices. The characteristics that make conductive particle elastomer composites (CPECs) ideal for soft sensor and actuator devices often include, low stiffness, controllable conductivity, controllable piezoresistivity, mouldable, 3D printable, low toxicity, durable, inexpensive, easy to obtain, simple fabrication process, and sustainable[124, 130, 131, 145].

2.5.1 Fabricating Conductive Particle Elastomer Composites

Before exploring the known conduction and piezoresistive mechanisms and models for CPECs, it is important to understand how the fabrication process of a CPEC may affect its physical structure.

CPECs are made by dispersing conductive particles through a curable liquid elastomer matrix. To change the electromechanical properties of the material, the dispersion of the conductive

particles throughout the matrix can be optimised through various methods. To minimise the agglomerations of primary conductive particles often a sonication step is completed. This involves a mixture of the conductive particles and a liquid, usually in the form of a solvent, to be placed in a sonication bath. The sonication bath performs a frequency sweep whereby the resonant modes of the agglomerates are met causing separation of the agglomerates into their primary particles [6]. The degree of dispersion is governed by the time in the sonication bath, the sonication frequencies, and sonication amplitudes [6]. This sonication usually occurs before the particles are added to the elastomeric matrix due to the large viscous damping effects of liquid elastomers. The next step involves mixing the dispersed conductive particles throughout the liquid elastomer, this can be done using a variety of mixing methods, including a planetary mixer, magnetic mixer, screw mixer, static mixers, amongst others [6]. During the mixing process often the liquid solvent used in the dispersion stage is evaporated, leaving only the curable elastomer and the conductive particles. When sufficient mixing of the liquid elastomer and conductive particles have been completed the material is formed into a desired final shape using advanced additive manufacturing methods [6] or traditional moulding [6] or film making techniques [6]. During the moulding process the material undergoes a form of curing, such as UV curing, catalysed curing, or moisture curing [6]. If the composite material has not already been integrated into a device containing electrodes and other mechanical support structures these are integrated at the end of the process [6].

2.5.2 Modelling Conduction mechanism

The typical fabrication process stated in Section 2.5.1 for CPECs shows that the dispersion of conductive particles will always vary.

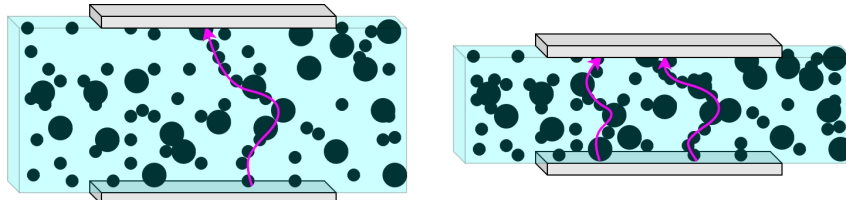


FIGURE 2.12: Two grey highly conductive electrodes across a CPEC cuboid showing enlarged black conductive particles within a blue polymer matrix. Left: An uncompressed CPEC. Right: A compressed CPEC.

Some of the physical features of these conductive percolation networks can be quantified and directly relate to the macro-level electromechanical properties of the material. Such characteristics of a conductive percolation network include:

1. Conductive particle(s) used
 - (a) Aspect ratio [132, 133]
 - (b) Inherent particle conductivity
2. Conductive particle dispersion [131]
 - (a) Inter-particle distance distribution
 - (b) Particle agglomeration distribution [134]
 - (c) Isotropy/anisotropy [135]
 - (d) Sedimentation [136]

3. Elastomeric matrix
 - (a) Viscosity
 - (b) Elastic modulus
 - (c) Dielectric permittivity
4. Impurities
5. Voids

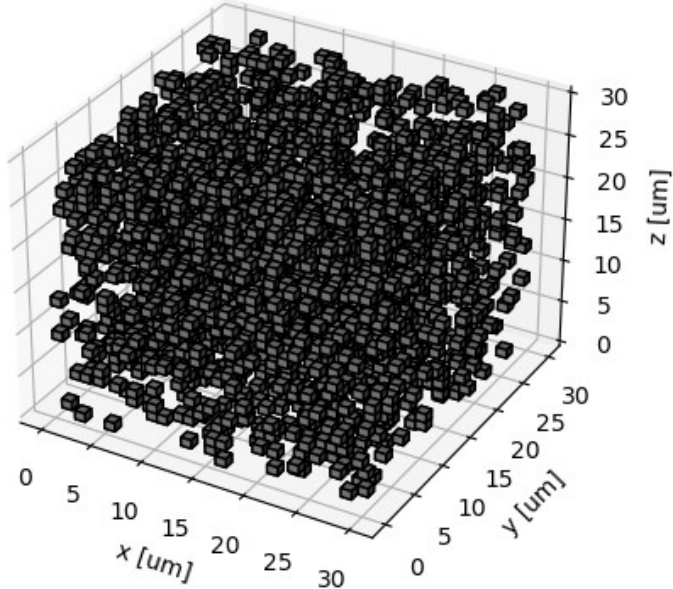


FIGURE 2.13: Example of a randomised cube percolation with a volume percentage of 8% of particles

Microscale models for CPECs and the relationship between particle and electric charge motion are often computationally heavy, overly idealised, and non-invertible [137]. A microscale model example can be seen in Figure 2.13. However, microscale modelling of CPECs may give insight into understanding complex physical phenomena that may relate to the macroscale models made for CPECs. An alternate method for modelling CPECs is the formation of macroscale models[138].

Electrical DC conduction through a CPEC occurs via two main mechanisms, Coulomb conduction and quantum tunneling [139–142]. Coulomb conduction uses the conduction band electrons are shared by adjacent atoms allow conduction throughout chains of cascading conductive particles. The second mechanism of conduction is through quantum tunneling which is stochastic in nature and allows for conduction through insulative boundaries between the percolative network of conductive particles [143, 144].

Electrical AC conduction can occur through a CPEC through capacitive means depending of particle spacing with a decrease in reactance becoming more prominent for composites near the percolation threshold[145].

Chapter 3

Giving Artificial Muscles the Sense of Touch

The content from this chapter is contains content from the manuscript published in the proceedings of Electroactive Polymers Actuators and Devices XXVI.

ABSTRACT

Dielectric elastomer actuators (DEAs) commonly use flexible conductive electrodes to apply an electric potential to actuate. Depending on the material used, these electrodes often possess predictable piezo-resistive properties. Combining electrical impedance tomography (EIT) with a dielectric elastomer actuator (DEA) is investigated in this work to map compressive forces occurring throughout the electrode surfaces. This technology could allow for enhanced closed-loop control of electro-active actuators, broadening their already extensive set of applications. This deformation mapping system also has potential to be used with other piezoresistive materials opening up applications requiring a range of hardnesses and pressure sensitivity. With the material used in this work, the DEA-EIT device has an inherent trade-off between actuation and pressure mapping accuracy driven by the compliant electrode thickness of the DEA. It has been shown experimentally that the simultaneous actuation and EIT mapping can be achieved on the designed hybrid DEA-EIT device. The DEA-EIT device exhibited actuation strains of 2.5 % with a mean center-of-mass detection error of 1.66 ± 0.17 mm for 2 mm thick DEA electrodes. Future designs will ensure that applications requiring human-like manipulation can be designed, ranging between biomedical implant devices, agricultural processing equipment, soft optics, and bio-mimicked robotic aquatic life.

3.1 INTRODUCTION

Fine motor manipulation, pressure sensitivity, and pressure mapping are some core attributes of skin and muscle tissues when innervated to the brain. These functions can be emulated and combined with two core technologies; Dielectric Elastomer Actuators (DEAs), and Electrical Impedance Tomography (EIT) based pressure mapping.

DEAs have been used to mimic biological muscles in many applications, because of the technology's likeness to biological muscle in terms of elasticity, energy density, and various potential

shapes/topologies [146–148]. In previous research, it was determined that pressure mapping similar to that of human mechanoreceptors could be emulated using EIT with a piezoresistive nanoparticle elastomer composite (PNEC) in a planar sheet format[14]. The key qualities of the EIT-based sensing platform were that; pressure estimates could be obtained, and the pressure could be mapped and the spatial performance quantified[15]. Like DEAs, this sensing technology has a likeness to human tissue in terms of mechanical characteristics such as elasticity, and the potential of various topologies.

Alongside the visual and other sensory feedback, animals receive when actuating muscle tissue, pressure-sensitive mechanoreceptors are present within the muscle tissue and soft skin tissue to aid control the extent of a muscle contraction. This forms a multi-sensor closed-loop control system with a complex biological control regime. This work is looking towards creating a closed-loop control system which utilises a DEA-based artificial muscle and an EIT-based artificial skin all contained within monolithic bodies. Applications such as the ones conceptualised in Figure 3.1 can be designed with the use of DEA-EIT integrated technology.

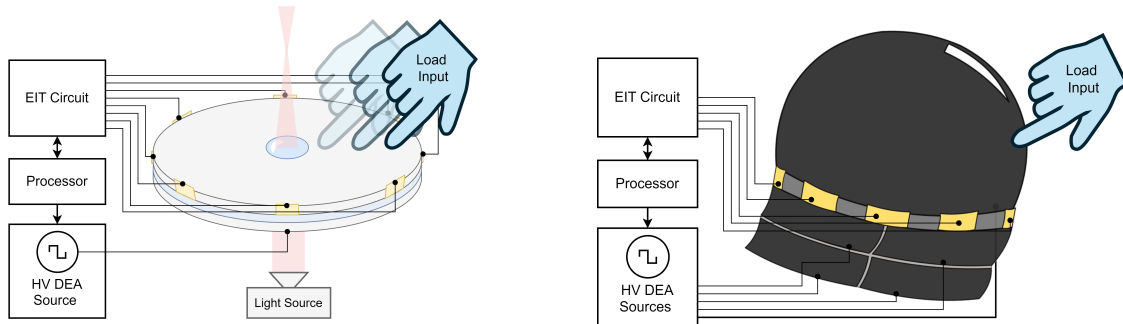


FIGURE 3.1: Potential future application of the DEA-EIT device topology. Left: EIT sensor input DEA controlled optical lens. Right: Pressure mapping sensitive skin for a DEA propelled jellyfish soft robot.

3.1.1 Background

The fundamental principles and a brief explanation of the state-of-the-art of each DEA and EIT-based sensor technologies are given in this section. A review of pressure mapping devices with actuation capabilities was then completed. At the time of completing this work, no literature had been found regarding the combination of these two technologies using PNEC electrodes on a DEA for simultaneous execution of sensing and actuation events.

3.1.1.1 Dielectric Elastomer Actuators

DEAs are often referred to as artificial muscles because they share similar characteristics to biological muscle. Although commonly used as an actuator, this technology offers versatile applications as an energy generator[149–151] or sensor and provides attractive features such as high energy density, large displacements, and fast response times. DEAs have been proven to produce strains larger than 1600 %[104] which is significantly larger than that of regular biological muscle. However, large DEA strains can often be at the cost of actuator instability and a low effective force. DEAs have a high work and power density comparable to that of biological muscle and have been found experimentally to have energy densities of around 3.4 J.g^{-1} and theoretically an order of magnitude more[151, 152]. A dielectric elastomer actuator (DEA) is a form of soft robotic actuator that induces deformation with an applied electric field.

A simple common configuration of DEA is a circular parallel plate capacitor, which consists of a thin elastomer sheet between two compliant conductive electrodes, as shown in Figure 3.2.

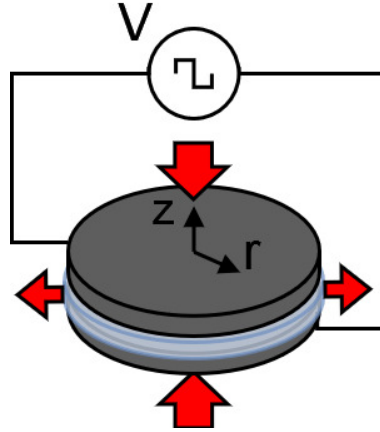


FIGURE 3.2: A circular DEA exemplifying its actuation principle.

When a voltage is applied to the compliant electrodes, an electrostatic force arises between the electrodes causing the dielectric elastomer (DE) membrane to contract by a decrease in thickness and an increase in area. The resulting actuation is controlled by changing the applied voltage. The region encompassing the two compliant electrodes and the DE portion sandwiched between them is called the ‘active region’, i.e. where the electric field is largest. For a simple DEA such as the one shown in Figure 3.2, a simplified formula for the electrostatic force on the compliant capacitor electrodes is given in Equation 3.1.

$$\sigma_{es} = \varepsilon_0 \varepsilon_r \frac{V^2}{z_{de}^2} \quad (3.1)$$

Where σ_{es} is the electrostatic stress, V is the applied voltage, z_{de} is the DE thickness, ε_0 is the permittivity of free space, and ε_r is the relative permittivity constant of the DE, which is a function of strain[153–155] and applied voltage[30]. This can be expanded to estimate the DE strain, $S_{z_{de}}$, using the bulk modulus, K , of the DE as shown in Equation 3.2.

$$S_{z_{de}} = \frac{\sigma_{es}}{K} \quad (3.2)$$

Designing a DEA for practical applications is often highly constrained by three key modes of failure as well as the parameters of the constituent components. A common mode of failure is the electromechanical instability of the elastomer. With increasing voltage, the DE compresses until the voltage exceeds the critical point at which dielectric breakdown occurs. At the point of failure, the DE membrane experiences a surge of electrical current, permanently changing the DE insulative properties. The second mode is a loss of tension in the elastomer when an applied voltage is large and the axial force provides an excessively large compression. The stress in the DE may cause the plane to lose tension such that the elastomer no longer actuates as expected, if at all. Often resulting in visible wrinkles in the DE. The third mode is a physical rupture of the elastomer due to stretching beyond the DE’s yield strength [156]. A key benefit of DEA technology is its potential to be fabricated into various topologies depending of the desired application including, parallel plate[104], roll[157], tube[158], helical[159], and conical geometries[160].

3.1.1.2 Soft EIT-based Pressure Mapping

A soft EIT-based pressure mapping sensor has the ability to estimate the magnitude and location of deformation events in a planar PNEC material. The hardware required usually consists of a piezoresistive sensor domain with attached boundary electrodes, EIT driver electronics, and a reconstruction processor. Boundary electrodes allow a non-invasive method of pressure mapping without compromising a monolithic piezoresistive material. Several researchers have created an EIT-based pressure mapping sensor using a range of piezoresistive domains and custom or lab-based hardware [15, 51, 161–164] .

Electrical impedance tomography or EIT is most commonly used in medical pulmonary research to give a cross-section of a human thorax in real-time at a frame rate of 50 Hz, as shown in the two commercially available medical EIT machines the Pulmovista500 (Draeger, Lübeck, Germany) and the LuMon System (Sentec, Lincoln, USA). However, using EIT to map and quantify pressure events has the potential to give a faster frame rate due to the use of DC instead of AC. However, the viscoelastic and resistive nature of the sensor can lower the frequency response of the sensor depending on the piezoresistive sensing domain used. The stages required to generate a pressure image using EIT can be simplified into three core stages,

1. Data acquisition
2. Image reconstruction
3. Inverse force model

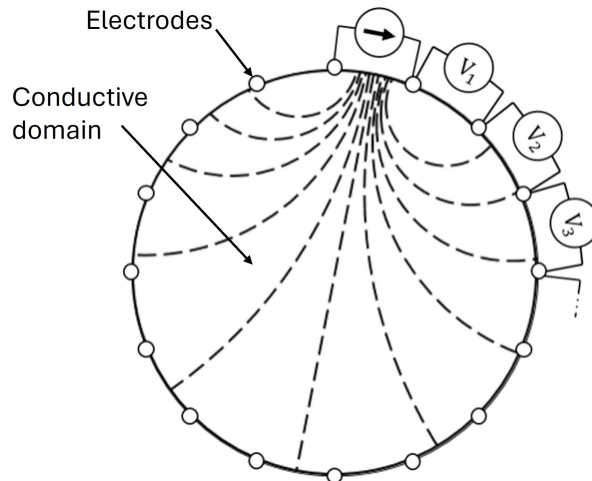


FIGURE 3.3: A 16 electrode circular EIT domain setup exemplifying its electrical function. Where the dashed lines are representative of an applied electric field[14] .

Data acquisition involves an excitation drive pattern to be applied to the piezoresistive sensing domain, which consists of the injection of a known current or voltage through two boundary electrodes connected to the material domain as shown in Figure 3.3. Typically an adjacent electrode drive pattern is used in literature and is also used in this work[161] . Concurrently all voltages at the other boundary electrodes of the material domain are read. Then a known current (or voltage) source is applied to the next set of adjacent electrodes, and all of the other adjacent electrode voltages are read once more. This process is repeated until it has been deemed there have been sufficient readings to solve the inverse problem and generate

a conductance, ρ , distribution estimate of the material domain. Finally, an inverse model converting the conductance estimate of the material domain can be converted into a pressure map using an inverse model.

3.1.2 Simultaneous Pressure Mapping and Actuation

Various researchers have demonstrated and proposed the use of self-sensing DEAs for closed-loop control looking at the one-dimensional deformation of a DEA using their change in capacitance[29, 31, 32, 165]. Multi-degree-of-freedom (multi-DOF) DEA topologies have been created by several researchers [166–169], allowing for a broader range of applications. The complex actuation mechanisms discussed in these papers give rise to the question of having more resolute sensor data for such topologies to aid with the control of such multi-DOF devices.

To sense deformation in multiple dimensions, the current methods used for DEA self-sensing must be altered. To ensure the DEA maintains minimal change to the parallel plate topology, the compliant piezoresistive electrodes can be used and/or altered to be able to determine the deformation of the DEA in more than one dimension. Options for sensing in two dimensions include determining the stretch across the compliant electrode material by measuring the change in resistance of the electrodes diametrically opposed at various angles around the DEA, or adding an extra pressure mapping sensor layer to the DEA stack, or using EIT to map change in resistance of the compliant electrodes. Using diametrically opposed resistance measurements across the compliant electrodes will have limited resolution and is limited in compliant electrode shapes that can be used effectively. Adding another sensing layer to the DEA requires a sensing technology that has a very low elastic modulus, to not hinder the actuation force of the DEA. The limitations given above are why EIT was chosen to sense 2D deformation of a DEA, as it has a relatively high spatial resolution that can be quantified and requires no extra hardware on the DEA body apart from non-invasive electrodes on the boundary of the DEA's compliant electrode(s).

3.2 METHODOLOGY

The DEA-EIT actuator-sensor-hybrid system required the two technologies to be verified and fabricated individually before being integrated to observe the effects of combining the two technologies relative to their independent forms. The following sections discuss the fabrication process for the DEA and EIT systems and then the integration of them both into a DEA-EIT device.

To optimise the actuation and sensing capabilities of the DEA-EIT system different parameters of the design were altered, such as the compliant electrode composite used, DE material used, circumferential electrodes, and magnitude of DE pre-stretch and sizing. The methodology explores the reasoning to certain design choices for the fabrication of the DEA design seen in Figure 3.4.

3.2.1 Dielectric Elastomer Preparation

The fabrication of the DEA used a rigid acrylic frame to attach the pre-stretched elastomer. For simplicity, a circular frame was chosen with the DE at a radial pre-stretch of +10%, i.e. $\lambda_r = 1.1$, as this is well within the DE's more predictable linear elastic region. The circular

acrylic frame of 178 mm inner diameter was fabricated from laser cut acrylic of 4 mm thickness to ensure rigidity.

To achieve uniform stretch of the elastomer sheet, a toroidal shower hose mechanism was placed on the relaxed sheet of 4910 VHB tape (3M, Saint Paul, USA), which would act as a pre-stretcher annulus. The toroidal mechanism has an axis of rotation along its circumference as shown in, giving the ability to roll and stretch the elastomer equiaxially to the desired pre-stretch.

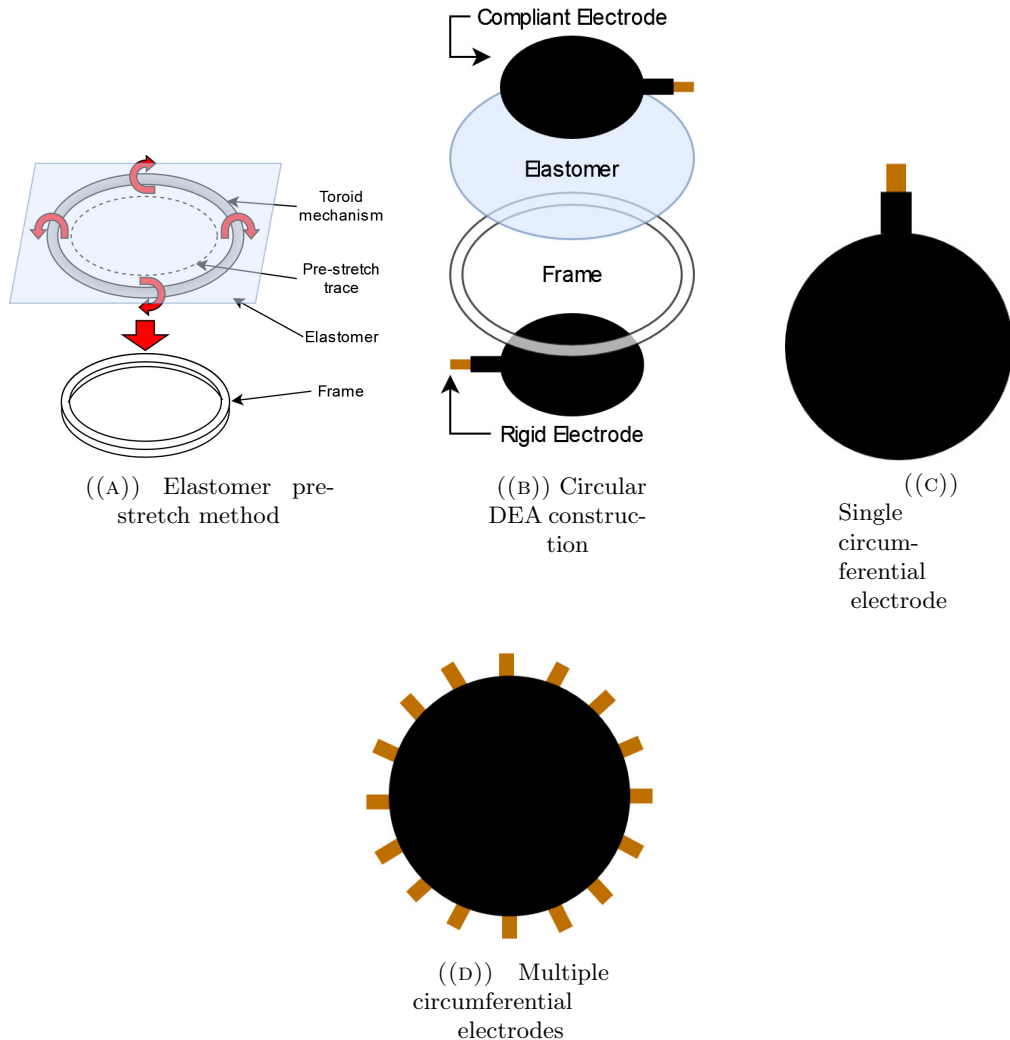


FIGURE 3.4: Mechanical fabrication of the circular DEA-EIT platforms

3.2.2 Compliant Electrode Fabrication

Compliant electrodes (or active area) were fabricated using acrylic moulds of varying dimensions. Three thicknesses, z_{ce} , of the compliant electrode were fabricated, 0.5 mm, 1 mm and 2 mm, with two circular compliant electrodes of 100 mm diameter. Different thicknesses were explored as this would vary the actuation and sensing performance of the electrodes.

Two compliant electrode mediums were used in this work, carbon black (CB) powder and a carbon black silicone rubber (CBSR) composite. Compliant electrodes solely made of CB powder have been used for DEAs in previous literature[170–172], hence this work uses the

same compliant electrode type to generate reference data. The CB powder was used to make a single circumferential electrode configuration DEA as a reference to compare to the following DEA-EIT experiments. The CBSR composite was used to make both single (Figure 3.4(b)) and multiple (Figure 3.4(d)) circumferential electrode configurations of DEAs. The CB powder used in all of the compliant electrode samples was Vulcan XC-72 powder (Fuel Cell Store, Bryan, USA). The CBSR composite had 8% CB by weight mixed with DragonSkin 10NV silicone rubber (Smooth-On, Macungie, USA). This composite is a piezoresistive medium that has proven useful for EIT pressure mapping and sensing in previous work[15] , and DEA actuation[170, 171] .

Using the liquid silicone rubber, the CBSR composite mixture was formed by combining part A of the silicone solution and 8 wt% CB and mixing by hand for 10 s. The mixture was then placed in the ARV-310PCE planetary vacuum mixer (Thinky Inc., Tokyo, Japan) to complete a mixing cycle with 500 RPM for 45 s followed by a cycle with 800 RPM for 45 s. In the same mixing container, part B of the silicone solution was added to the mixture and stirred by hand for 10 s and immediately the same mixing cycle in the planetary mixer was completed again. After the cycle was completed, the composite was poured into the mould with attached circumferential copper tape electrodes. The CBSR mixture was then placed in an oven at 80 °C for 4.5 h to ensure the composite was sufficiently cross-linked.

Two types of compliant electrode configuration have been fabricated in this work, single circumferential electrode and multiple circumferential electrodes. The single circumferential electrode configuration was purely for testing DEA actuation. The multiple circumferential electrode configuration consisted of 16 evenly spaced circumferential electrodes. The multiple circumferential electrode configuration was for testing both EIT-based pressure mapping and actuation functionality of the DEA. Prior to curing the compliant electrode in a circular mold, the conductive copper tape circumferential electrodes were placed into the mold. The width of the circumferential electrodes were 8 mm. The circumferential electrodes were placed with a 3 x 8 mm area embedded in the compliant electrode circumference edge with the rest of the circumferential electrode protruding for easy access to external electrical connections.

3.2.3 DEA Hardware

The excitation voltage for the DEA was provided by a Trek 610E high voltage supply (Advanced Energy Industries, Fort Collins, USA) providing a maximum voltage output of 10 kV DC. The DEA was placed in a clear insulated box with the high voltage supply leads attached to the rigid copper electrodes of the DEA. An iPhone 11 camera (Apple Inc., Cupertino, USA) was used to obtain images of the radial compliant electrode strain as shown in Figure 3.5. The current limit of the high voltage supply was set to its maximum of 2 mA to ensure the DEA actuation response was not limited by the charging of the compliant electrodes.

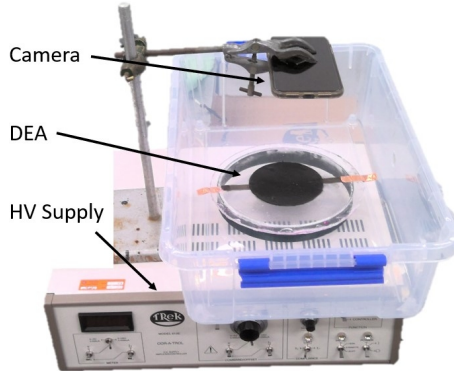


FIGURE 3.5: DEA excitation and measurement setup

3.2.4 EIT Hardware

The EIT hardware allows for data collection to reconstruct a conductance map of the piezoresistive composite used as compliant electrodes in the DEA samples. The hardware required for this function, shown diagrammatically in Figure 3.6, includes a 2634b source measure unit (SMU) (Keithley, Solon, USA), a custom 4:16 multiplexer (MUX) PCB, an ESP32 development board, a Cartesian force applicator, and a reconstruction and control computer.

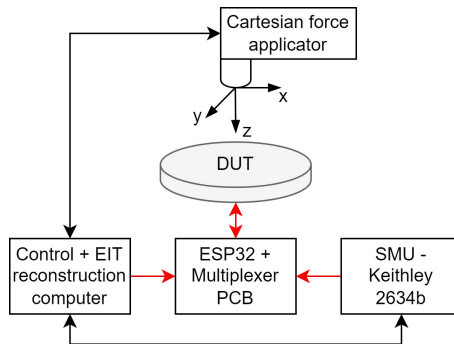


FIGURE 3.6: Architecture of the force applicator and EIT measurement system [15]

The SMU provides a constant current value of 1 mA and reads a series of voltages through the MUX PCB required for the EIT drive pattern. An adjacent electrode EIT drive pattern was used for EIT through the circumferential electrodes of the compliant electrode. The MUX PCB and SMU are controlled by the control computer. Once the data for each image reconstruction has been gathered the control computer was also used for the reconstruction of the conductivity maps of the compliant electrodes. The Cartesian force applicator is made up of a MK3s 3D printer (Prusa, Prague, Czechia) integrated with a loadcell and fabricated applicator tip to apply loads and hence generate data for pressure magnitude and localisation quantification.

3.2.5 Experimental Method

Before attempting to have simultaneous DEA actuation and EIT sensing occur in the same device, each system had to be tested independently. First DEA strain voltage relationships were explored followed by EIT-based pressure mapping of the DEA electrodes. Finally the same

samples used for EIT testing were subsequently integrated into a DEA device for simultaneous functional testing.

3.2.5.1 DEA Validation

DEA actuation strain measurements were taken from voltages 5 kV to 10 kV in 1 kV increments. The SNR of strain measurements of the DEA excited with voltages < 5 kV were deemed to be too low to generate meaningful data. The excitation voltage was toggled between on and off states waiting for the strain deflection to reach a steady state for the strain measurements. Five radial strain images were captured and measured. The measurements were then averaged to minimise error and determine the radial strain uniformity. The radial strain was found by measuring the radial change of the circular compliant electrodes between relaxed and electrically contracted states. From the radial compliant electrode strain the planar and thickness deformation of the DE was estimated. The DE is assumed to be incompressible and have a Poisson's ratio, ν , of 0.5. The adhesion between the compliant electrode and the DE is assumed to be perfect to simplify the model used here. The thickness strain, $S_{z_{de}}$, is calculated using Equation 3.3[170] and 3.1.

$$S_{z_{de}} = \frac{1}{(S_{r_{ce}} + 1)^2} - 1 \quad (3.3)$$

Where S_r is the radial strain measured from the equi-biaxial actuation. The elastic modulus of a hyperelastic material such as VHB is often defined as a non-linear function of strain and strain rate[173]. In this work a linear bulk modulus value, K , of 142 kPa was used. The bulk modulus was determined by doing a meta-analysis and averaging of the elastic moduli determined at steady state 10% strain for VHB 4905 material in previous literature[32, 173, 174]. The relative permittivity, ϵ_r , used in Equation 3.1 was approximated to be 4.5 ± 0.2 due to pre-strain effects seen in literature[153–155, 175].

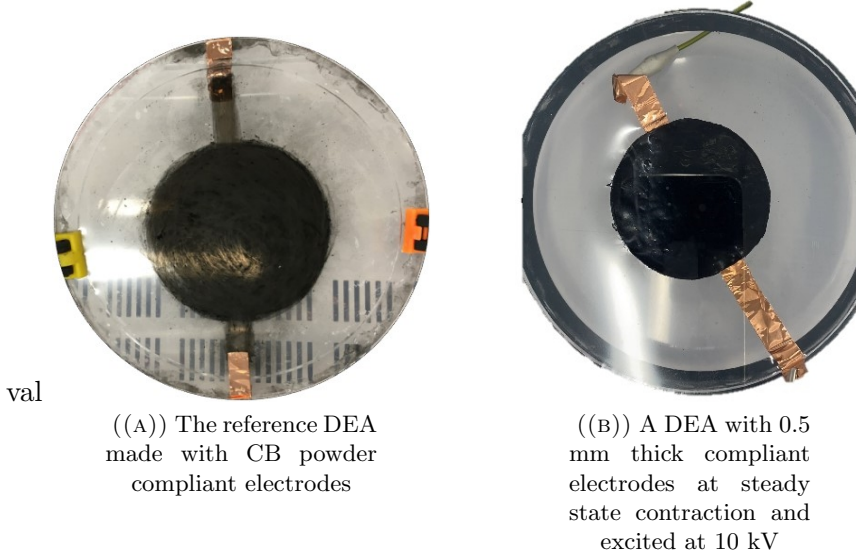


FIGURE 3.7: The two DEA compliant electrode material types used in this work.

3.2.5.2 EIT-based Pressure Mapping on DEA

A load sequence was devised to ensure that forces in various locations of the compliant DEA electrode could be localised using EIT. A similar test procedure used in previous works[15?] was applied to the three individual compliant electrodes thicknesses, z_{ce} , of 0.5, 1, and 2 mm. Nine load application points were determined on the material at three distinct radii as shown in Figure 3.8.

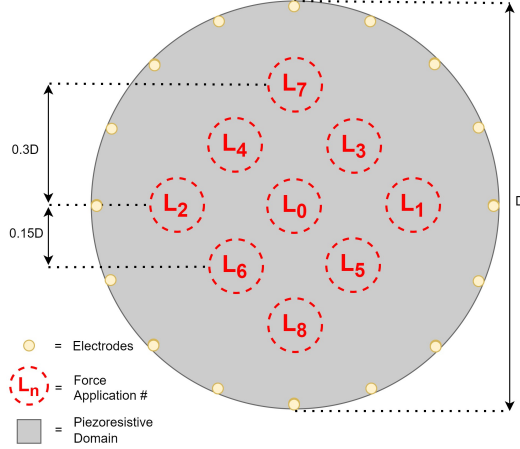


FIGURE 3.8: Load application areas used for compressive stress testing in order of application[15] .

A Cartesian force applicator applied the loads with varying strains in the nine locations. Once the compliant electrodes had undergone the first load application tests, they were applied to each side of a DEA and tested again using the same sequence of nine loads. Compressive strains from 0 to 30% of the electrode thickness in 5% increments were applied when to each of the load points using a flat circular 13 mm diameter force applicator. When applying the compressive strain to the compliant electrodes, a slow strain rate of $16.67\%\text{ s}^{-1}$ was used to minimise piezoresistive transient phenomena. After completing the load tests on individual compliant electrodes the compliant electrodes were attached to the DE surface. Next the load test was completed again to the DEA placed on a flat surface.

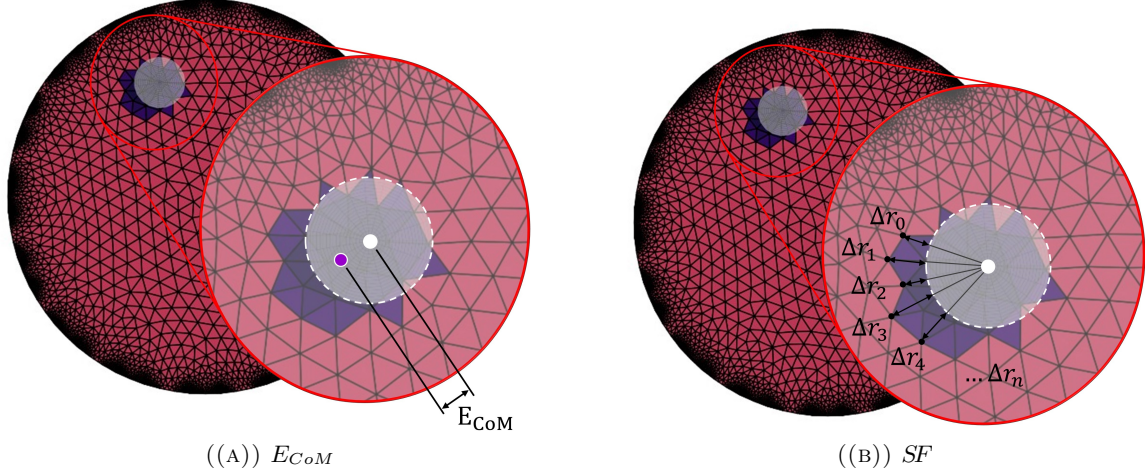


FIGURE 3.9: The two spatial performance metrics used for determining accuracy of blob as a load area estimate, where the transparent white circle is the actual load area and the dark purple elements are the load estimate area.

$$SF = \left(\sum_n^i \Delta r_i^2 \right) / n \quad (3.4)$$

After gathering all of the experimental data from applied loads, the data was used to generate EIT conductance images. To form blobs as estimates of the applied loads, post-processing was completed by applying an 85 % threshold mask to the EIT image. These blob images were subsequently analysed using two spatial performance metrics, the center-of-mass error, E_{CoM} , and the shape fit, SF , as exemplified in Figure 3.9. The E_{CoM} values were determined by calculating the difference between the CoM of the actual load and the blob representing the load estimate. The SF was determined by calculating the radial mean square error between all of the, n , perimetal nodes of the blob load estimate and the actual load circumference, as taken from the CoM of the actual load area.

3.2.6 Simultaneous Actuation and Pressure Mapping

The DEA-EIT device was tested for simultaneous actuation and pressure mapping to highlight the functional limitations that arise with such a device. Simultaneous actuation and pressure mapping involves an excitation voltage is applied to the DEA whilst completing EIT to the grounded DEA electrode.

To ensure that the EIT electronics are able to operate during transients or dielectric breakdown events, an intermediary 20 V Zener diode array and a current limiting resistor, R_{lim} , were added to the system as shown in Figure 3.10.

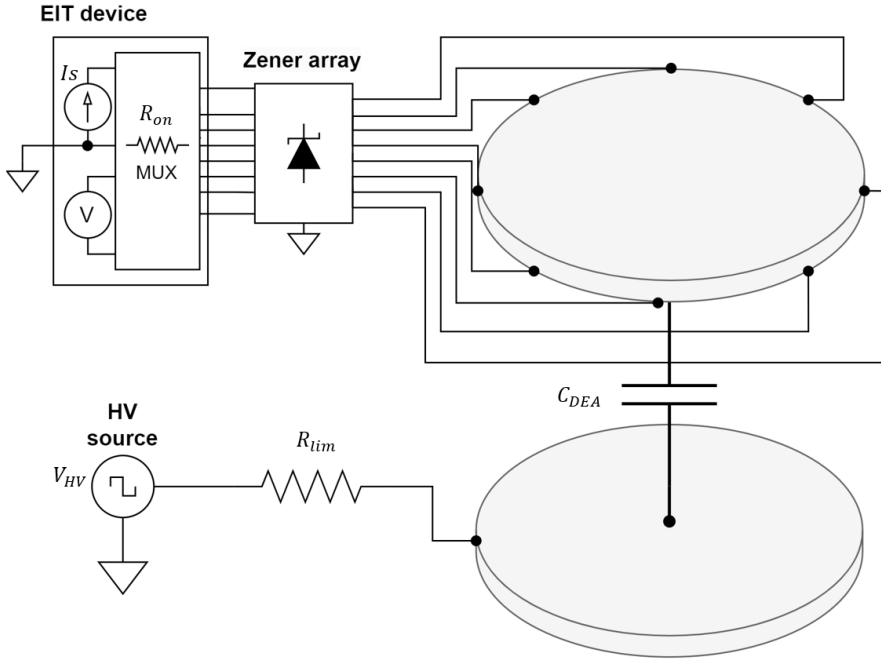


FIGURE 3.10: System architecture for simultaneous DEA actuation and EIT mapping.

When the DEA is switched on, the compliant electrodes charge. During this charging period a voltage will be developed on the HV and low-voltage EIT electrode characterised by the charging capacitance, C_{DEA} , the HV source resistance, R_{lim} , and the multiplexer on-resistance, R_{on} . The resistance of the DEA is lumped in with R_{lim} for the Equations 3.5 and 3.6 below. The charging of the DEA capacitance is governed by Equation 3.5.

$$V_{DEA_{HV}}(t) = V_{HV}(1 - e^{-t/(R_{on} + R_{lim})C_{DEA}}) \quad (3.5)$$

In the configuration shown in Figure 3.10, a voltage divider is created between the R_{lim} resistor and the multiplexer, R_{on} , on-resistance to ensure the voltage seen at the multiplexer input pin is sufficiently low. The voltage seen on the multiplexer pin is given by Equation 3.6.

$$V_{MUX}(t) = V_{HV} \frac{R_{on}}{R_{on} + R_{lim}} e^{-t/(R_{on} + R_{lim})C_{DEA}} \quad (3.6)$$

To mitigate the effects of the DEA switching transients during loading experiments, the loads were applied when the DEA voltages were at steady state, as exemplified in Figure 3.11, to observe the effects of the high voltage electrode on the EIT electrode mapping.

To investigate the effects the DEA voltage switching transient has on EIT data capture, EIT frames were captured during switching events as shown in Figure 3.11.

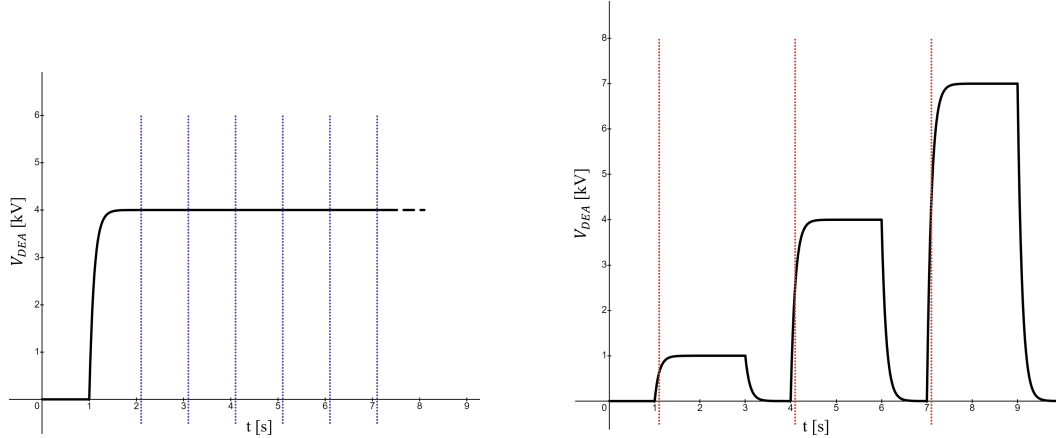


FIGURE 3.11: Illustrative experiment timing diagrams. Left: Steady state V_{DEA} where the purple dotted lines represent the time a load event begins. Right: Transient EIT measurements where the red dotted line represents the time an EIT frame capture begins.

3.3 RESULTS

First the measurements taken during fabrication are explored, followed by the results from the independent DEA actuation validation and EIT pressure mapping validation. Finally, results are presented on the phenomena of concern when integrating HV DEAs with EIT-based pressure mapping.

3.3.1 Fabrication

Prior to constructing the DEA, the compliant CBSR inter-electrode resistances, R_{int} , were measured in a similar fashion to voltage shown in Figure 3.3 to ensure the sufficient conductivity and hence CB particle dispersion for DEA actuation and EIT-based sensing. R_{int} between the adjacent circumferential electrodes for all samples was consistently < 20 k Ω , as shown in Table 3.2. Therefore, the R_{int} values indicated a sufficiently low resistance for the EIT circuitry and indicates sufficiently homogeneous CB particle dispersion.

3.3.2 DEA Validation

Before testing the piezoresistive compliant electrodes for both actuation and pressure mapping capability, the reference DEA was tested for its voltage actuation strain relationship. The theoretical actuation strain versus voltage was compared to the measured strain for the reference DEA shown in Figure 3.7(a). The actuation strain data gathered is shown in Figure 3.12. The range given was derived from substituting the range of K and ε_r parameter values found in previous similar works[32, 173, 174] into Equations 3.1 - 3.3.

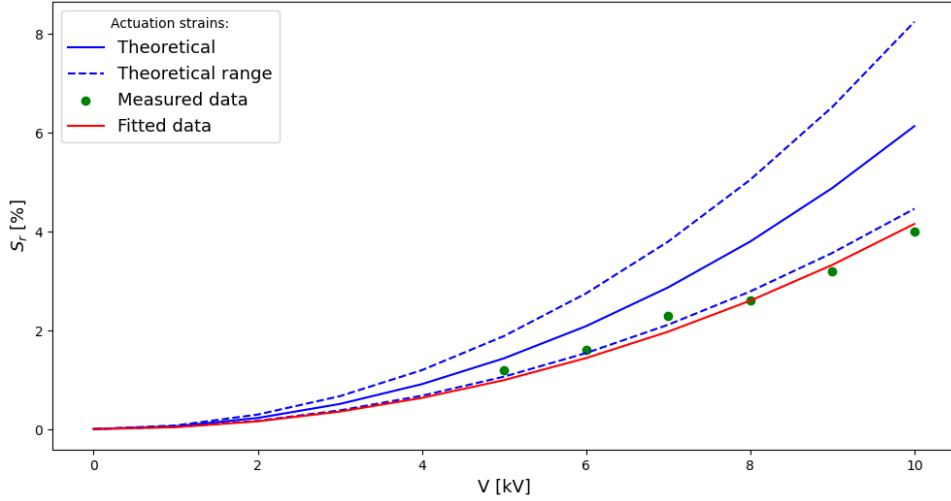


FIGURE 3.12: Comparing the measured CB reference DEA strain, the theoretical strain average and range, and the data fitted to Equation 3.3 by fitting either parameter K or ε_r .

The curve fit shown in Figure 3.12 was found to have a linear set of solutions for K and ε_r with values similar to those limits of the material given characterisation determined in previous literature [176].

The CBSR compliant electrode experiments showed significantly smaller strains relative to the DEA with the CB powder compliant electrode as displayed in Figure 3.13. The effective mechanical impedance for the DEA with the CBSR compliant electrodes was significantly increased due to the relative thickness of the CBSR electrode and similar bulk modulus relative to the DE VHB material. Hence an effective bulk modulus, K_{eff} , was calculated from fitting to the measured data, as a sum of the existing DE bulk modulus, K , and the effect of the compliant electrode's bulk modulus. K_{eff} is the a key characteristic of using thick compliant electrodes on a DEA that limits the actuation performance. When calculating K_{eff} , ε_r is assumed constant, as the effects of this different compliant electrode thickness on ε_r is assumed relatively negligible.

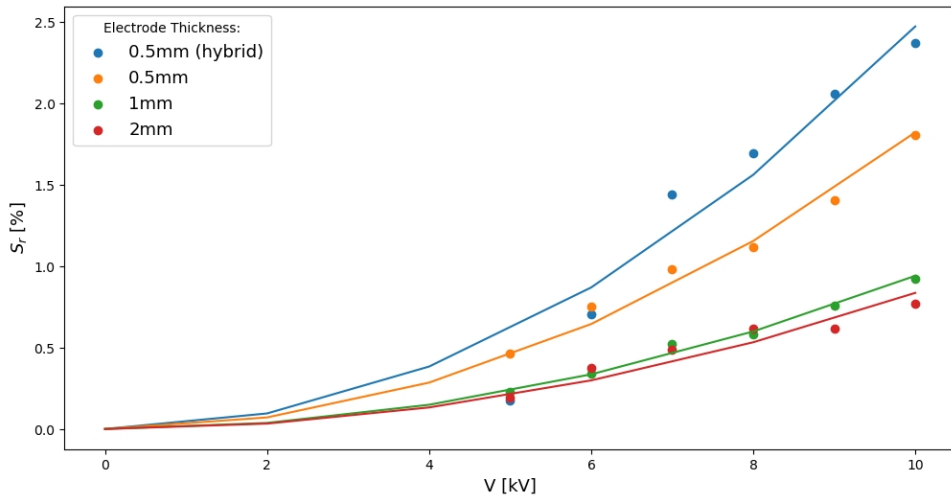


FIGURE 3.13: Comparison of the voltage strain relationships between the 100 mm diameter compliant electrodes of various thicknesses, z_{ce} , used for the DEA.

The effective bulk modulus impeding the actuation of the DE was calculated for each CBSR compliant electrode thickness by fitting to Equation 3.3 with the results displayed in Table 3.1. To further enhance the actuation strain, $S_{z_{de}}$ of the DEA-EIT device, the compliant electrodes

TABLE 3.1: Effective bulk modulus, K_{eff} , and coefficient of determination, R^2 , for each fit of voltage-strain data for the CBSR compliant electrodes.

z_{ce} [mm]	K_{eff} [kPa]	R^2
2	966	0.86
1	860	0.99
0.5	450	0.98
0.5 (hybrid)	334	0.91

were hybridised such that one of the compliant electrodes was made from CB powder and the other from the CBSR composite. The hybridised results for the K_{eff} value are also given in Table 3.1.

3.3.3 EIT Validation

Validation of the EIT sensing method on the compliant electrodes was carried out for the three different electrode thickness, z_{ce} , values to see the differences the thickness may have on the pressure mapping characteristics' spatial performance. Figure 3.14 exemplifies the difference in the conductance reconstructions for a load.

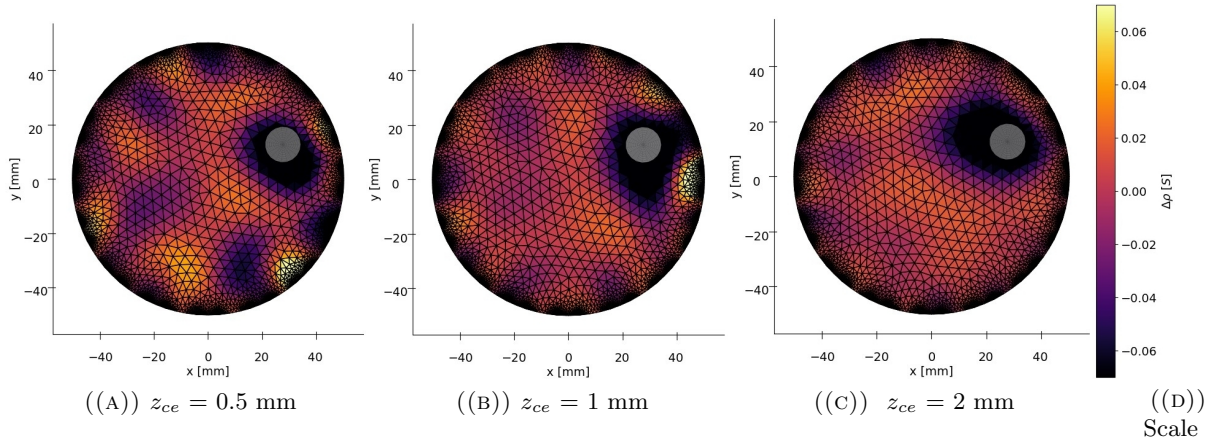


FIGURE 3.14: A 15% strain compression at point L_1 applied to 100mm diameter compliant DEA electrodes of 3 compliant electrode thicknesses.

A significant factor for determining the minimum pressure able to be detected is governed by the noise floor experienced when the domain is in a steady relaxed state. A metric used to quantify the noise floor is the noise figure, NF , which is commonly used in other applications of EIT[15, 177]. To quantify the domain homogeneity the inter-electrode resistance (i.e. between adjacent electrodes) and respective standard deviation data for each sample was gathered alongside the NF , as shown in Table 3.2.

TABLE 3.2: Noise factor and mean inter-electrode resistance, \bar{R}_{int} , for each thickness of compliant DEA electrode used for EIT

z_{ce} [mm]	NF	\bar{R}_{int} [kΩ]
2	0.99	4.40 ± 0.69
1	0.98	7.72 ± 1.14
0.5	0.96	9.91 ± 2.16

To quantify the localisation performance of the loads applied to the DEA compliant electrode the center-of-mass error, E_{CoM} , and shape fit, SF , of the sensing system were calculated. A polar histogram plot of the E_{CoM} values from each frame from an experiment are displayed in Figures 3.15(a) - 3.15(b). From this same experiment a mean E_{CoM} is given in Table 3.3.

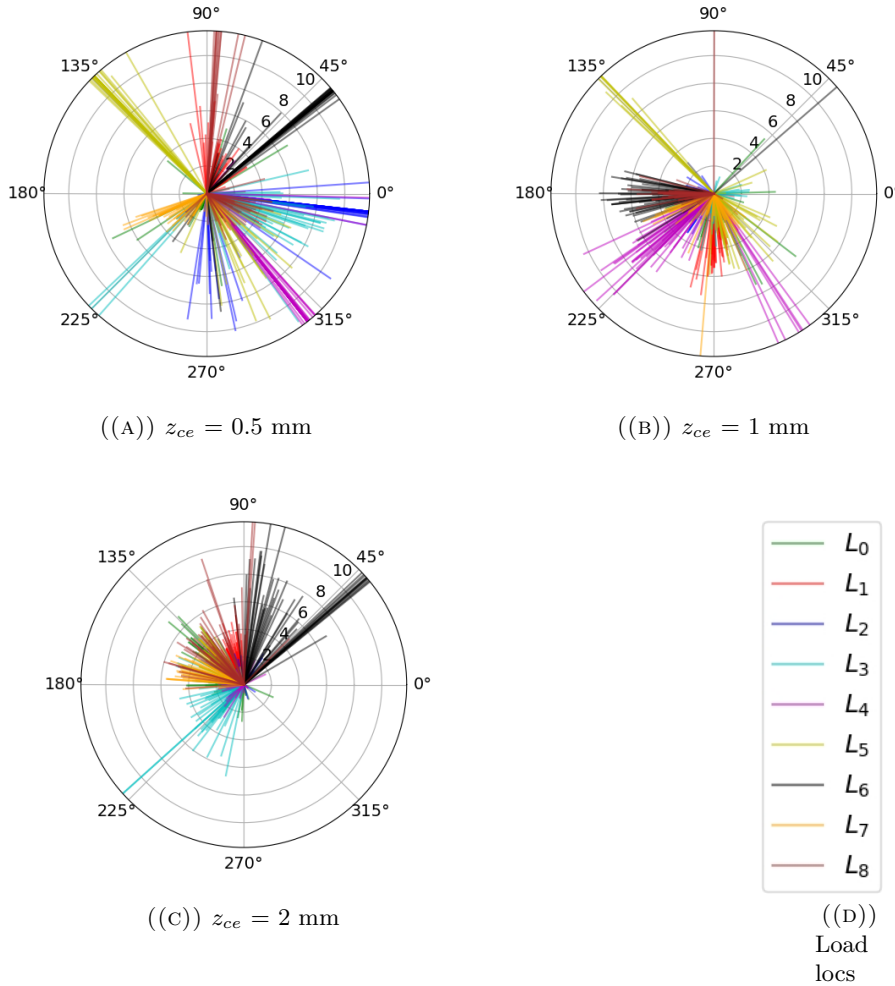


FIGURE 3.15: Vectorised E_{CoM} for the nine load experiment at 20% compressive strain for each z_{ce} value tested on individual DEA-EIT compliant electrode samples.

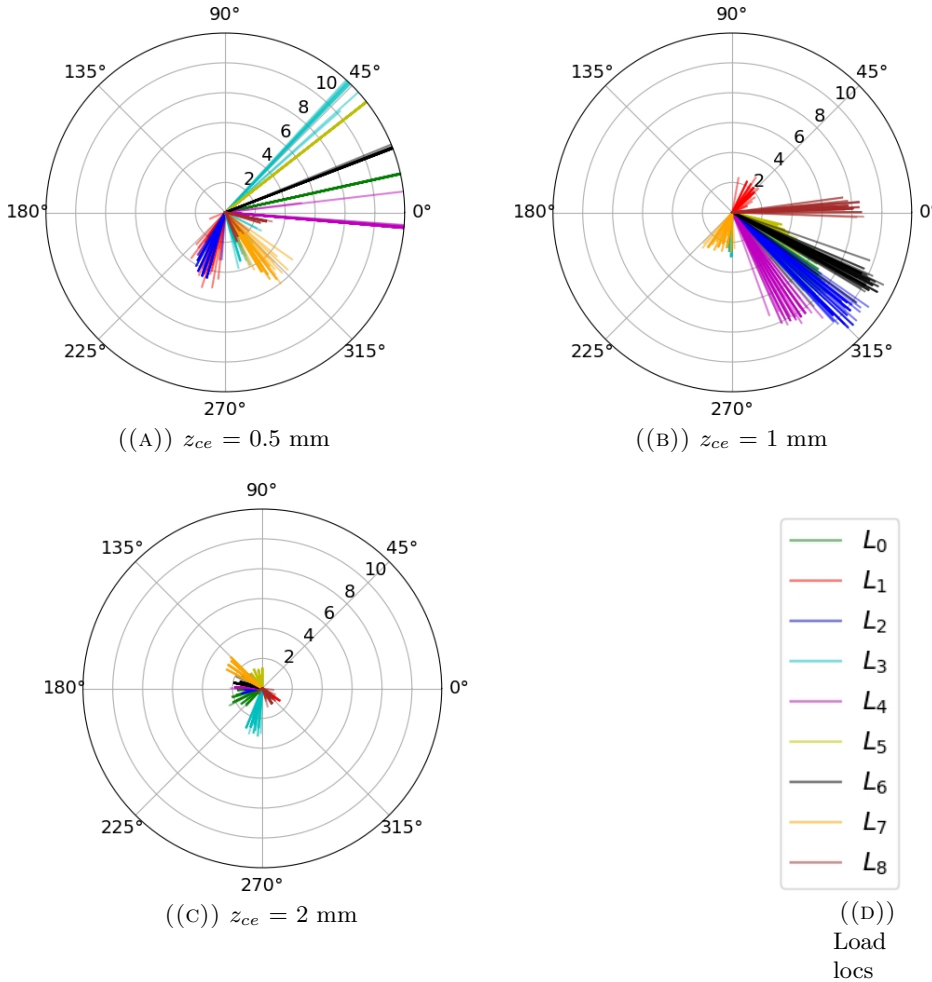


FIGURE 3.16: Vectorised E_{CoM} for the nine load experiment using the same indentation depth as Figure 3.15 for each z_{ce} value tested on the DEA-EIT integrated samples.

Mean values for the spatial performance metrics, E_{CoM} and SF , were gathered for each strain, each thickness, and at each load point. Spatial performance metric means from two nine load experiment are given in Tables 3.3 and 3.4. The SF values are found using Equation 3.4.

TABLE 3.3: Mean E_{CoM} and SF values (\pm std) obtained for each DEA compliant electrode thickness at 20% strains loads

z_{ce} [mm]	\bar{E}_{CoM} [mm]	\bar{SF} [mm^2]
2	4.10 ± 1.93	46.03 ± 0.51
1	4.25 ± 2.42	36.93 ± 0.92
0.5	10.43 ± 6.06	81.92 ± 8.43

TABLE 3.4: Mean E_{CoM} and SF values (\pm std) obtained for each DEA stack at the same indent depth as 20% strain in Table 3.3 loads. *Where the compliant electrode is part of a DE compliant electrode DEA stack.

z_{ce}^* [mm]	\bar{E}_{CoM} [mm]	\bar{SF} [mm^2]
2	1.66 ± 0.17	46.03 ± 0.56
1	6.01 ± 0.44	37.03 ± 1.06
0.5	8.83 ± 1.49	81.64 ± 7.99

3.3.4 Simultaneous Actuation and Pressure Mapping

Simultaneous actuation and pressure mapping has been performed when at a range of actuation strains using excitation voltages ranging from 1 kV to 10 kV. Each DEA voltage excitation yielded similar noise in their reconstruction results as shown in Figure 3.17.

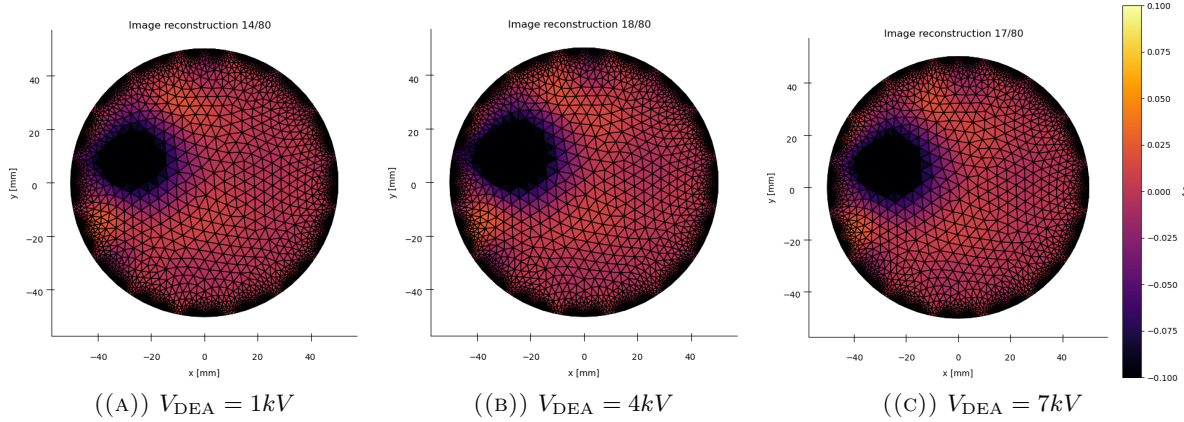


FIGURE 3.17: Loads applied to the compliant ground electrode of a DEA during different steady state voltage excitations, V_{DEA} .

The next set of experiments observed the transient effects of a high voltage step input the DEA during an EIT cycle. Artifacts such as the ones given in Figure 3.18 occur due the inrush/outrush currents across the DEA's capacitance.

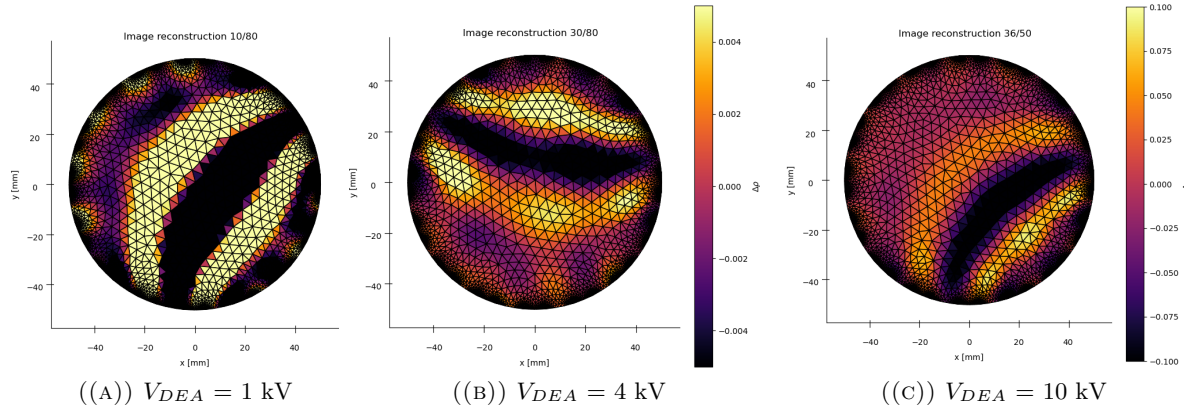


FIGURE 3.18: An unloaded DEA with a captured during various voltage, V_{DEA} , step input artifacts.

Note that the scale on Figure 3.18 contains two scales and one is an order of magnitude smaller than that seen in Figure 3.17 to highlight and investigate the transient artifact pattern observed.

3.4 DISCUSSION

A system was created that could both generate strain and map strain events using common DEA componentry with a circular DEA topology. The major limitations of integrating the two technologies were explored and quantified as a starting point for the further optimisation of such a device.

3.4.1 Fabrication

Fabrication methods were successfully developed to create a range compliant electrode composites for successful DEA actuation and EIT-based pressure mapping. The fabrication process had limited quantification of the dispersion of CB particles within the CBSR composite material used for the DEA compliant electrodes. A basic check for homogeneity was done using the device hardware measuring the inter-electrode resistance between adjacent electrodes as shown in Table 3.2. Further validation to check the homogeneity of the whole domain could be done using other invasive or non-invasive methods such as a nail-bed resistance test and/or spectroscopic imaging. Inhomogeneity quantification on a resolution similar to that of the thickness of the material sample is important to obtain a higher SNR and hence *NF* value. Dispersion of the CB particles and minimisation of air voids was ensured by using a vacuum planetary mixer, however a change to a less viscous liquid silicone rubber in future could ensure improved mixing, less air voids, and increased homogeneity.

A key limitation to decreasing the thickness of the compliant electrode occurs at a point where the tear strength of the material is significantly lower than the elastic modulus of the circumferential electrodes, hence increasing the likelihood of mechanical failure through tearing resulting in unstable conductivity or an open-circuit of the electrical connection.

Moulds were used successfully to generate a series of samples, in future work other techniques for film fabrication could be used to improve sample quality such as, screen printing, spin coating, and conductive coating deposition and spray methods [170, 178, 179] .

Stress-strain characterisation of DEs in literature clearly shows a hyperelastic softening effect between 50 to 400 % strain for VHB film material whereby the elastic modulus decreases to 40 - 70 kPa[173] . This is significantly less than the assumed ~ 142 kPa elastic modulus resulting from a 10 % pre-stretch in this work. This hyperelastic region should be determined using both the DE and compliant electrode materials' hyperelastic regions to ensure the K_{eff} is minimised for maximal actuation strain, $S_{z_{de}}$.

3.4.2 DEA Validation

Through actuation testing of different compliant electrodes applied to a DEA, models were fitted to the voltage-strain data gathered with R^2 values between 0.86 and 0.99. The model fitting resulted in the formation of effective bulk modulus, K_{eff} , values of the DEA active region ranging from 334 to 966 kPa for increasing $z_c e$ values. The use of an effective bulk modulus constant only holds for a small linear range of strains. The CBSR compliant electrodes should be modelled to produce expected behaviours for a much larger range of strains to optimise for a better DEA-EIT system over a large range of potential pre-stretches and actuation strains.

Mullins effect was expected to be observed in our experiments with CBSR compliant due to the nature of testing conductive particle filled elastomer composites[180]. Mullins effect is

the change in the stress-strain relationship when stress testing a sample at a stress value at a stress value higher than the sample has experienced in previous testing. Therefore, often before characterising conductive particle elastomer composites, the composite sample should be subjected to a stress larger than that of the intended future experimentation stresses.

It is well known in literature and is intuitive that mechanical characteristics of a DEA's compliant electrodes have a significant effect on the actuation performance [176, 181]. However, there has been a lack of empirical evidence and subsequent modelling on quantifying how much the thickness of a piezoresistive composite electrode effects actuation performance. This work provides empirical data to begin creating and validating models for thick electrode DEAs, as a step towards creating an objective function to optimise for a DEA for both actuation and sensing performance.

3.4.3 EIT Validation

A metric used to determine the minimum resistance change measured and hence pressure sensed is the noise factor, NF . NF is analogous to SNR, but instead using EIT reconstruction noise vs EIT voltage data noise. It was found that for increasing values of z_{ce} the NF values also increased. This noise correlation is exemplified in Figure 3.14.

EIT was used to map nine compressive loads applied throughout the material successfully. To compare the performance of each thickness of the compliant electrode the spatial resolution was quantified using two main performance metrics, E_{CoM} and SF . For increasing thickness of compliant electrode the E_{CoM} and its standard deviation decreased by almost an order of magnitude. However, the SF values were all within the same order of magnitude and had decreasing standard deviations for increasing z_{ce} .

The vectorised format of the E_{CoM} gave a good indication of consistent biases that were present in the sample domains when compared across several repetitions of the same experiment. The vectorised E_{CoM} values do not appear random and may instead be due to inhomogeneity. This data could be used in future in a calibration stage to determine how pressure sensed in particular regions may be spatially biased and preemptively corrected.

To ensure the EIT domain reconstruction was geometrically accurate the circumferential electrodes were modelled in the meshing software to the same width as the real circumferential electrodes. However, the embedded depth of the circumferential electrode was not modelled. Due to the manual nature of the fabrication, significant error of up to 3 mm in the circumferential spacing of the rigid EIT electrodes was present, a factor which would be improved in future iterations especially if automated fabrication were to be implemented.

3.4.4 Simultaneous Actuation and Mapping

The DEA-EIT device constructed in this work has been shown to complete simultaneous actuation and pressure mapping using the method shown in Figure 3.11.

There was no significant noise generated due to an active DEA electrode at a steady state voltage, however this may vary with rapid large loads which change the DEA capacitance and cause a large transient on the grounded EIT compliant electrode. The pressure mapping for 1 - 7 kV scenarios is shown in Figure 3.17.

The transients induced by the large sudden voltage changes are shown as crescent shaped artifact in Figure 3.18. The artifact seen in the image is due to an increase in the grounded DEA electrode voltage at a certain point during the data collection sequence of the EIT voltages.

Not all transient events were captured, which was due to aliasing. A lower EIT sample frequency and higher resolution ‘DEA transient’-‘EIT data capture’ synchronisation would aid in capturing these events more accurately.

This technology show promise and can be further optimised for improved actuation and pressure mapping capability. A system architecture integrating both DEA and EIT-based pressure mapping functionality into a single device is done using the components in Figure 3.10.

3.4.5 Altered Actuation Performance

During a compressive load event to an actuated DEA-EIT device, the DE thickness is decreased which increases the electrostatic stress, Equation 3.2, induced by the same voltage. Therefore during a compressive loading event the stress applied to the material is a combination of the external compressive load and the increased electrostatic load.

Often a DEA is pre-stretched to take advantage of the hyper-elastic region of DE material so for a smaller change in electrostatic stress, $\Delta\sigma_{es}$, a larger strain, $\Delta S_{z_{de}}$, can be achieved. An externally applied load may mean that the stress-strain region the material may be in is changed (i.e. from a linear to a hyper/hypo-elastic region) and the same $\Delta\sigma_{es}$ would have a different $\Delta S_{z_{de}}$.

3.4.6 Dielectric Breakdown

During a compressive load event to an actuated DEA-EIT device, the DE thickness is decreased which increases the concentration of charge in the strain area. Both factors increasing the likelihood of dielectric breakdown within the material.

Feedback from the EIT pressure sensor could be used to decrease the actuation voltage if the device receives a strain that is likely to cause a dielectric breakdown.

An un-explored research avenue is the structural health monitoring of DEAs using EIT. It may also be possible to alter the system given in this work to map the location and size of any dielectric breakdown using EIT concurrently on each compliant electrode. This would allow for more technology to be developed around the self-healing of DEAs.

3.5 CONCLUSION

This work demonstrates the effective integration of Electrical Impedance Tomography (EIT) with Dielectric Elastomer Actuators (DEAs) for simultaneous pressure mapping and actuation. The findings indicate that the use of piezoresistive nanoparticle elastomer composites (PNEC) allows for the emulation of pressure sensing akin to human mechanoreceptors, enhancing the sensitivity and responsiveness of DEAs in various applications. Effective bulk moduli values were found to quantify the mechanical actuation impedance of each compliant electrode thickness used, ranging from 334 to 966 kPa. Force mapping was successful with decreasing degrees of

mapping error with increasing compliant DEA electrode thickness. The best mean centre-of-mass error of 1.66 ± 0.17 mm was found for the thickest, 2 mm, compliant DEA electrode used.

The work highlights the importance of electrode thickness on the performance of pressure mapping, revealing that thicker electrodes may improve the detection of pressure changes due to their lower noise factors. The results suggest that the EIT method can provide valuable feedback for controlling actuation, potentially preventing issues such as dielectric breakdown by adjusting voltage levels in response to detected strain.

Moreover, the research opens avenues for structural health monitoring of DEAs, enabling the mapping of dielectric breakdown locations and sizes, which could lead to advancements in self-healing technologies. Overall, the integration of EIT with DEAs not only enhances their functionality but also broadens their applicability in fields such as robotics, soft actuators, and wearable technology, paving the way for future innovations in smart materials and systems.

Bibliography

- [1] Meejin Kim and Sukwon Lee. Fusion poser: 3d human pose estimation using sparse imus and head trackers in real time. *Sensors*, 22:4846, 6 2022. ISSN 1424-8220. doi: 10.3390/S22134846. URL <https://www.mdpi.com/1424-8220/22/13/4846>.
- [2] Ryo Eguchi, Brendan Michael, Matthew Howard, and Masaki Takahashi. Shift-adaptive estimation of joint angle using instrumented brace with two stretch sensors based on gaussian mixture models. *IEEE Robotics and Automation Letters*, 5:5881–5888, 10 2020. ISSN 23773766. doi: 10.1109/LRA.2020.3010486.
- [3] Logan Thomas Chatfield. A hybrid assist-as-needed elbow exoskeleton for stroke rehabilitation. 2021. doi: 10.26021/11321. URL <https://hdl.handle.net/10092/102273>.
- [4] Ben O'Brien, Todd Gisby, and Iain A. Anderson. Stretch sensors for human body motion. volume 9056, pages 254–262. SPIE, 3 2014. ISBN 9780819499820. doi: 10.1117/12.2046143. URL <https://www.spiedigitallibrary.org/conference-proceedings-of-spie/9056/905618/Stretch-sensors-for-human-body-motion/10.1117/12.2046143.full>.
- [5] XSENSOR. Xsensor — wheelchair seating. URL <https://www.xsensor.com/solutions-and-platform/csm/wheelchair-seating>.
- [6] PressureProfile. Tactile sensors for robotic applications — pps, 2023. URL <https://pressureprofile.com/robotics>.
- [7] PowerOn. Poweron: Update of the "super sensitive" - robotik-insider.de. URL <https://mrk-blog.de/en/PowerON-Update-of-the-super-sensitive/>.
- [8] Tekscan. Thin-film pressure sensors — tekscan. URL https://www.tekscan.com/thin-film-pressure-sensors?utm_source=google&utm_medium=cpc&utm_term=pressure+sensors&utm_content=eta7&utm_campaign=pressure&gad_source=1&gclid=CjwKCAiApuCrBhAuEiwA8VJ6Jt-4kVuEinAM6-jd72DwnWxvPCQus_Md7xr2i_bD0sIWg7SK7aw6nRoCuk0QAvD_BwE.
- [9] SensorProducts. Tactilus — compression force sensing resistor (fsr) — force sensing resistors — force sensing resistors — tactilus — surface pressure indicator — mapping — force sensing and profiling. URL <https://www.sensorprod.com/tactilus.php>.
- [10] Joseph Teran, Silvia Blemker, Victor Ng-Thow-Hing, and R. Fedkiw. Finite volume methods for the simulation of skeletal muscle. pages 68–74, June 2003.
- [11] Wang Yanjie and Takushi Sugino. Ionic polymer actuators: Principle, fabrication and applications. July 2018.

- [12] Nicholas Kellaris, Vidyacharan Gopaluni Venkata, Garrett M. Smith, Shane K. Mitchell, and Christoph Keplinger. Peano-hasel actuators: Muscle-mimetic, electrohydraulic transducers that linearly contract on activation. *Science Robotics*, 3(14):3276, 1 2018. ISSN 24709476. doi: 10.1126/scirobotics.aar3276. URL <http://robotics.sciencemag.org/jbr/i>.
- [13] Yu-Jin Park, Seong Hwan Kim, Tae-Hoon Lee, Ae-Ri Cha, Gi-Woo Kim, and Seung-Bok Choi. Design analysis of a magnetorheological elastomer based bush mechanism. volume 10595, March 2018. URL <https://doi.org/10.1117/12.2318795>.
- [14] Richard Ellingham and Tim Giffney. Carbon black silicone piezoresistive electrical impedance tomography stress sensor device. volume 12042, pages 207–214. SPIE, 4 2022. doi: 10.1117/12.2610694. URL <https://doi.org/10.1117/12.2610694>.
- [15] Richie Ellingham, Chris Pretty, Lui Holder-Pearson, Kean Aw, and Tim Giffney. An electrical impedance tomography based artificial soft skin pressure sensor: Characterisation and force modelling. *Sensors and Actuators A: Physical*, 373:115427, 2024. ISSN 0924-4247. doi: <https://doi.org/10.1016/j.sna.2024.115427>. URL <https://www.sciencedirect.com/science/article/pii/S0924424724004217>.
- [16] Yann Roudaut, Aurélie Lonigro, Bertrand Coste, Jizhe Hao, Patrick Delmas, and Marcel Crest. Touch sense: functional organization and molecular determinants of mechanosensitive receptors. *Channels (Austin, Tex.)*, 6:234–245, 7 2012. ISSN 1933-6950. doi: 10.4161/CHAN.22213. URL <https://www.ncbi.nlm.nih.gov/pmc/articles/pmid/23146937/?tool=EBIhttps://europepmc.org/article/pmc/3508902>.
- [17] Francesco Stella and Josie Hughes. The science of soft robot design: A review of motivations, methods and enabling technologies. *Frontiers in Robotics and AI*, 9:1059026, 1 2023. ISSN 22969144. doi: 10.3389/FROBT.2022.1059026/BIBTEX.
- [18] Yongchang Zhang, Pengchun Li, Jiale Quan, Longqiu Li, Guangyu Zhang, and Dekai Zhou. Progress, challenges, and prospects of soft robotics for space applications. *Advanced Intelligent Systems*, 5:2200071, 3 2023. ISSN 2640-4567. doi: 10.1002/AISY.202200071. URL <https://onlinelibrary.wiley.com/doi/full/10.1002/aisy.202200071https://onlinelibrary.wiley.com/doi/abs/10.1002/aisy.202200071https://onlinelibrary.wiley.com/doi/10.1002/aisy.202200071>.
- [19] Florian Hartmann, Melanie Baumgartner, Martin Kaltenbrunner, F Hartmann, M Baumgartner, and M Kaltenbrunner. Becoming sustainable, the new frontier in soft robotics. *Advanced Materials*, 33:2004413, 5 2021. ISSN 1521-4095. doi: 10.1002/ADMA.202004413. URL <https://onlinelibrary.wiley.com/doi/full/10.1002/adma.202004413https://onlinelibrary.wiley.com/doi/abs/10.1002/adma.202004413https://onlinelibrary.wiley.com/doi/10.1002/adma.202004413>.
- [20] Oncay Yasa, Yasunori Toshimitsu, Mike Y. Michelis, Lewis S. Jones, Miriam Filippi, Thomas Buchner, and Robert K. Katzschmann. An overview of soft robotics. *Annual Review of Control, Robotics, and Autonomous Systems*, 6:1–29, 5 2023. ISSN 25735144. doi: 10.1146/ANNUREV-CONTROL-062322-100607/CITE/REFWORKS. URL <https://www.annualreviews.org/content/journals/10.1146/annurev-control-062322-100607>.
- [21] Mariangela Manti, Vito Cacucciolo, and Matteo Cianchetti. Stiffening in soft robotics: A review of the state of the art. *IEEE Robotics and Automation Magazine*, 23:93–106, 9 2016. ISSN 10709932. doi: 10.1109/MRA.2016.2582718.

- [22] Chidanand Hegde, Jiangtao Su, Joel Ming Rui Tan, Ke He, Xiaodong Chen, and Shlomo Magdassi. Sensing in soft robotics. *ACS Nano*, 17:15277–15307, 8 2023. ISSN 1936086X. doi: 10.1021/ACSNANO.3C04089/ASSET/IMAGES/LARGE/NN3C04089_0013.JPG. URL <https://pubs.acs.org/doi/full/10.1021/acsnano.3c04089>.
- [23] Cosimo Della-Santina, Christian Duriez, and Daniela Rus. Model-based control of soft robots: A survey of the state of the art and open challenges. *IEEE Control Systems*, 43: 30–65, 6 2023. ISSN 1941000X. doi: 10.1109/MCS.2023.3253419.
- [24] Costanza Armanini, Frederic Boyer, Anup Teejo Mathew, Christian Duriez, and Federico Renda. Soft robots modeling: A structured overview. *IEEE Transactions on Robotics*, 6 2023. ISSN 19410468. doi: 10.1109/TRO.2022.3231360.
- [25] S. Murugesan. An overview of electric motors for space applications. *IEEE Transactions on Industrial Electronics and Control Instrumentation*, IECL-28:260–265, 1981. ISSN 00189421. doi: 10.1109/TIECI.1981.351050.
- [26] T. Ashuri, A. Armani, R. Jalilzadeh Hamidi, T. Reasnор, S. Ahmadi, and K. Iqbal. Biomedical soft robots: current status and perspective. *Biomedical engineering letters*, 10:369–385, 8 2020. ISSN 2093-985X. doi: 10.1007/S13534-020-00157-6. URL <https://pubmed.ncbi.nlm.nih.gov/32864173/>.
- [27] F. Branz and A. Francesconi. Experimental evaluation of a dielectric elastomer robotic arm for space applications. *Acta Astronautica*, 133:324–333, 4 2017. ISSN 0094-5765. doi: 10.1016/J.ACTAASTRO.2016.11.007.
- [28] Alessandro Bruschi, Davide Maria Donati, Peter Choong, Enrico Lucarelli, and Gordon Wallace. Dielectric elastomer actuators, neuromuscular interfaces, and foreign body response in artificial neuromuscular prostheses: A review of the literature for an in vivo application. *Advanced Healthcare Materials*, 10:2100041, 7 2021. ISSN 2192-2659. doi: 10.1002/ADHM.202100041. URL <https://onlinelibrary.wiley.com/doi/full/10.1002/adhm.202100041>
<https://onlinelibrary.wiley.com/doi/abs/10.1002/adhm.202100041>
- [29] Todd A. Gisby, Benjamin M. Obrien, and Iain A. Anderson. Self sensing feedback for dielectric elastomer actuators. *Applied Physics Letters*, 102, 5 2013. ISSN 00036951. doi: 10.1063/1.4805352/26744. URL [/aip/apl/article/102/19/193703/26744/Self-sensing-feedback-for-dielectric-elastomer](https://aip.org/article/102/19/193703/26744/Self-sensing-feedback-for-dielectric-elastomer).
- [30] Samuel Rosset, Benjamin M. O'Brien, Todd Gisby, Daniel Xu, Herbert R. Shea, and Iain A. Anderson. Self-sensing dielectric elastomer actuators in closed-loop operation. *Smart Materials and Structures*, 22:104018, 9 2013. ISSN 0964-1726. doi: 10.1088/0964-1726/22/10/104018. URL <https://iopscience.iop.org/article/10.1088/0964-1726/22/10/104018>
<https://iopscience.iop.org/article/10.1088/0964-1726/22/10/104018/meta>.
- [31] Xiqiang Liu, Li Wang, Guidong Chen, al, Joseph W Lowdon, Kasper Eersels, Bart van Grinsven, G Rizzello, D Naso, A York, and S Seelecke. Closed loop control of dielectric elastomer actuators based on self-sensing displacement feedback. *Smart Materials and Structures*, 25:035034, 2 2016. ISSN 0964-1726. doi: 10.1088/0964-1726/25/3/035034. URL <https://iopscience.iop.org/article/10.1088/0964-1726/25/3/035034>
<https://iopscience.iop.org/article/10.1088/0964-1726/25/3/035034/meta>.

- [32] Weiyang Huang, Guozheng Kang, and Pengyu Ma. Uniaxial electro-mechanically coupled cyclic deformation of vhb 4905 dielectric elastomer: Experiment and constitutive model. *Journal of Materials Engineering and Performance*, pages 1–16, 4 2023. ISSN 15441024. doi: 10.1007/S11665-023-08179-8/FIGURES/17. URL <https://link.springer.com/article/10.1007/s11665-023-08179-8>.
- [33] Wan Hasbullah MohdIsa, Andres Hunt, and S. Hassan HosseinNia. Sensing and self-sensing actuation methods for ionic polymer–metal composite (ipmc): A review. *Sensors* 2019, Vol. 19, Page 3967, 19:3967, 9 2019. ISSN 1424-8220. doi: 10.3390/S19183967. URL <https://www.mdpi.com/1424-8220/19/18/3967>
- [34] John A. McGrath and Jouni Uitto. Anatomy and organization of human skin. *Rook’s Textbook of Dermatology: Eighth Edition*, 1:1–53, 5 2010. doi: 10.1002/9781444317633. CH3. URL <https://onlinelibrary.wiley.com/doi/full/10.1002/9781444317633.ch3> <https://onlinelibrary.wiley.com/doi/abs/10.1002/9781444317633.ch3> <https://onlinelibrary.wiley.com/doi/10.1002/9781444317633.ch3>.
- [35] Guillaume Landry, Katia Parodi, Joachim E Wildberger, al, Mikaël Simard, Arthur Lalonde, Hugo Bouchard, Gurpreet Singh, and Arnab Chanda. Mechanical properties of whole-body soft human tissues: a review. *Biomedical Materials*, 16:062004, 10 2021. ISSN 1748-605X. doi: 10.1088/1748-605X/AC2B7A. URL <https://iopscience.iop.org/article/10.1088/1748-605X/ac2b7a> <https://iopscience.iop.org/article/10.1088/1748-605X/ac2b7a/meta>.
- [36] Holger J. Klein, Richard M. Fakin, Pascal Ducommun, Thomas Giesen, Pietro Giovanoli, and Maurizio Calcagni. Evaluation of cutaneous spatial resolution and pressure threshold secondary to digital nerve repair. *Plastic and Reconstructive Surgery*, 137:1203–1212, 2016. ISSN 00321052. doi: 10.1097/PRS.000000000002023. URL https://journals.lww.com/plasreconsurg/fulltext/2016/04000/evaluation_of_cutaneous_spatial_resolution_and.20.aspx.
- [37] Judith Krotoski, Sidney Weinstein, and Curt Weinstein. Testing sensibility, including touch-pressure, two-point discrimination, point localization, and vibration. *Journal of Hand Therapy*, 6:114–123, 4 1993. ISSN 0894-1130. doi: 10.1016/S0894-1130(12)80292-4.
- [38] Aisling Ní Annaidh, Karine Bruyère, Michel Destrade, Michael D. Gilchrist, and Mélanie Otténio. Characterization of the anisotropic mechanical properties of excised human skin. *Journal of the Mechanical Behavior of Biomedical Materials*, 5:139–148, 1 2012. ISSN 1751-6161. doi: 10.1016/J.JMBBM.2011.08.016.
- [39] Krisakorn Khaothong, J C H Goh, and C T Lim. In vivo measurements of the mechanical properties of human skin and muscle by inverse finite element method combined with the indentation test. *IFMBE Proceedings*, 31 IFMBE:1467–1470, 2010. ISSN 1433-9277. doi: 10.1007/978-3-642-14515-5_374. URL https://link.springer.com/chapter/10.1007/978-3-642-14515-5_374.
- [40] Y. Zheng and A. F.T. Mak. Effective elastic properties for lower limb soft tissues from manual indentation experiment. *IEEE Transactions on Rehabilitation Engineering*, 7: 257–267, 9 1999. ISSN 10636528. doi: 10.1109/86.788463.
- [41] Brian Holt, Anubhav Tripathi, and Jeffrey Morgan. Viscoelastic response of human skin to low magnitude physiologically relevant shear. *Journal of biomechanics*, 41:2689, 8 2008. ISSN 00219290. doi: 10.1016/J.JBIOMECH.

- 2008.06.008. URL [/pmc/articles/PMC2584606//pmc/articles/PMC2584606/?report=abstract](https://www.ncbi.nlm.nih.gov/pmc/articles/PMC2584606/)<https://www.ncbi.nlm.nih.gov/pmc/articles/PMC2584606/>.
- [42] Cameron H. Parvini, Alexander X. Cartagena-Rivera, and Santiago D. Solares. Viscoelastic parameterization of human skin cells characterize material behavior at multiple timescales. *Communications Biology* 2022 5:1, 5:1–11, 1 2022. ISSN 2399-3642. doi: 10.1038/s42003-021-02959-5. URL <https://www.nature.com/articles/s42003-021-02959-5>.
- [43] Mélanie Ottenio, Doris Tran, Aisling Ní Annaidh, Michael D. Gilchrist, and Karine Bruyère. Strain rate and anisotropy effects on the tensile failure characteristics of human skin. *Journal of the Mechanical Behavior of Biomedical Materials*, 41:241–250, 1 2015. ISSN 1751-6161. doi: 10.1016/J.JMBBM.2014.10.006.
- [44] Karen A. Newell. *Wound Closure*, pages 313–341. W.B. Saunders, 2 edition, 1 2007. ISBN 9781416030010. doi: 10.1016/B978-1-4160-3001-0.50027-7.
- [45] Sharad P. Paul. Biodynamic excisional skin tension lines for surgical excisions: untangling the science. *Annals of The Royal College of Surgeons of England*, 100:330, 4 2018. ISSN 00358843. doi: 10.1308/RCSANN.2018.0038. URL [/pmc/articles/PMC5958865//pmc/articles/PMC5958865/?report=abstract](https://www.ncbi.nlm.nih.gov/pmc/articles/PMC5958865/)<https://www.ncbi.nlm.nih.gov/pmc/articles/PMC5958865/>.
- [46] Davide Deflorio, Massimiliano Di Luca, and Alan M. Wing. Skin and mechanoreceptor contribution to tactile input for perception: A review of simulation models. *Frontiers in Human Neuroscience*, 16:862344, 6 2022. ISSN 16625161. doi: 10.3389/FNHUM.2022.862344/BIBTEX.
- [47] Hirotake Yokota, Naofumi Otsuru, Rie Kikuchi, Rinako Suzuki, Sho Kojima, Kei Saito, Shota Miyaguchi, Yasuto Inukai, and Hideaki Onishi. Establishment of optimal two-point discrimination test method and consideration of reproducibility. *Neuroscience Letters*, 714:134525, 1 2020. ISSN 0304-3940. doi: 10.1016/J.NEULET.2019.134525.
- [48] Rochelle Ackerley, Ida Carlsson, Henric Wester, Håkan Olausson, and Helena Backlund Wasling. Touch perceptions across skin sites: differences between sensitivity, direction discrimination and pleasantness. *Frontiers in Behavioral Neuroscience*, 8, 2 2014. ISSN 16625153. doi: 10.3389/FNBEH.2014.00054. URL [/pmc/articles/PMC3928539//pmc/articles/PMC3928539/?report=abstract](https://www.ncbi.nlm.nih.gov/pmc/articles/PMC3928539/)<https://www.ncbi.nlm.nih.gov/pmc/articles/PMC3928539/>.
- [49] Nicholas D.J. Strzalkowski, Robyn L. Mildren, and Leah R. Bent. Neurophysiology of tactile perception: A tribute to steven hsiao: Thresholds of cutaneous afferents related to perceptual threshold across the human foot sole. *Journal of Neurophysiology*, 114:2144, 8 2015. ISSN 15221598. doi: 10.1152/JN.00524.2015. URL <https://www.ncbi.nlm.nih.gov/pmc/articles/PMC4595609/>.
- [50] Mohsin I. Tiwana, Stephen J. Redmond, and Nigel H. Lovell. A review of tactile sensing technologies with applications in biomedical engineering. *Sensors and Actuators A: Physical*, 179:17–31, 6 2012. ISSN 0924-4247. doi: 10.1016/J.SNA.2012.02.051.
- [51] Lei Sun, Shuwen Jiang, Yao Xiao, and Wanli Zhang. Realization of flexible pressure sensor based on conductive polymer composite via using electrical impedance tomography. *Smart Materials and Structures*, 29:055004, 3 2020. ISSN 0964-1726. doi: 10.1088/1361-665X/AB75A3. URL <https://iopscience-iop-org.ezproxy.canterbury.ac.nz/article/10.1088/1361-665X/ab75a3><https://iopscience-iop-org.ezproxy.canterbury.ac.nz/article/10.1088/1361-665X/ab75a3/meta>.

- [52] Yun Lu, Weina He, Tai Cao, Haitao Guo, Yongyi Zhang, Qingwen Li, Ziqiang Shao, Yulin Cui, and Xuetong Zhang. Elastic, conductive, polymeric hydrogels and sponges. *Scientific Reports* 2014 4:1, 4:1–8, 7 2014. ISSN 2045-2322. doi: 10.1038/srep05792. URL <https://www.nature.com/articles/srep05792>.
- [53] Michael E. Spahr, Raffaele Gilardi, and Daniele Bonacchi. *Carbon Black for Electrically Conductive Polymer Applications*, pages 375–400. Springer, Cham, 2017. doi: 10.1007/978-3-319-28117-9_32. URL https://link.springer.com/referenceworkentry/10.1007/978-3-319-28117-9_32.
- [54] Patricia Hazelton, Mengguang Ye, and Xianfeng Chen. *Introduction to Conducting Polymers*. 2023. doi: 10.1021/bk-2023-1438.ch001. URL <https://pubs.acs.org/sharingguidelines>.
- [55] Yong Lae Park, Carmel Majidi, Rebecca Kramer, Phillip Brard, and Robert J. Wood. Hyperelastic pressure sensing with a liquid-embedded elastomer. *Journal of Micromechanics and Microengineering*, 20:125029, 11 2010. ISSN 0960-1317. doi: 10.1088/0960-1317/20/12/125029. URL <https://iopscience.iop.org/article/10.1088/0960-1317/20/12/125029> <https://iopscience.iop.org/article/10.1088/0960-1317/20/12/125029/meta>.
- [56] Taekeon Jung and Sung Yang. Highly stable liquid metal-based pressure sensor integrated with a microfluidic channel. *Sensors* 2015, Vol. 15, Pages 11823–11835, 15:11823–11835, 5 2015. ISSN 1424-8220. doi: 10.3390/S150511823. URL <https://www.mdpi.com/1424-8220/15/5/11823>.
- [57] Daehan Kim, Sung Hwan Kim, and Joong Yull Park. Floating-on-water fabrication method for thin polydimethylsiloxane membranes. *Polymers*, 11:1264, 8 2019. ISSN 20734360. doi: 10.3390/polym11081264. URL pmc/articles/PMC6722912/?report=abstract <https://www.ncbi.nlm.nih.gov/pmc/articles/PMC6722912/>.
- [58] Hyunwoo Yuk, Teng Zhang, German Alberto Parada, Xinyue Liu, and Xuanhe Zhao. Skin-inspired hydrogel-elastomer hybrids with robust interfaces and functional microstructures. *Nature communications*, 7:12028, 6 2016.
- [59] K. Park, H. Yuk, M. Yang, J. Cho, H. Lee, and J. Kim. A biomimetic elastomeric robot skin using electrical impedance and acoustic tomography for tactile sensing. *Science Robotics*, 7:7187, 6 2022. ISSN 24709476. doi: 10.1126/SCIROBOTICS.ABM7187/SUPPL_FILE/SCIROBOTICS.ABM7187_MOVIES_S1_TO_S4.ZIP. URL <https://www.science.org/doi/10.1126/scirobotics.abm7187>.
- [60] Haofeng Chen, Xuanxuan Yang, Jialu Geng, Gang Ma, and Xiaojie Wang. A skin-like hydrogel for distributed force sensing using an electrical impedance tomography-based pseudo-array method. *ACS Applied Electronic Materials*, 3 2023. ISSN 2637-6113. doi: 10.1021/ACSAELM.2C01394. URL <https://pubs.acs.org/doi/abs/10.1021/acsaelm.2c01394>.
- [61] Shuoyan Xu, Zigan Xu, Ding Li, Tianrui Cui, Xin Li, Yi Yang, Houfang Liu, and Tianling Ren. Recent advances in flexible piezoresistive arrays: Materials, design, and applications. *Polymers* 2023, Vol. 15, Page 2699, 15:2699, 6 2023. ISSN 2073-4360. doi: 10.3390/POLYM15122699. URL <https://www.mdpi.com/2073-4360/15/12/2699> <https://www.mdpi.com/2073-4360/15/12/2699>.
- [62] Kyoseung Sim, Zhouyu Rao, Zhanan Zou, Faheem Ershad, Jianming Lei, Anish Thukral, Jie Chen, Qing An Huang, Jianliang Xiao, and Cunjiang Yu. Metal oxide semiconductor

- nanomembrane-based soft unnoticeable multifunctional electronics for wearable human-machine interfaces. *Science advances*, 5, 8 2019. ISSN 2375-2548. doi: 10.1126/SCIADV.AAV9653. URL <https://pubmed.ncbi.nlm.nih.gov/31414044/>.
- [63] Yuting Zhu, Kean Aw, and Tim Giffney. Dielectric elastomer-based multi-location capacitive sensor. pages 84–95, 12 2021. URL <https://researchspace.auckland.ac.nz/handle/2292/60603>.
- [64] Guanhao Liang, Yancheng Wang, Deqing Mei, Kailun Xi, and Zichen Chen. Flexible capacitive tactile sensor array with truncated pyramids as dielectric layer for three-axis force measurement. *Journal of Microelectromechanical Systems*, 24:1510–1519, 10 2015. ISSN 10577157. doi: 10.1109/JMEMS.2015.2418095.
- [65] Youcan Yan, Zhe Hu, Zhengbao Yang, Wenzhen Yuan, Chaoyang Song, Jia Pan, and Yajing Shen. Soft magnetic skin for super-resolution tactile sensing with force self-decoupling. *Science Robotics*, 6:8801, 2 2021. ISSN 24709476. doi: 10.1126/SCIROBOTICS.ABC8801/SUPPL.FILE/ABC8801_SM.PDF. URL <https://www.science.org/doi/10.1126/scirobotics.abc8801>.
- [66] Gihun Lee, Hyunjin Kim, and Inkyu Park. A mini review of recent advances in optical pressure sensor. *Journal of Sensor Science and Technology*, 32:22–30, 2023. ISSN pISSN 1225-5475/eISSN 2093-7563. doi: <http://dx.doi.org/10.46670/JSST.2023.32.1.22>.
- [67] Dana Hughes and Nikolaus Correll. Texture recognition and localization in amorphous robotic skin. *Bioinspiration & Biomimetics*, 10:055002, 9 2015. ISSN 1748-3190. doi: 10.1088/1748-3190/10/5/055002. URL <https://iopscience.iop.org/article/10.1088/1748-3190/10/5/055002><https://iopscience.iop.org/article/10.1088/1748-3190/10/5/055002/meta>.
- [68] Golezar Gilanizadehdizaj, Kean C. Aw, Jonathan Stringer, and Debes Bhattacharyya. Facile fabrication of flexible piezo-resistive pressure sensor array using reduced graphene oxide foam and silicone elastomer. *Sensors and Actuators A: Physical*, 340:113549, 6 2022. ISSN 0924-4247. doi: 10.1016/J.SNA.2022.113549.
- [69] Ya Fei Fu, Feng Lian Yi, Jin Rui Liu, Yuan Qing Li, Ze Yu Wang, Gang Yang, Pei Huang, Ning Hu, and Shao Yun Fu. Super soft but strong e-skin based on carbon fiber/carbon black/silicone composite: Truly mimicking tactile sensing and mechanical behavior of human skin. *Composites Science and Technology*, 186:107910, 1 2020. ISSN 0266-3538. doi: 10.1016/J.COMPSCITECH.2019.107910.
- [70] Kun Yang, Xinkai Xia, Fan Zhang, Huanzhou Ma, Shengbo Sang, Qiang Zhang, and Jianlong Ji. Implementation of a sponge-based flexible electronic skin for safe human–robot interaction. *Micromachines*, 13:1344, 8 2022. ISSN 2072666X. doi: 10.3390/MI13081344/S1. URL <https://www.mdpi.com/2072-666X/13/8/1344><https://www.mdpi.com/2072-666X/13/8/1344>.
- [71] Jonathan Rossiter and Toshiharu Mukai. A novel tactile sensor using a matrix of leds operating in both photoemitter and photodetector modes. *Proceedings of IEEE Sensors*, 2005:994–997, 2005. doi: 10.1109/ICSENS.2005.1597869.
- [72] Sho Shimadera, Kei Kitagawa, Koyo Sagehashi, Yoji Miyajima, Tomoaki Niiyama, and Satoshi Sunada. Speckle-based high-resolution multimodal soft sensing. *Scientific Reports* 2022 12:1, 12:1–11, 7 2022. ISSN 2045-2322. doi: 10.1038/s41598-022-17026-0. URL <https://www.nature.com/articles/s41598-022-17026-0>.

- [73] Marc Ramuz, Benjamin C.K. Tee, Jeffrey B.H. Tok, and Zhenan Bao. Transparent, optical, pressure-sensitive artificial skin for large-area stretchable electronics. *Advanced Materials*, 24:3223–3227, 6 2012. ISSN 1521-4095. doi: 10.1002/ADMA.201200523. URL <https://onlinelibrary.wiley.com/doi/full/10.1002/adma.201200523><https://onlinelibrary.wiley.com/doi/abs/10.1002/adma.201200523><https://onlinelibrary.wiley.com/doi/10.1002/adma.201200523>.

[74] R. D. Keynes, David J. Aidley, and Christopher L.-H Huang. *Nerve and Muscle*. Cambridge University Press, 4 edition, 2011. ISBN 9780511853067.

[75] Robert A Cross. Myosin mechanical ratchet. *Proc Natl Acad Sci USA*, 103(24):8911, 6 2006. URL <http://www.pnas.org/content/103/24/8911.abstract>.

[76] R Mcn. Alexander and H C Bennet-Clark. Storage of elastic strain energy in muscle and other tissues. *Nature*, 265(5590):114–117, 1977. URL <https://www.scopus.com/inward/record.uri?eid=2-s2.0-0017338764&doi=10.1038%2F265114a0&partnerID=40&md5=1e1abd16ddee92cca4a7a8e6a33940f9>. Cited By :466;br/;Export Date: 10 May 2020;br/;br/;br/;Cited By :466;br/;Export Date: 10 May 2020.

[77] Robert Full and Kenneth Meijer. Metrics of Natural Muscle Function, chapter Metrics of Natural Muscle Function, pages 73–89. SPIE, 3 2004. doi: 10.1117/3.547465.ch3. URL <http://ebooks.spiedigitallibrary.org/content.aspx?doi=10.1117/3.547465.ch3>.

[78] Mihai Duduta, Ehsan Hajiesmaili, Huichan Zhao, Robert J. Wood, and David R. Clarke. Realizing the potential of dielectric elastomer artificial muscles. *Proceedings of the National Academy of Sciences of the United States of America*, 116(30679271):2476–2481, February 2019. ISSN 0027-8424. doi: 10.1073/pnas.1815053116. URL <https://www.pnas.org/content/116/7/2476><https://www.pnas.org/content/116/7/2476.abstract><https://www.ncbi.nlm.nih.gov/pmc/articles/PMC6377461/>. 30679271[pmid];br/;PMC6377461[pmcid];br/;br/;br/;30679271[pmid];br/;PMC6377461[pmcid].

[79] Nicholas P Smith, Christopher J Barclay, and Denis S Loiselle. The efficiency of muscle contraction. *Progress in Biophysics and Molecular Biology*, 88(1):1–58, 2005. ISSN 0079-6107. URL <http://www.sciencedirect.com/science/article/pii/S0079610703001081>.

[80] Archibald Vivian Hill. The heat of shortening and the dynamic constants of muscle. *Proceedings of the Royal Society of London. Series B - Biological Sciences*, 126(843):136–195, 1938. doi: 10.1098/rspb.1938.0050. URL <https://royalsocietypublishing.org/doi/pdf/10.1098/rspb.1938.0050>.

[81] Morufu Olusola Ibitoye, Nur Azah Hamzaid, Nazirah Hasnan, Ahmad Khairi Abdul Wahab, and Glen M. Davis. Strategies for rapid muscle fatigue reduction during fes exercise in individuals with spinal cord injury: A systematic review. *PloS one*, 11:e0149024, 2016.

[82] Milos R. Popovic and T. Adam Thrasher. Neuroprostheses. *Encyclopedia of Biomaterials and Biomedical Engineering*, 2004. doi: DOI:10.1081/E-EBBE120013941. URL <http://toronto-fes.ca/publications/2004Popovic.pdf>.

[83] Knut Schmidt Nielsen. *Animal Physiology: Adaptation and Environment*. Cambridge University Press, 5 edition, 2002. ISBN 521 57098. URL https://books.google.co.nz/books?id=hcw2AAAAQBAJ&printsec=frontcover&redir_esc=y#v=onepage&q&f=false.

- [84] Katie L. Meadmore, Timothy A. Exell, Emma Hallewell, Ann Marie Hughes, Chris T. Freeman, Mustafa Kutlu, Valerie Benson, Eric Rogers, and Jane H. Burridge. The application of precisely controlled functional electrical stimulation to the shoulder, elbow and wrist for upper limb stroke rehabilitation: a feasibility study. *Journal of neuroengineering and rehabilitation*, 11, 6 2014. ISSN 1743-0003. doi: 10.1186/1743-0003-11-105. URL <https://pubmed.ncbi.nlm.nih.gov/24981060/>.
- [85] Chris Freeman, Tim Exell, Katie Meadmore, Emma Hallewell, and Ann Marie Hughes. Computational models of upper-limb motion during functional reaching tasks for application in fes-based stroke rehabilitation. *Biomedizinische Technik. Biomedical engineering*, 60:179–191, 6 2015. ISSN 1862-278X. doi: 10.1515/BMT-2014-0011. URL <https://pubmed.ncbi.nlm.nih.gov/25355246/>.
- [86] Edmund F. Hodkin, Yuming Lei, Jonathan Humby, Isabel S. Glover, Supriyo Choudhury, Hrishikesh Kumar, Monica A. Perez, Helen Rodgers, and Andrew Jackson. Automated fes for upper limb rehabilitation following stroke and spinal cord injury. *Ieee Transactions on Neural Systems and Rehabilitation Engineering*, 26:1067, 5 2018. ISSN 15344320. doi: 10.1109/TNSRE.2018.2816238. URL [/pmc/articles/PMC6051484/](https://pmc/articles/PMC6051484/)?report=abstract<https://www.ncbi.nlm.nih.gov/pmc/articles/PMC6051484/>.
- [87] Dejan B. Popovic. Advances in functional electrical stimulation (fes). *Journal of Electromyography and Kinesiology*, 24:795–802, 12 2014. ISSN 1050-6411. doi: 10.1016/J.JELEKIN.2014.09.008.
- [88] Guangqiang Ma, Xiaojun Wu, Lijin Chen, Xin Tong, and Weiwei Zhao. Characterization and optimization of elastomeric electrodes for dielectric elastomer artificial muscles. *Materials* 2020, Vol. 13, Page 5542, 13(1908508):5542, 12 2020. ISSN 1996-1944. doi: 10.3390/MA13235542. URL <https://www.mdpi.com/1996-1944/13/23/5542>
<https://www.mdpi.com/1996-1944/13/23/5542>
- [89] Raphael Neuhaus, Nima Zahiri, Jan Petrs, Yasaman Tahouni, Jörg Siegert, Ivica Kolaric, Hanaa Dahy, and Thomas Bauernhansl. Integrating ionic electroactive polymer actuators and sensors into adaptive building skins – potentials and limitations. *Frontiers in Built Environment*, 6:546334, 7 2020. ISSN 22973362. doi: 10.3389/FBUIL.2020.00095/BIBTEX. URL www.frontiersin.org.
- [90] Daniel Segalman, Walter Witkowski, D Adolf, and Mohsen Shahinpoor. Theory and application of electrically controlled polymeric gels. *Smart Materials and Structures*, 1: 95, 1 1999.
- [91] Mohsen Shahinpoor. *Ionic Polymer Metal Composites (IPMCs)*. Smart Materials Series. The Royal Society of Chemistry, 2016. ISBN 978-1-78262-720-3.
- [92] Masahiro Homma and Yoshio Nakano. Development of electro-driven polymer gel/platinum composite membranes. *Kagaku Kogaku Ronbunshu*, 25(6):1010–1014, 1999. ISSN 13499203. doi: 10.1252/kakoronbunshu.25.1010.
- [93] Raymond Liu. In situ electrode formation on a nafion membrane by chemical platinization. *Journal of The Electrochemical Society*, 139(1):15, 1992. ISSN 0013-4651. URL <http://dx.doi.org/10.1149/1.2069162>.
- [94] James D Carrico, Nicklaus W Traeden, Matteo Aureli, and Kam K Leang. Fused filament 3d printing of ionic polymer-metal composites (ipmcs). *Smart Materials and Structures*, 24(12):125021, 11 2015. doi: 10.1088/0964-1726/24/12/125021. URL <https://doi.org/10.1088%2F0964-1726%2F24%2F12%2F125021>.

- [95] Mohsen Shahinpoor and Kwang J. Kim. Ionic polymer-metal composites: Iii. modeling and simulation as biomimetic sensors, actuators, transducers, and artificial muscles. *Smart Materials and Structures*, 13(6):1362–1388, 12 2004. ISSN 09641726. doi: 10.1088/0964-1726/13/6/009. URL <https://www.scopus.com/inward/record.uri?eid=2-s2.0-10444275650&doi=10.1088%2f0964-1726%2f13%2f6%2f009&partnerID=40&md5=87202eb3f7394ab27e1da783d00c7386>.
- [96] Barbar Akle and Donald J. Leo. Electromechanical transduction in multilayer ionic transducers. *Smart Materials and Structures*, 13(5):1081–1089, 10 2004. ISSN 09641726. doi: 10.1088/0964-1726/13/5/014. URL <https://www.scopus.com/inward/record.uri?eid=2-s2.0-5744242938&doi=10.1088%2f0964-1726%2f13%2f5%2f014&partnerID=40&md5=65de150f898f2264f18c2ad0633e2f74>.
- [97] Yan Xu, Gang Zhao, Changshun Ma, and Zhuangzhi Sun. Research on preparation and stacking performance of ipmc. *Journal of Biomimetics, Biomaterials and Biomedical Engineering*, 21(1):45–53, 2014. ISSN 22969845. doi: 10.4028/www.scientific.net/JBBBE.21.45. URL <https://www.scopus.com/inward/record.uri?eid=2-s2.0-84906851147&doi=10.4028%2fwww.scientific.net%2fJBBBE.21.45&partnerID=40&md5=ab1a439c97294fdb8d0bcf59ad4d5edb>.
- [98] Shuxiang Guo, T Fukuda, K Kosuge, F Arai, K Oguro, and M Negoro. Micro catheter system with active guide wire-structure, experimental results and characteristic evaluation of active guide wire catheter using icpf actuator. In *1994 5th International Symposium on Micro Machine and Human Science Proceedings*, page 191, 1994.
- [99] Akio Kodaira, Kinji Asaka, Tetsuya Horiuchi, Gen Endo, Hiroyuki Nabae, and Koichi Suzumori. Ipmc monolithic thin film robots fabricated using a multi-layer casting process. *IEEE Robotics and Automation Letters*, 4(2):1335–1342, 4 2019. ISSN 23773766. doi: 10.1109/LRA.2019.2895398.
- [100] Yi Chu Chang and Won Jong Kim. Aquatic ionic-polymer-metal-composite insectile robot with multi-dof legs. *IEEE/ASME Transactions on Mechatronics*, 18(2):547–555, April 2013. ISSN 10834435. doi: 10.1109/TMECH.2012.2210904.
- [101] Joel J. Hubbard, Maxwell Fleming, Viljar Palmre, David Pugal, Kwang J. Kim, and Kam K. Leang. Monolithic ipmc fins for propulsion and maneuvering in bioinspired underwater robotics. *IEEE Journal of Oceanic Engineering*, 39(3):540–551, July 2014. ISSN 03649059. doi: 10.1109/JOE.2013.2259318.
- [102] Jasim Khawwaf, Jinchuan Zheng, Hai Wang, and Zhihong Man. Practical model-free robust control design for an underwater ipmc actuator. In *2019 Chinese Control Conference (CCC)*, volume 2019-July, pages 3214–3219. IEEE Computer Society, 7 2019. ISBN 9789881563972. doi: 10.23919/ChiCC.2019.8866467.
- [103] E. Acome, S. K. Mitchell, T. G. Morrissey, M. B. Emmett, C. Benjamin, M. King, M. Radakovitz, and C. Keplinger. Hydraulically amplified self-healing electrostatic actuators with muscle-like performance. *Science*, 359(6371):61–65, 1 2018. ISSN 10959203. doi: 10.1126/science.aa06139. URL <http://science.sciencemag.org/>.
- [104] Christoph Keplinger, Tiefeng Li, Richard Baumgartner, Zhigang Suo, and Siegfried Bauer. Harnessing snap-through instability in soft dielectrics to achieve giant voltage-triggered deformation. *Soft Matter*, 8(2):285–288, 1 2012. ISSN 1744683X. doi: 10.1039/c1sm06736b. URL www.rsc.org/advances.

- [105] Charles Manion, Dinesh Patel, Mark Fuge, and Sarah Bergbrieter. Modeling and evaluation of additive manufacturedhasel actuators. n.d. URL https://softcontrol.mit.edu/sites/default/files/documents/SRMCIROS18_paper_13.pdf.
- [106] Shane K Mitchell, Xingrui Wang, Eric Acome, Trent Martin, Khoi Ly, Nicholas Kellaris, Vidyacharan Gopaluni Venkata, and Christoph Keplinger. An easy-to-implement toolkit to create versatile and high-performance hasel actuators for untethered soft robots. *Advanced Science*, 6(14):1900178, 7 2019. ISSN 2198-3844. doi: 10.1002/advs.201900178. URL <https://doi.org/10.1002/advs.201900178>. doi: 10.1002/advs.201900178.
- [107] Yang Liu, Meng Gao, Shengfu Mei, Yanting Han, and Jing Liu. Ultra-compliant liquid metal electrodes with in-plane self-healing capability for dielectric elastomer actuators. *Applied Physics Letters*, 103:64101, 8 2013. ISSN 0003-6951. URL <https://ui.adsabs.harvard.edu/abs/2013ApPhL.103f4101L>.
- [108] John A Rogers. A clear advance in soft actuators. *Science*, 341:968–969, 8 2013. ISSN 0036-8075. URL <https://ui.adsabs.harvard.edu/abs/2013Sci...341..968R>.
- [109] A Bele, C Tugui, M Asandulesa, D Ionita, L Vasiliu, G Stiubianu, M Iacob, C Racles, and M Cazacu. Conductive stretchable composites properly engineered to develop highly compliant electrodes for dielectric elastomer actuators. *Smart Materials and Structures*, 27(105005), 2018. URL <https://www.scopus.com/inward/record.uri?eid=2-s2.0-85054609457&doi=10.1088%2F1361-665X%2Faad977&partnerID=40&md5=37f280185c3e3f3c2bf1196fd522e256>. Cited By :1 Export Date: 8 May 2020.
- [110] Jose Enrico Q Quinsaat, Mihaela Alexandru, Frank A Nuesch, Heinrich Hofmann, Andreas Borgschulte, and Dorina M Opris. Highly stretchable dielectric elastomer composites containing high volume fractions of silver nanoparticles. *Journal of Materials Chemistry A*, 3(28):14675–14685, 2015. ISSN 2050-7488. URL <http://dx.doi.org/10.1039/C5TA03122B>.
- [111] S. Hau, G. Rizzello, and S. Seelecke. A novel dielectric elastomer membrane actuator concept for high-force applications. *Extreme Mechanics Letters*, 23:24–28, 2018. ISSN 2352-4316. URL <http://www.sciencedirect.com/science/article/pii/S2352431618301019>.
- [112] G. Kovacs, L. During, S. Michel, and G. Terrasi. Stacked dielectric elastomer actuator for tensile force transmission. *Sensors and Actuators A: Physical*, 155(2):299–307, 2009. ISSN 0924-4247. URL <http://www.sciencedirect.com/science/article/pii/S0924424709004002>.
- [113] F. Carpi and D. De Rossi. Small-strain modeling of helical dielectric elastomer actuators. *IEEE/ASME Transactions on Mechatronics*, 17(5706367):318–325, 2012. URL <https://www.scopus.com/inward/record.uri?eid=2-s2.0-84856316362&doi=10.1109/2fTMECH.2010.2100403&partnerID=40&md5=8aa3bd1f53656c405a8280ab884c829f>.
- [114] S. Pfeil, K. Katzer, A. Kanan, J. Mersch, M. Zimmermann, M. Kaliske, and G. Gerlach. A biomimetic fish fin-like robot based on textile reinforced silicone. *Micromachines*, 11(298):1–16, 2020. URL <https://www.scopus.com/inward/record.uri?eid=2-s2.0-85082725099&doi=10.3390%2fmi11030298&partnerID=40&md5=db2d25c45e87089b0ce501ad2e885d2a>.
- [115] M. Ghilardi, H. Boys, P. Torok, J. J. C. Busfield, and F. Carpi. Smart lenses with electrically tuneable astigmatism. *Scientific Reports*, 9(16127), 2019. URL <https://doi.org/10.1038/s41598-019-43820-w>.

- //www.scopus.com/inward/record.uri?eid=2-s2.0-85074625641&doi=10.1038%2fs41598-019-52168-8&partnerID=40&md5=8fc861d90be73fbb8e0c212a2800ca84.
- [116] H. Amin and S. F. M. Assal. Design methodology of a spring roll dielectric elastomer-based actuator for a hand rehabilitation system. In *2018 IEEE International Conference on Mechatronics and Automation (ICMA)*, pages 997–1002, 2018.
- [117] J. H. Park, A. El Atrache, D. Kim, and E. Divo. Optimization of helical dielectric elastomer actuator with additive manufacturing. volume 10594, 2018. URL <https://www.scopus.com/inward/record.uri?eid=2-s2.0-85050800758&doi=10.1117%2f12.2296720&partnerID=40&md5=89fe2bcddc403d953bb74c5cee2acad0>.
- [118] David McCoul, Samuel Rosset, Samuel Schlatter, and Herbert Shea. Inkjet 3d printing of uv and thermal cure silicone elastomers for dielectric elastomer actuators. *Smart Materials and Structures*, 26(12):125022, 2017. ISSN 1361665X. doi: 10.1088/1361-665X/aa9695. URL <http://dx.doi.org/10.1088/1361-665X/aa9695>.
- [119] K. Jung, K. J. Kim, and H. R. Choi. A self-sensing dielectric elastomer actuator. *Sensors and Actuators, A: Physical*, 143(2):343–351, 2008. URL <https://www.scopus.com/inward/record.uri?eid=2-s2.0-41349085167&doi=10.1016%2fj.sna.2007.10.076&partnerID=40&md5=93777dd3b85b4884763060bebeab2b4b>.
- [120] N. C. Goulbourne, E. M. Mockensturm, and M. I. Frecker. Electro-elastomers: Large deformation analysis of silicone membranes. *International Journal of Solids and Structures*, 44(9):2609–2626, 2007. ISSN 0020-7683. URL <http://www.sciencedirect.com/science/article/pii/S002076830600312X>.
- [121] Mark R Jolly, J David Carlson, Beth C Munoz, and Todd A Bullions. The magnetoviscoelastic response of elastomer composites consisting of ferrous particles embedded in a polymer matrix. *Journal of Intelligent Material Systems and Structures*, 7(6):613–622, 11 1996. ISSN 1045-389X. doi: 10.1177/1045389x9600700601. URL <https://doi.org/10.1177/1045389X9600700601>. doi: 10.1177/1045389X9600700601.
- [122] Holger Bose, Raman Rabindranath, and Johannes Ehrlich. Soft magnetorheological elastomers as new actuators for valves. *Journal of Intelligent Material Systems and Structures*, 23(9):989–994, 1 2012. ISSN 1045-389X. doi: 10.1177/1045389x11433498. URL <https://doi.org/10.1177/1045389X11433498>. doi: 10.1177/1045389X11433498.
- [123] Nurul Liyana Burhannuddin, Nur Azmah Nordin, Saiful Amri Mazlan, Siti Aishah Abdul Aziz, Seung Bok Choi, Noriyuki Kuwano, Nurhazimah Nazmi, and Norhasnidawani Johari. Effects of corrosion rate of the magnetic particles on the field-dependent material characteristics of silicone based magnetorheological elastomers. *Smart Materials and Structures*, 29, 8 2020. ISSN 1361665X. doi: 10.1088/1361-665X/AB972C.
- [124] Qi Ge, Zhiqin Li, Zhaolong Wang, Kavin Kowsari, Wang Zhang, Xiangnan He, Jianlin Zhou, and Nicholas X. Fang. Projection micro stereolithography based 3d printing and its applications. *International Journal of Extreme Manufacturing*, 2:022004, 6 2020. ISSN 2631-7990. doi: 10.1088/2631-7990/AB8D9A. URL <https://iopscience.iop.org/article/10.1088/2631-7990/ab8d9a><https://iopscience.iop.org/article/10.1088/2631-7990/ab8d9a/meta>.
- [125] Mohammadreza Lalegani Dezaki and Mahdi Bodaghi. Magnetorheological elastomer-based 4d printed electroactive composite actuators. *Sensors and Actuators A: Physical*, 349:114063, 1 2023. ISSN 0924-4247. doi: 10.1016/J.SNA.2022.114063.

- [126] Hannes Krueger, Mohammad Vaezi, and Shoufeng Yang. 3d printing of magnetorheological elastomers(mres)smart materials. volume 0, pages 213–218. Pro-AM, May 2014. ISBN 9789810904463. doi: 10.3850/978-981-09-0446-3_088.
- [127] Yakub F. Ismail M. A. Unuh H, Muhamad P and Z. Tanasta. Experimental validation to a prototype magnetorheological (mr) semi-active damper for c-class vehicle. *IJAME*, 16 (3):7034–7047, 2019.
- [128] Bing Chen, Xuan Zhao, Hao Ma, Ling Qin, and Wei-Hsin Liao. Design and characterization of a magneto-rheological series elastic actuator for a lower extremity exoskeleton. *Smart Materials and Structures*, 26(10):105008, 2017. ISSN 1361-665X. URL <http://dx.doi.org/10.1088/1361-665X/aa8343>.
- [129] Gregory J. Hiemenz, Young Tai Choi, and Norman M. Wereley. Semi-active control of vertical stroking helicopter crew seat for enhanced crashworthiness. *Journal of Aircraft*, 44 (3):1031–1034, 5 2007. ISSN 15333868. doi: 10.2514/1.26492. URL <https://arc.aiaa.org/doi/abs/10.2514/1.26492>.
- [130] D. D.L. Chung. A critical review of piezoresistivity and its application in electrical-resistance-based strain sensing. *Journal of Materials Science* 2020 55:32, 55:15367–15396, 8 2020. ISSN 1573-4803. doi: 10.1007/S10853-020-05099-Z. URL <https://link.springer.com/article/10.1007/s10853-020-05099-z>.
- [131] Hwa Kim, Kwangsik Park, and Moo Yeol Lee. Biocompatible dispersion methods for carbon black. *Toxicological Research*, 28:209, 12 2012. ISSN 19768257. doi: 10.5487/TR.2012.28.4.209. URL [/pmc/articles/PMC3834425/](https://www.ncbi.nlm.nih.gov/pmc/articles/PMC3834425/)?report=abstract<https://www.ncbi.nlm.nih.gov/pmc/articles/PMC3834425/>.
- [132] Di Wu, Mengni Wei, Rong Li, Tao Xiao, Shen Gong, Zhu Xiao, Zhenghong Zhu, and Zhou Li. A percolation network model to predict the electrical property of flexible cnt/pdms composite films fabricated by spin coating technique. *Composites Part B: Engineering*, 174:107034, 2019. ISSN 13598368. doi: 10.1016/j.compositesb.2019.107034.
- [133] L. Flandin, J. Y. Cavaille, Y. Brechet, and R. Dendievel. Characterization of the damage in nanocomposite materials by a.c. electrical properties: experiment and simulation. *Journal of Materials Science*, 34:1753–1759, 4 1999. ISSN 1573-4803. doi: 10.1023/A:1004546806226. URL <https://link.springer.com/article/10.1023/A:1004546806226>.
- [134] Sven Pegel, Petra Pötschke, Gudrun Petzold, Ingo Alig, Sergej M. Dudkin, and Dirk Lellinger. Dispersion, agglomeration, and network formation of multiwalled carbon nanotubes in polycarbonate melts. *Polymer*, 49:974–984, 2 2008. ISSN 0032-3861. doi: 10.1016/J.POLYMER.2007.12.024.
- [135] Pan Song and Yong Zhang. Vertically aligned carbon nanotubes/graphene/cellulose nanofiber networks for enhancing electrical conductivity and piezoresistivity of silicone rubber composites. *Composites Science and Technology*, 222:109366, 5 2022. ISSN 0266-3538. doi: 10.1016/J.COMPSCITECH.2022.109366.
- [136] Melika Eklund and Nellie Kjäll. Silicone-based carbon black composite for epidermal electrodes. 12 2019. URL <http://uu.diva-portal.org/smash/get/diva2:1384429/FULLTEXT02.pdf>.

- [137] Yuanzhen Wang, Chensheng Xu, Timotheus Jahnke, Wolfgang Verestek, Siegfried Schmauder, and Joachim P. Spatz. Microstructural modeling and simulation of a carbon black-based conductive polymer - a template for the virtual design of a composite material. *ACS Omega*, 7:28820–28830, 8 2022. ISSN 24701343. doi: 10.1021/AC SOMEGA.2C01755/ASSET/IMAGES/LARGE/AO2C01755_0009.JPEG. URL <https://pubs.acs.org/doi/full/10.1021/acsomega.2c01755>.
- [138] R. Neffati and J. M.C. Brokken-Zijp. Electric conductivity in silicone-carbon black nanocomposites: percolation and variable range hopping on a fractal. *Materials Research Express*, 6:125058, 11 2019. ISSN 2053-1591. doi: 10.1088/2053-1591/AB58FD. URL <https://iopscience.iop.org/article/10.1088/2053-1591/ab58fd> <https://iopscience.iop.org/article/10.1088/2053-1591/ab58fd/meta>.
- [139] D. Bloor, A. Graham, E. J. Williams, P. J. Laughlin, and D. Lussey. Metal-polymer composite with nanostructured filler particles and amplified physical properties. *Applied Physics Letters*, 88:102103, 3 2006. ISSN 00036951. doi: 10.1063/1.2183359/902621. URL [/aip/apl/article/88/10/102103/902621/Metal-polymer-composite-with-nanostructured-filler](https://aip.org/doi/10.1063/1.2183359/902621/Metal-polymer-composite-with-nanostructured-filler).
- [140] Lingyan Duan, Sirui Fu, Hua Deng, Qin Zhang, Ke Wang, Feng Chen, and Qiang Fu. The resistivity-strain behavior of conductive polymer composites: stability and sensitivity. *Journal of Materials Chemistry A*, 2: 17085–17098, 9 2014. ISSN 2050-7496. doi: 10.1039/C4TA03645J. URL <https://pubs.rsc.org/en/content/articlehtml/2014/ta/c4ta03645j> <https://pubs.rsc.org/en/content/articlelanding/2014/ta/c4ta03645j>.
- [141] Rui Zhang, Mark Baxendale, and Ton Peijs. Universal resistivity-strain dependence of carbon nanotube/polymer composites. *Physical Review B - Condensed Matter and Materials Physics*, 76:195433, 11 2007. ISSN 10980121. doi: 10.1103/PHYSREVB.76.195433/FIGURES/6/MEDIUM. URL <https://journals.aps.org/prb/abstract/10.1103/PhysRevB.76.195433>.
- [142] Leonel P. Madrid, Carlos A. Palacio, Arnaldo Matute, and Carlos A. Parra Vargas. Underlying physics of conductive polymer composites and force sensing resistors (fsrs) under static loading conditions. *Sensors (Basel, Switzerland)*, 17, 9 2017. ISSN 14248220. doi: 10.3390/S17092108. URL [/pmc/articles/PMC5621037/](https://pmc.ncbi.nlm.nih.gov/pmc/articles/PMC5621037/) [pmc/articles/PMC5621037/?report=abstract](https://www.ncbi.nlm.nih.gov/pmc/articles/PMC5621037/?report=abstract) <https://www.ncbi.nlm.nih.gov/pmc/articles/PMC5621037/>.
- [143] Ning Hu, Yoshifumi Karube, Cheng Yan, Zen Masuda, and Hisao Fukunaga. Tunneling effect in a polymer/carbon nanotube nanocomposite strain sensor. *Acta Materialia*, 56: 2929–2936, 8 2008. ISSN 1359-6454. doi: 10.1016/J.ACTAMAT.2008.02.030.
- [144] C. Grimaldi and I. Balberg. Tunneling and nonuniversality in continuum percolation systems. *Physical Review Letters*, 96:066602, 2 2006. ISSN 10797114. doi: 10.1103/PHYSREVLETT.96.066602/FIGURES/2/MEDIUM. URL <https://journals.aps.org/prl/abstract/10.1103/PhysRevLett.96.066602>.
- [145] Manuela HindermannBischoff and Françoise Ehrburger-Dolle. Electrical conductivity of carbon black-polyethylene composites: Experimental evidence of the change of cluster connectivity in the ptc effect. *Carbon*, 39:375–382, 3 2001. ISSN 0008-6223. doi: 10.1016/S0008-6223(00)00130-5.
- [146] Samuel Rosset, Oluwaseun A. Ararom, Samuel Schlatter, and Herbert R. Shea. Fabrication process of silicone-based dielectric elastomer actuators. *Journal of Visualized*

- Experiments, page 53423, 2 2016. ISSN 1940087X. doi: 10.3791/53423. URL www.jove.com?url=https://www.jove.com/video/53423.
- [147] Ehsan Hajiesmaili and David R. Clarke. Dielectric elastomer actuators. *Journal of Applied Physics*, 129:151102, 4 2021. ISSN 0021-8979. doi: 10.1063/5.0043959. URL <https://aip-scitation-org.ezproxy.canterbury.ac.nz/doi/abs/10.1063/5.0043959>.
- [148] Yaguang Guo, Liwu Liu, Yanju Liu, and Jinsong Leng. Review of dielectric elastomer actuators and their applications in soft robots. *Advanced Intelligent Systems*, 3:2000282, 10 2021. ISSN 2640-4567. doi: 10.1002/AISY.202000282. URL <https://onlinelibrary.wiley.com/doi/full/10.1002/aisy.202000282> <https://onlinelibrary.wiley.com/doi/abs/10.1002/aisy.202000282> <https://onlinelibrary.wiley.com/doi/10.1002/aisy.202000282>.
- [149] William H McKnight and Wayne C. McGinnis. Energy-harvesting device using electrostrictive polymers, 1 2002. URL <http://www.patentbuddy.com/Patent/6433465>.
- [150] Federico Carpi, Danilo De Rossi, Roy Kornbluh, Ronald Pelrine, and Peter Sommer-Larsen. Dielectric elastomers as electromechanical transducers: Fundamentals, materials, devices, models and applications of an emerging electroactive polymer technology. *Dielectric Elastomers as Electromechanical Transducers*, page 329, 7 2008. doi: 10.1016/B978-0-08-047488-5.X0001-9. URL <http://www.sciencedirect.com:5070/book/9780080474885/dielectric-elastomers-as-electromechanical-transducers>.
- [151] Soo Jin Adrian Koh, Xuanhe Zhao, and Zhigang Suo. Maximal energy that can be converted by a dielectric elastomer generator. *Applied Physics Letters*, 94, 2009. URL <http://imechanica.org/files/MaximalEnergyAPL.pdf>.
- [152] Yanju Liu, Liwu Liu, Zhen Zhang, and Jinsong Leng. Dielectric elastomer film actuators: Characterization, experiment and analysis. *Smart Materials and Structures*, 18:095024, 7 2009. ISSN 09641726. doi: 10.1088/0964-1726/18/9/095024. URL <https://iopscience-iop-org.ezproxy.canterbury.ac.nz/article/10.1088/0964-1726/18/9/095024> <https://iopscience-iop-org.ezproxy.canterbury.ac.nz/article/10.1088/0964-1726/18/9/095024/meta>.
- [153] Gugli Kofod, Peter Sommer-Larsen, Roy Kornbluh, and Ron Pelrine. Actuation response of polyacrylate dielectric elastomers. <http://dx.doi.org/10.1177/104538903039260>, 14:787–793, 12 2003. ISSN 1045389X. doi: 10.1177/104538903039260. URL <https://journals.sagepub.com/doi/10.1177/104538903039260>.
- [154] Hyouk Ryeol Choi, Kwangmok Jung, Nguyen Huu Chuc, Minyoung Jung, Igmo Koo, Jachoon Koo, Joonho Lee, Jonghoon Lee, Jaedo Nam, Misuk Cho, Youngkwan Lee, Hyouk Ryeol Choi, Kwangmok Jung, Nguyen Huu Chuc, Minyoung Jung, Igmo Koo, Jachoon Koo, Joonho Lee, Jonghoon Lee, Jaedo Nam, Misuk Cho, and Youngkwan Lee. Effects of prestrain on behavior of dielectric elastomer actuator. *Proceedings of the SPIE*, 5759:283–291, 5 2005. ISSN 0277-786X. doi: 10.1117/12.599363. URL <https://ui.adsabs.harvard.edu/abs/2005SPIE.5759..283C/abstract>.
- [155] Michael Wissler and Edoardo Mazza. Electromechanical coupling in dielectric elastomer actuators. *Sensors and Actuators A: Physical*, 138:384–393, 8 2007. ISSN 0924-4247. doi: 10.1016/J.SNA.2007.05.029.
- [156] Yunwei Mao and Lallit Anand. Fracture of elastomeric materials by crosslink failure. *Journal of Applied Mechanics, Transactions ASME*, 85, 8 2018. ISSN 15289036. doi: 10.1115/1.4040100.

- [157] Huichan Zhao, Aftab M. Hussain, Mihai Duduta, Daniel M. Vogt, Robert J. Wood, and David R. Clarke. Compact dielectric elastomer linear actuators. *Advanced Functional Materials*, 28, 10 2018. ISSN 1616301X. doi: 10.1002/adfm.201804328. URL <http://doi.wiley.com/10.1002/adfm.201804328>.
- [158] P ; Thummala, L ; Huang, Z ; Zhang, and M A E Andersen. Analysis of dielectric electro active polymer actuator and its high voltage driving circuits. *Proceedings of the International Power Modulator Symposium and High Voltage Workshop*, 2012. doi: 10.1109/IPMHVC.2012.6518779. URL <https://doi.org/10.1109/IPMHVC.2012.6518779>.
- [159] Jeong Hun Kim, Ji Young Hwang, Ha Ryeon Hwang, Han Seop Kim, Joong Hoon Lee, Jae Won Seo, Ueon Sang Shin, and Sang Hoon Lee. Simple and cost-effective method of highly conductive and elastic carbon nanotube/polydimethylsiloxane composite for wearable electronics. *Scientific Reports*, 8:54853, 12 2018. ISSN 20452322. doi: 10.1038/s41598-017-18209-w. URL www.nature.com/scientificreports.
- [160] Chongjing Cao and Andrew T. Conn. Performance optimization of a conical dielectric elastomer actuator. *Actuators*, 7:32, 6 2018. ISSN 2076-0825. doi: 10.3390/act7020032. URL <http://www.mdpi.com/2076-0825/7/2/32>.
- [161] Stefania Russo, Samia Nefti-Meziani, Nicola Carbonaro, and Alessandro Tognetti. A quantitative evaluation of drive pattern selection for optimizing eit-based stretchable sensors. *Sensors*, 17, 2017. doi: 10.3390/s17091999. URL www.mdpi.com/journal/sensors.
- [162] Akihiko Nagakubo, Hassan Alirezai, and Yasuo Kuniyoshi. A deformable and deformation sensitive tactile distribution sensor. *2007 IEEE International Conference on Robotics and Biomimetics, ROBIO*, pages 1301–1308, 2007. doi: 10.1109/ROBIO.2007.4522352.
- [163] David Silvera-Tawil, David Rye, Manuchehr Soleimani, and Mari Velonaki. Electrical impedance tomography for artificial sensitive robotic skin: A review. *IEEE Sensors Journal*, 15:2001–2016, 4 2015. doi: 10.1109/JSEN.2014.2375346.
- [164] Sang Ho Yoon, Ke Huo, Yunbo Zhang, Guiming Chen, Luis Paredes, Subramanian Chidambaram, and Karthik Ramani. isoft: A customizable soft sensor with real-time continuous contact and stretching sensing. *Proceedings of the 30th Annual ACM Symposium on User Interface Software and Technology*, pages 665–678, 10 2017. doi: 10.1145/3126594. URL <https://doi.org/10.1145/3126594.3126654>.
- [165] Krunal Koshiya, Sebastian Gratz-Kelly, Paul Motzki, and Gianluca Rizzello. An embedded self-sensing motion control system for a strip-shaped dielectric elastomer actuators. volume 12482, pages 147–155. SPIE, 4 2023. ISBN 9781510660717. doi: 10.1117/12.2657131. URL [https://www.spiedigitallibrary.org/conference-proceedings-of-spie/12482/124820I/An-embedded-self-sensing-motion-control-system-for-a-strip/10.1117/12.2657131.short](https://www.spiedigitallibrary.org/conference-proceedings-of-spie/12482/124820I/An-embedded-self-sensing-motion-control-system-for-a-strip/10.1117/12.2657131.full).
- [166] Canh Toan Nguyen, Hoa Phung, Tien Dat Nguyen, Hosang Jung, and Hyouk Ryeol Choi. Multiple-degrees-of-freedom dielectric elastomer actuators for soft printable hexapod robot. *Sensors and Actuators A: Physical*, 267:505–516, 11 2017. ISSN 0924-4247. doi: 10.1016/J.SNA.2017.10.010.

- [167] Yang Zhang, Yong Huang, Wenjie Sun, Hang Jin, Jinhui Zhang, Lida Xu, Shuai Dong, Zhenjin Xu, Bin Zhu, Jinrong Li, and Dezhi Wu. A multi-electrode electroelastomer cylindrical actuator for multimodal locomotion and its modeling. *International Journal of Mechanical Sciences*, 266:108964, 3 2024. ISSN 0020-7403. doi: 10.1016/J.IJMECSCI.2024.108964.
- [168] Jiang Zou, Shakiru Olajide Kassim, Jieji Ren, Vahid Vaziri, Sumeet S. Aphale, and Guoying Gu. A generalized motion control framework of dielectric elastomer actuators: Dynamic modeling, sliding-mode control and experimental evaluation. *IEEE Transactions on Robotics*, 2023. ISSN 19410468. doi: 10.1109/TRO.2023.3338973.
- [169] Qibing Pei, Marcus Rosenthal, Scott Stanford, Harsha Prahlad, and Ron Pelrine. Multiple-degrees-of-freedom electroelastomer roll actuators. *Smart Materials and Structures*, 13:N86, 9 2004. ISSN 0964-1726. doi: 10.1088/0964-1726/13/5/N03. URL <https://iopscience.iop.org/article/10.1088/0964-1726/13/5/N03>
<https://iopscience.iop.org/article/10.1088/0964-1726/13/5/N03/meta>.
- [170] Federico Carpi, Iain Anderson, Siegfried Bauer, Gabriele Frediani, Giuseppe Gallone, Massimiliano Gei, Christian Graaf, Claire Jean-Mistral, William Kaal, Guggi Kofod, Matthias Kollosche, Roy Kornbluh, Benny Lassen, Marc Matysek, Silvain Michel, Stephan Nowak, Benjamin O'Brien, Qibing Pei, Ron Pelrine, Björn Rechenbach, Samuel Rosset, and Herbert Shea. Standards for dielectric elastomer transducers. *Smart Materials and Structures*, 24:105025, 9 2015. ISSN 0964-1726. doi: 10.1088/0964-1726/24/10/105025. URL <https://iopscience.iop.org/article/10.1088/0964-1726/24/10/105025>
<https://iopscience.iop.org/article/10.1088/0964-1726/24/10/105025/meta>.
- [171] Jianjian Huang, Fang Wang, Li Ma, Zhiqiang Zhang, Erchao Meng, Chao Zeng, Hao Zhang, and Dongjie Guo. Vinylsilane-rich silicone filled by polydimethylsiloxane encapsulated carbon black particles for dielectric elastomer actuator with enhanced out-of-plane actuations. *Chemical Engineering Journal*, 428:131354, 1 2022. ISSN 1385-8947. doi: 10.1016/J.CEJ.2021.131354.
- [172] Hiroki Shigemune, Shigeki Sugano, Jun Nishitani, Masayuki Yamauchi, Naoki Hosoya, Shuji Hashimoto, and Shingo Maeda. Dielectric elastomer actuators with carbon nanotube electrodes painted with a soft brush. *Actuators*, 7:51, 8 2018. ISSN 2076-0825. doi: 10.3390/ACT7030051. URL <https://www.mdpi.com/2076-0825/7/3/51>
<https://www.mdpi.com/2076-0825/7/3/51>.
- [173] Leipeng Liu, Yanfei Huang, Yihe Zhang, Elshad Allahyarov, Zhongbo Zhang, Fengzhu Lv, and Lei Zhu. Understanding reversible maxwellian electroactuation in a 3m vhb dielectric elastomer with prestrain. *Polymer*, 144:150–158, 5 2018. ISSN 0032-3861. doi: 10.1016/J.POLYMER.2018.04.048.
- [174] Alexander Helal, Marc Doumit, and Robert Shaheen. Biaxial experimental and analytical characterization of a dielectric elastomer. *Applied Physics A: Materials Science and Processing*, 124:1–11, 1 2018. ISSN 14320630. doi: 10.1007/S00339-017-1422-3/TABLES/3. URL <https://link.springer.com/article/10.1007/s00339-017-1422-3>.
- [175] Deng Pan and Adrian Koh Soo Jin. Uniaxial prestretch dependence of dielectric permittivity in polyacrylate elastomers, 7 2015. URL <http://dengpan.ca/reports/vhb.pdf>.
- [176] Federico Carpi, Piero Chiarelli, Alberto Mazzoldi, and Danilo De Rossi. Electromechanical characterisation of dielectric elastomer planar actuators: comparative evaluation of different electrode materials and different counterloads. *Sensors and Actuators A: Physical*, 107:85–95, 10 2003. ISSN 0924-4247. doi: 10.1016/S0924-4247(03)00257-7.

- [177] Andy Adler, John H. Arnold, Richard Bayford, Andrea Borsic, Brian Brown, Paul Dixon, Theo J.C. Faes, Inéz Frerichs, Hervé Gagnon, Yvo Gärber, Bartłomiej Grychtol, Günter Hahn, William R.B. Lionheart, Anjum Malik, Robert P. Patterson, Janet Stocks, Andrew Tizzard, Norbert Weiler, and Gerhard K. Wolf. Greit: a unified approach to 2d linear eit reconstruction of lung images. *Physiological measurement*, 30, 2009. ISSN 0967-3334. doi: 10.1088/0967-3334/30/6/S03. URL <https://pubmed.ncbi.nlm.nih.gov/19491438/>.
- [178] Florian M. Weiss, Frederikke B. Madsen, Tino Töpper, Bekim Osmani, Vanessa Leung, and Bert Müller. Molecular beam deposition of high-permittivity polydimethylsiloxane for nanometer-thin elastomer films in dielectric actuators. *Materials and Design*, 105: 106–113, 2016. ISSN 18734197. doi: 10.1016/j.matdes.2016.05.049.
- [179] Musthafa O. Mavukkandy, Samantha A. McBride, David M. Warsinger, Nadir Dizge, Shadi W. Hasan, and Hassan A. Arafat. Thin film deposition techniques for polymeric membranes— a review. *Journal of Membrane Science*, 610:118258, 9 2020. ISSN 18733123. doi: 10.1016/j.memsci.2020.118258.
- [180] Julie Diani, Bruno Fayolle, and Pierre Gilormini. A review on the mullins effect. *European Polymer Journal*, 45:601–612, 3 2009. ISSN 0014-3057. doi: 10.1016/J.EURPOLYMJ.2008.11.017.
- [181] Junshi Zhang, Lei Liu, and Hualing Chen. Electromechanical properties of soft dissipative dielectric elastomer actuators influenced by electrode thickness and conductivity. *Journal of Applied Physics*, 127:184902, 5 2020. ISSN 10897550. doi: 10.1063/5.0001580/280844. URL [/aip/jap/article/127/18/184902/280844/Electromechanical-properties-of-soft-dissipative](https://aip.org/pubs/journals/127/18/184902/280844/Electromechanical-properties-of-soft-dissipative).